UNIVERSITY OF PRETORIA

MASTERS THESIS

FINITE ELEMENT MODELLING OF CREEP FOR AN INDUSTRIAL APPLICATION

Author:
Gareth Howard

Supervisors:
Dr. Helen Inglis
Mr Francesco Pietra

A thesis submitted in partial fulfillment of the requirements for the degree of

Master of Engineering

in the Department of Mechanical and Aeronautical Engineering

January 31, 2017

The financial assistance of the National Research Foundation (NRF) towards this research is hereby acknowledged. Opinions expressed and conclusions arrived at, are those of the author and are not necessarily to be attributed to the NRF

"Anyone who stops learning is old, whether at twenty or eighty. Anyone who keeps learning stays young. The greatest thing in life is to keep your mind young."

Henry Ford

UNIVERSITY OF PRETORIA

Abstract

Mechanical and Aeronautical Engineering

Masters in Engineering

FINITE ELEMENT MODELLING OF CREEP FOR AN INDUSTRIAL APPLICATION

by Gareth Howard

Thermal power stations operate at elevated temperatures and pressures in order to attain maximum available steam energy. At these high temperatures creep becomes a dominant mechanism that needs to be considered. However, for many components, the locations where peak stresses occur are unreachable to apply the commonly used Non-Destructive Testing (NDT) techniques. This encourages the use of Finite Element Analysis (FEA) to better predict the creep state in these complex components.

Commonly, creep damage models are used in conjunction with accelerated creep tests to develop material models that can be implemented into a FEA to determine failure. These approaches are often infeasible for industrial decision-making, leaving a gap for more accessible commercially available models to be developed. This paper focuses on using openly available creep data from the Japanese National Institute for Material Science (NIMS). A creep strain model capable of modelling only the primary and secondary creep regimes was then chosen from the ANSYS database to fit this data. In order to fully characterise the experimental data a multi-creep-model approach was adopted that uses a family of creep models, instead of a single creep material model, to characterise the probable range of responses. This methodology was applied to an industrial application, namely an Intermediate Pressure (IP) valve operating under creep-prone conditions. The multi-creep-model approach was incorporated into FEA to analyse the variation in stress distributions. It was interesting to see that a variation of 153% in the creep strain models only resulted in a 21% variation in the relaxed stress. Worst case scenario life time calculations were then conducted using both a time-based Larson-Miller approach and a strain-based ASME code approach. Both sets of results showed that, for the specific component of interest, creep rupture lifetimes were in excess of 3000 years. It was therefore noted that, for the IP valve of interest, the operating temperature and pressure combination were such that no worrisome creep damage occurred. In conclusion, for the specific component analysed, the operating conditions are such that creep based failure will not occur.

Keywords: Creep, Finite Element Analysis, NIMS experimental data

Acknowledgements

I would like to express my greatest gratitude towards all who supported me throughout the two years completing this dissertation:

- First and foremost, my academic supervisors Dr Helen Inglis and Mr Francesco Pietra for their academic and personal mentorship throughout my studies. Without their expertise, helping hands and encouraging words, this dissertation would not have been possible.
- Ronnie Scheepers, Marthinus Bezuidenhout, and Micheal Hindley for their industry perspectives and recommendations.
- My parents Paul and Wendy Howard for their support, guidance and love throughout my academic journey. Without your upbringing I would not have grown into the man I am today.
- My brother Brandon Howard for always being there for support. I wish you all the best throughout your life's journeys.
- My friends, for providing that most important balance between academic and social spheres, and sharing in my academic experience. I wish you all the very best in your future endeavours.
- Prof Stephan Heyns along with the Centre for Asset Integrity Management (C-AIM), Eskom Power Plant Engineering Institute (EPPEI), and the National Research Foundation (NRF) for their financial support throughout my postgraduate studies at the University of Pretoria.

Contents

List of Abbreviations

CTE	Coefficient of Thermal Expansion
FE	Finite Element
FEA	Finite Element Analysis
FEM	Finite Element Method
GB	Grain Boundary
GBS	Grain Boundary Sliding
HP	High Pressure
IP	Intermediate Pressure
L-M	Larson-Miller
LP	Low Pressure
LSE	Least Squares Error
NDT	Non Destructive Testing
NIMS	National Institute for Material Science
OEM	Original Equipment Manufacturer
RT	Room Temperature
UTS	Ultimate Tensile Strength

List of Symbols

Symbol	Description	Units
b	Burgers vector	m
C_p	Specific heat	$\mathrm{J\,kg^{-1}\,K^{-1}}$
D	Fourth order tensor	
d	Average grain diameter	m
D_V	Volume diffusivity through grain interior	
D_{GB}	Grain boundary diffusivity	
E	Young's modulus	Pa
F	Force	N
G	Shear modulus	Pa
k	Boltmann's constant	$\mathrm{m^2\,kg\,s^{-2}\,K^{-1}}$
P	Pressure	Pa
P_{LM}	Larson-Miller parameter	
Q	Activation energy	J
R	Universal gas constant	$\mathrm{J\,mol^{-1}\,K^{-1}}$
r	Radius	m
t	Time	s
T	Temperature	K
α	Coefficient of thermal expansion	$\mathrm{K^{-1}}$
ε	Strain	$\mathrm{mm\,mm^{-1}}$
μ	Coefficient of friction	
ν	Poisson's ration	
ρ	Density	$\mathrm{kg\,m^{-3}}$
σ	Stress	Pa
ω	Damage parameter	

Superscript	Description
$\cdot$	Rate
$*$	Converged solution

Subscripts	Description
a	Axial
cr	Creep
el	Elastic
f	Failure
h	Hoop
i	Internal
o	Outer

Subscripts cont'd	Description cont'd
pl	Plastic
r	Rupture, radial
R	Reaction
ter	Tertiary creep

Chapter 1

Introduction

1.1 Background

Due to increasing energy demands worldwide, power stations have come under extreme pressure. This has led to an ongoing effort to extend the design life of components in South African power stations. Many of these power stations have deteriorated markedly with age, and as a consequence the structural loads on components which are subjected to these extended lives may be such that failure is imminent. For this reason the industry needs more accurate methods of modelling materials and predicting remaining useful life.

A representation of the power cycle and the arrangement of major components in steam power plants is shown in Figure 1.1. This schematic shows the general layout of the steam turbines, and is by no means a detailed layout of components. The steam turbines used for power generation usually consist of a high pressure (HP), intermediate pressure (IP), and low pressure (LP) section. Steam is heated to the prescribed temperature and pressure by the boiler, and passed into the inlet of the HP turbine to expand through a series of stages, increasing in blade height, to the exhaust of the turbine. Each stage consists of a row of stationary blades fixed to the casing, as well as a row of rotating blades attached to the turbine rotor shaft. After the steam exits the HP turbine it is typically passed through the boiler for a reheat to increase temperature and pressure before entering the IP turbine. Between the turbine sections are valves which control the flow of steam into and between turbine sections. Lastly the steam passes through the LP turbine and exhausts to a condenser. A series of pumps allows the condensed water to be passed back to the boiler where the closed cycle process is repeated [1].

The efficiency of the thermal power systems, specifically the steam turbines, is directly related to the inlet conditions of the steam. Increasing the pressure and temperature of the inlet steam leads to improved cycle efficiency. These high operating temperatures however lead to challenges in the design and maintenance of components that are susceptible to creep, which is the irreversible deformation of material at high temperatures [2]. The accurate prediction of the creep state of a material is thus of the utmost importance in making informed predictions on the remaining useful life of components.

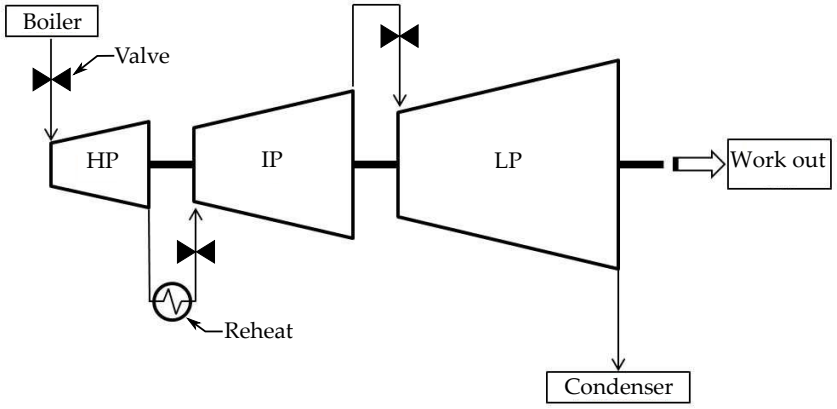

Figure 1.1: Simple schematic of steam turbine layout

1.2 Definition of creep

Creep is defined as time-dependent irreversible deformation at elevated temperatures [2]. Most metals experience creep at temperatures elevated to approximately 40% of their melting point temperature in K. Due to the fact that creep involves thermally activated processes, which are generally time-dependent, creep strain and eventual creep fracture can occur at stresses well below the macroscopic yield strength of the material. In addition creep has no lower yield point below which permanent plastic deformation will not occur. Creep is therefore assumed to be active when any non-zero stress is present in the material.

Creep is generally considered to occur in three stages, namely primary creep, secondary or steady-state creep, and tertiary creep, as depicted in Figure 1.2. Primary creep is characterised by a transient response in which strain rate $\dot{\varepsilon} = d\varepsilon/dt$ decreases with time. This decreasing strain rate is believed to be due to a changing microstructure, causing increasing resistance to dislocation movement. Secondary creep, which comprises most of the part's life, is characterised by approximately linearly increasing strain and is hence also referred to as steady-state creep. During secondary creep there is an approximate balance between dislocation increase due to strain hardening and dislocation annihilation due to recovery, hence the approximately steady creep strain rate. Lastly, tertiary creep is characterised by exponentially increasing strain until eventual rupture occurs. The onset of tertiary creep is usually macroscopically characterized by the onset of necking and damage, and hence tertiary creep is short lived. Additionally, an instantaneous strain ε_0 is usually present due to the initial loading conditions. This strain is mostly elastic, however it can contain plastic strain depending on the magnitude of the applied loading.

The change in the microstructure throughout the creep life of a component can be seen in Figure 1.3, which shows the development of voids, which eventually form cracks that can lead to failure. Initially, creep loading causes voids to form. These voids slowly align and over time form microcracks in the microstructure. These microcracks grow and lead to the formation of macrocracks, which can lead to eventual failure of a component.

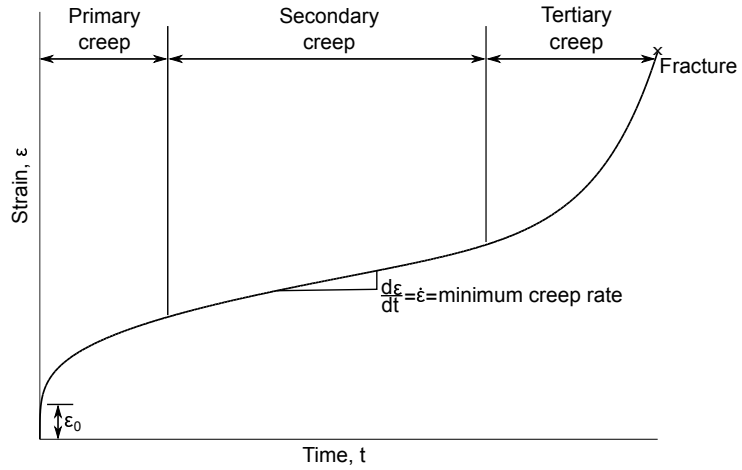

Figure 1.2: Typical creep curve showing three stages of creep, adapted from [2]

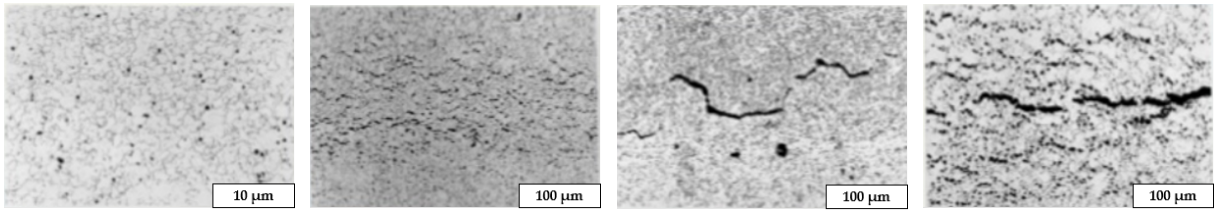

(a) (b) (c) (d)

Figure 1.3: Void development over time showing (a) Isolated voids, (b) Orientated voids, (c) Micro-cracks, and (d) Macro-cracks, adapted from [3]

1.3 Motivation

At the high operating temperatures experienced in thermal power plants creep becomes an important mechanism to consider. Engineers therefore need to make accurate and reliable predictions of the creep state of components.

The creep state of a component is usually monitored on site by means of replica metallography. This method consists of taking surface replicas of the component of interest, viweing these replicas under a microscope, and counting the voids [4]. Estimations on the extent of creep life damage can then be made by determining the voids/unit area. Although replicas can give an accurate estimate of the creep state in a component, the areas where failure is expected to occur are often unreachable to make use of replica metallography. Furthermore, many components are located such that inspection requires major downtime to the plant, leading to unnecessary production losses.

This encourages the use of Finite Element Analysis (FEA) to model components, and make accurate and reliable predictions on the remaining useful life of said components. By using FEA software, engineers can use built in creep material models to determine the creep state of components after time at exposed loads.

1.4 Objectives

With the above in mind, four objectives were identified for this study. These are:

1. To make use of available experimental creep data to fit creep material models.
2. To determine an adequate creep material model for use in an FEA package.
3. To develop a working Finite Element (FE) model that reliably estimates the creep state in a specific component.
4. To develop a methodology for quantifying the creep life of components through the use of FEA.

1.5 Approach

This research was conducted in conjunction with an industry sponsor, and thus certain industry specifications were given. These were:

1. The ANSYS FEA package must be used due to the industry use of this package.
2. The component to be modelled is an IP valve made from a 1Cr-1Mo-0.25V cast alloy steel.

With the above two specifications, the four predefined objectives can be approached in a more efficient manner. Each of the four objectives were approached in a different manner, listed as follows:

1. Due to the time constraints associated with a Masters degree, long term creep tests were not conducted. Instead, openly available creep data was used to develop the required creep material models.
2. Since the study is restricted to the use of ANSYS FEA software, research was conducted on the available creep models. Analysis of the data alongside a small numerical study is used to determine an adequate creep material model.
3. In order to develop a working FE model an in depth study was done to ensure a converged and verified result was obtained.
4. In order to quantify the creep state of the specific valve of interest two methodologies are proposed to determine the remaining useful life. These included time based and strain based lifetime calculations.

1.6 Thesis overview

The work conducted in this thesis is split into six main chapters.

Chapter 2 focuses on the relevant literature and theory required for the development of the work throughout the remainder of the thesis. Creep is first discussed from a

microstructural stand point. The mathematical modelling of creep is then presented, and from that, its application to Finite Element Methods (FEM).

Chapter 3 is the first of the application based chapters, and develops the creep strain material model required in ANSYS. The chapter focuses on the use of optimisation to fit a selected creep strain model to the available creep data. This involved the development of a new methodology that utilises multiple models, as opposed to a single model to characterise the creep strain data.

Chapter 4 develops the working FE model required throughout the remainder of the research. A study is done to ensure that a converged solution is obtained. This entailed the use of a static model to determine correct boundary conditions and mesh properties. Thick wall theory was then used to verify the FEA results.

In Chapter 5 the results from both Chapter 3 and Chapter 4 are used to develop a steady state FE creep model. A multi-model approach is utilised, and the results for each of the numerical tests are shown and compared. Chapter 6 then develops a methodology for calculating creep life based on the results from Chapter 5. This is done through the use of time-based and strain-based calculations.

Lastly, Chapter 7 concludes on the entirety of the work done throughout the thesis. The main outcomes are highlighted, and some recommendations for future work proposed.

Chapter 2

Literature

In Chapter 1 it was shown that due to the high operating temperatures in thermal power stations, creep is a problem that cannot be avoided. The aim of this research is to better understand creep on a continuum level, and to create a working FE model. However, before looking at creep from a macroscopic continuum level, one needs a better understanding of creep on a micro-structural level. With this knowledge we can begin to better understand the mathematical models defining material creep, and their use in FE applications.

This chapter focuses on the relevant literature required for understanding and modelling creep. First, creep is discussed from a micro-structural point of view. Constitutive creep models are then discussed, and their applications to FEA. A complete discussion of the applications of these models to FEA is reviewed, including discussions on previous work, creep capabilities of commercial FE code, and optimisation techniques used to fit material models.

2.1 High temperature deformation of metals

Creep in metals is a phenomenon that occurs at elevated temperatures. On a micro-structural level, creep is defined as the irreversible strain occurring when there is sufficient energy in the system to cause thermal activation of slip processes [5]. In metals this occurs in components that are subjected to stress over time at elevated temperatures. An important note here is that creep is a time-dependent process, a manifestation of the anelastic behaviour of materials at high temperatures. Commonly, elasticity theory assumes that elastic strain is a function of only stress ($\varepsilon_{el} = f(\sigma)$). Anelasticity refers to the time dependency of strain, a common phenomenon of metals at higher temperatures. That is, elastic strain is a function of both stress and time ($\varepsilon_{el} = f(\sigma, t)$) [5].

Figure 2.1 demonstrates this time-dependent behaviour of metals at higher temperatures. It can be seen that upon unloading there is an instantaneous decrease in strain equal in magnitude to the instantaneous strain which occurred at time zero. However, there is also an additional recovery which is equal in magnitude to the anelastic strain accumulated over time. A final unrecoverable strain is left, equal to the irreversible creep strain accumulated up until the time of unloading.

The high temperatures associated with creep result in increased atom mobility. This is analogous to the increased mobility of atoms in steam, in comparison to their state as

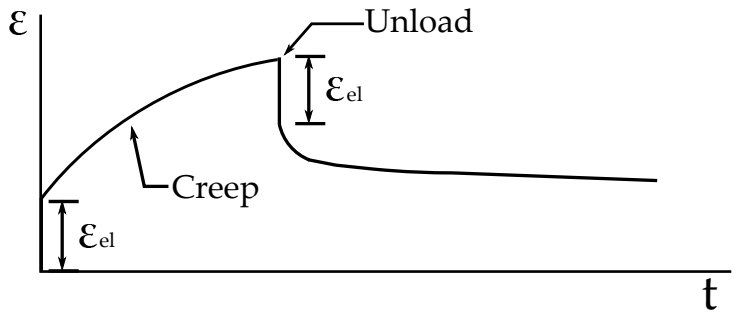

Figure 2.1: Example of material anelastic behaviour, adapted from [5]

a liquid. At these elevated temperatures there is more thermal energy present in the system, meaning that less mechanical energy, in the form of applied stress, is required to deform the material. In the absence of creep, the deformation mechanisms are slip and twinning [6]. However, at elevated temperatures there are additional deformation mechanisms that become more significant, the most important of which are discussed in the following subsection.

2.2 Creep deformation mechanisms

This subsection will discuss three of the most dominant creep deformation mechanisms, namely grain boundary sliding (GBS), intergranular diffusion creep, and dislocation creep [7].

2.2.1 Grain boundary sliding

As the name implies, GBS is the movement of grains relative to one another [5]. A study done by Ando et al. [8] shows a sample surface that was scribed with a mesh. After deformation the effect of GBS could be clearly seen by the misalignment along the grain boundaries (GB), as depicted in Figure 2.2. Research has shown that although the total accumulated creep due to GBS is small, it is a requirement for initiating cracks along the grain boundary. Due to the fact that the amount of GBS is dependent on the total GB area, a microstructure with larger grains will be less susceptible to grain boundary sliding. Manufacturers in the turbine blade industry often use this fact to their advantage by growing long columnar grain structures, or even eliminating grain boundaries completely by using single crystals [9].

2.2.2 Intergranular diffusion creep

At higher temperatures the mobility of atoms increases due to the increase in system energy. Therefore it is expected that diffusion-controlled processes become significant at the higher temperatures present during creep deformation [5]. Intergranular diffusion creep is unique in the sense that it is not dependent on the slip of dislocations, as is the case in slip and twinning, but rather occurs through diffusion of vacancies between grain boundaries. This mechanism occurs mainly at high temperatures, where many vacancies are present. Such diffusional creep is believed to occur through the movement of atomic vacancies from boundaries under tension to those under compression,

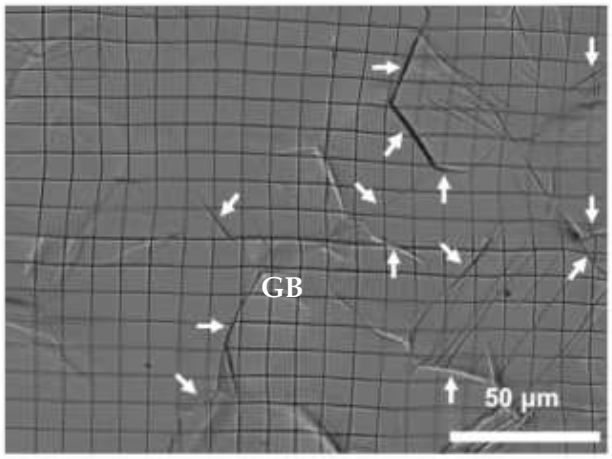

Figure 2.2: Illustration of grain boundary sliding, adapted from [8]

with the corresponding movement of atoms in the opposite direction [10]. The movement of these atoms is seen as material movement, resulting in a strain in the direction of the applied stress. Diffusional creep can be classified into either Nabarro-Herring or Coble creep. In Nabarro-Herring creep the atoms are thought to move through the grain itself, which results in the strain rate formulation given by

$$\dot{\varepsilon}_{cr} = \frac{7\sigma b^3 D_V}{d^2 kT}, \tag{2.1}$$

where creep strain rate $\dot{\varepsilon}_{cr}$ is written as a function of the applied stress σ, Burgers vector b, volume diffusivity through grain interior D_V, grain size d, Boltzmann's constant k, and temperature T [10].

The stress range where Nabarro-Herring creep is present is given by $\sigma/G < 10^{-4}$, where G is the shear modulus of the material. It has since been proposed by Coble [11] that at lower temperatures the diffusion of vacancies will not occur through the grain itself, but rather along the grain boundaries. A modified creep strain rate equation for Coble creep is given by

$$\dot{\varepsilon}_{cr} = \frac{50\sigma b^4 D_{GB}}{d^3 kT}, \tag{2.2}$$

where D_{GB} is the grain boundary diffusivity [10].

It is worth noting from Equation 2.1 and Equation 2.2 that larger grains result in lower creep strain rates, with Coble creep showing a higher sensitivity to grain size than Nabarro-Herring creep. The movement of vacancies in both Nabarro-Herring and Coble creep are shown schematically in Figure 2.3.

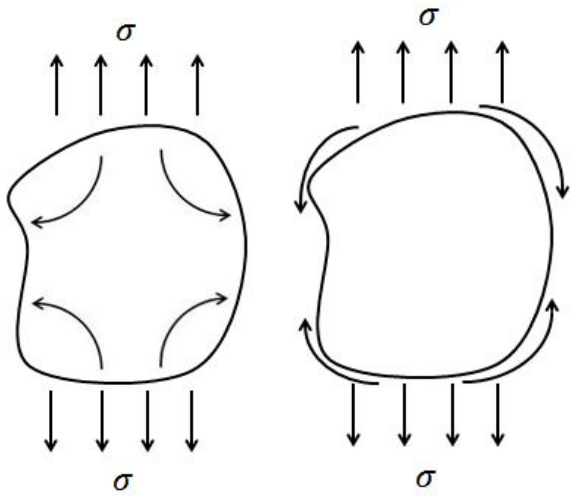

(a) Nabarro-Herring (b) Coble

Figure 2.3: Movement of vacancies in diffusional creep for (a) Nabarro-Herring creep through the grain, and (b) Coble creep along the grain boundaries

2.2.3 Dislocation creep

At relatively higher stresses, creep deformation is believed to be controlled by diffusion movement of dislocations, known as dislocation creep [9]. In this mechanism it has been proposed that dislocation creep is controlled by climb and glide of edge dislocations. Dislocation climb occurs by making use of available vacancies to "climb" and overcome an obstacle. Dislocation glide mechanisms however occur at much higher stresses where the applied stress and thermal energy available is sufficient to overcome an obstacle without climb processes from vacancies [9]. Due to the fact that the stresses and strain rates associated with dislocation creep are so high, it usually falls outside the scope of creep deformation and rather belongs to regimes such as hot working.

2.2.4 Creep deformation maps

To distinguish between different deformation mechanisms involved in creep deformation processes, Ashby [12] developed deformation-mechanism maps. These maps document which plastic deformation mechanisms are active under different combinations of stress and temperature. Each mechanism appears on the map as a field and one can therefore determine the dominant deformation mechanism, and thus the resulting strain rate under specified conditions. These maps are developed for specific materials of specific grain sizes and thus care must be taken to use the correct deformation-mechanism map. An example of such a deformation-mechanism map can be seen in Figure 2.4 where stress normalised by the shear modulus G is plotted against temperature normalised by melting temperature T_m. In this map clear distinction is made between the different deformation mechanisms listed thus far.

Another point worth noting is that creep deformation mechanisms do not remain constant throughout the life of a specimen. A study done by Wilshire and Battenbough

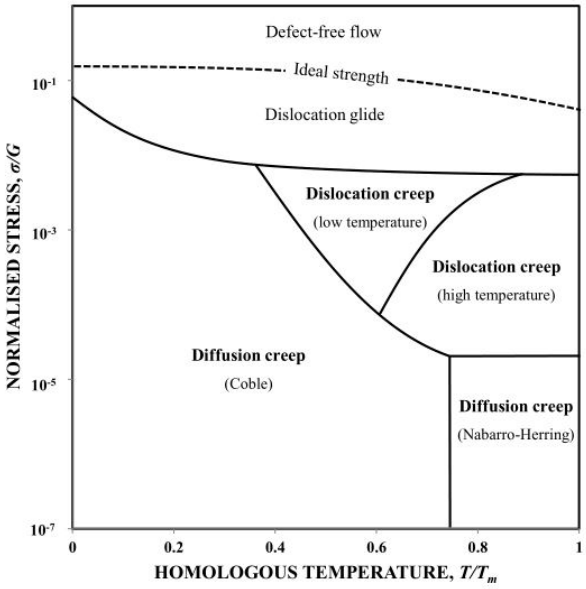

Figure 2.4: Example of deformation-mechanism map [12, 13]

[14] on a fine grained copper specimen found that there was an abrupt change in minimum creep rate gradient as stress varies. This is believed to be due to a change in the dominant creep deformation mechanism. The results of this study are shown in Figure 2.5. Notice that creep strain accumulates in the material at stresses well below the yield stress of the material, verifying that creep strain does in fact accumulate at all non-zero stresses.

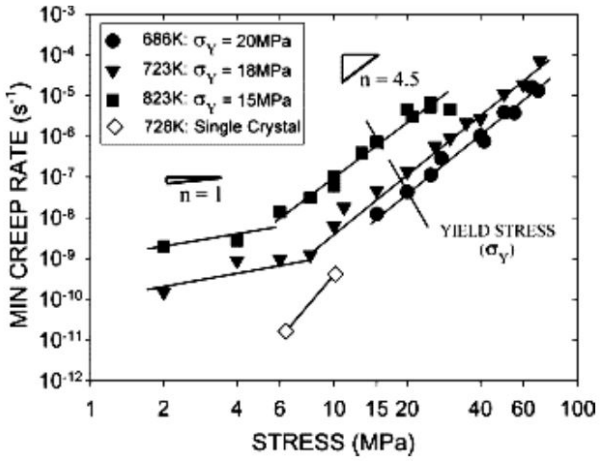

Figure 2.5: Secondary creep strain as a function of applied stress for a fine grained copper specimen [14]

From the above it is apparent that indication of the dominant deformation mechanism in creep deformation is hard to predict. Without the availability of deformation-mechanism maps this task becomes further complicated. This therefore encourages the use of other methods to predict creep deformation.

2.3 Creep damage detection

Quantifying the actual amount of creep strain a component has accumulated over its service life is not only of interest to predicting service life, but also of interest for verification of FE models. The most common non-destructive testing (NDT) method used for assessment of accumulated creep strain is replica metallography. Recently though, drawbacks to the use of microstructural replicas has prompted engineers to investigate other methods such as ultrasonic and electromagnetic methods, hardness measurements and nuclear techniques [4]. The following subsection briefly discusses possible NDT methods for the detection of creep damage. A comprehensive explanation of the theoretical background of the methods falls outside the scope of this thesis and thus is not included here.

2.3.1 Replica metallography

Replication, also called replica metallography, is the most common method used in the assessment of accumulated creep strain of components. A film is applied to a polished surface and lifted to obtain a mirror of the surface [4]. This replica is then analysed under a microscope, where creep damage is quantified by voids per unit area. Figure 2.6 shows an example of a replica for 1Cr-0.5Mo steel.

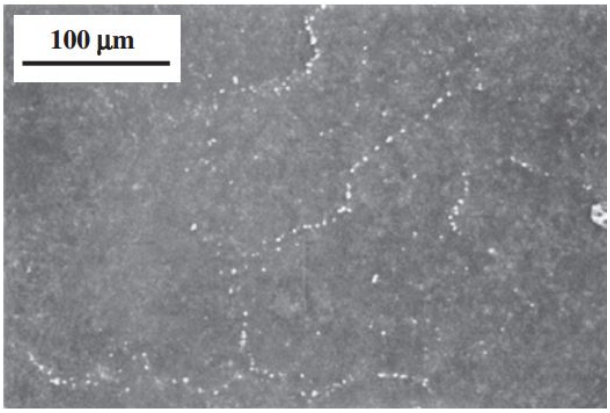

Figure 2.6: Example replica from 1Cr-0.5Mo steel after 168000 h service at 803 K [15]

As one would expect, the drawback to replication methodologies for creep evaluation is that replicas can only be taken during maintenance periods at locations that are easily accessible. Additionally, replication methods cannot be used to detect subsurface defects and thus could lead to potential misdiagnosis. A common assumption made is that voids can be detected from relatively early stages of creep; however some studies have shown that in certain cases cavities are only detectable on the surface shortly before fracture [4], thus making replica metallography techniques unreliable for early detection and quantification of creep strain.

2.3.2 Ultrasonics

Ultrasonic techniques are capable of both internal and surface flaw detection, making these methods capable of volumetric creep inspection [16]. It is however noted that a

considerable drawback to the use of ultrasonics techniques is that they should be carried out at room temperature, which is an obvious problem when dealing with creep. In general, the determination of a flaw using ultrasonics is measured from the echo of an outgoing pulse. Figure 2.7 demonstrates how the presence of a flaw will cause a difference in the wave echo.

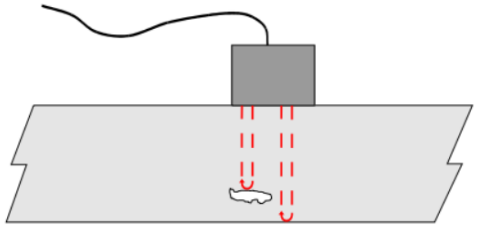

Figure 2.7: Schematic diagram of ultrasonic flaw detection [16]

2.3.3 Magnetic methods

For obvious reasons, magnetic methods are limited to ferromagnetic materials and thus cannot be used for creep detection in materials such as plastic. In principle, magnetic methods work by generating a magnetic flux in the part to be examined. A discontinuity in the flux lines will cause a flux leakage, attracting iron particles to the crack location [16]. Surface cracks are then visible as collections of iron particles. Magnetic methods are therefore only suitable for detection of surface and near surface flaws. A schematic of the process of magnetic flaw detection is shown in Figure 2.8.

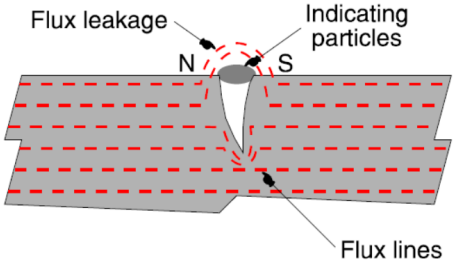

Figure 2.8: Flaw detection using magnetic methods [16]

2.3.4 Hardness measurements

The microstructural changes of a specimen throughout its creep life affect all materials differently. Studies have shown that in Cr-Mo steels (a common power plant material and the subject of this study) the Vickers hardness decreases approximately linearly between 20% and 90% of component creep life, followed by a sudden drop at rupture [4]. It has therefore been proposed that creep can be observed and evaluated by monitoring the change in hardness of a component. However, due to large inaccuracies caused by specimen preparation, site conditions and surface microstructures, this method is not widely used.

2.3.5 Strain measurement

Perhaps the most obvious method is that of strain measurement. Measuring the strain of specific components allows for live time monitoring of the creep condition of said components. These measurements can be used to predict the creep damage of other specimens under similar operating conditions. Various methods are available for strain measurement, with strain gauges being the most accurate method. However, strain gauges are often not suitable for prolonged life at the operating conditions where creep is of concern [4]. A much simpler, and obviously less accurate, method employs the use of markers such as projections or pipes attached to the specimen of interest. The movement of these markers can then be monitored over time.

Component life is then assessed by comparing strain to creep strain limits given by engineering codes, for example [17, 18].

2.4 Creep life prediction

In engineering design it is important to ensure that failure does not occur by either rupture or excessive deformation. At elevated temperatures this is achieved by designing such that the allowable stress does not exceed the rupture stress, which is commonly estimated with a 10^5 - 20^5 h design life at the required operating temperature [19, 20].

Ideally, one would like to base life calculations and failure predictions on long term creep data. The Japanese National Institute for Materials Science (NIMS) has such long term data openly available to the public. However, in cases where such data is not available, the long term creep properties need to be predicted from relatively short duration tests. The problem with accelerated creep tests is that, due to their associated higher temperatures and stresses, there are different deformation mechanisms present. Many parameters have however been developed that are independent of the creep deformation mechanism, with the Larson-Miller parameter being one of the most common ones.

The Larson-Miller (L-M) parameter is a time-temperature parameter that is used to extrapolate long term rupture properties from short duration creep rupture tests. The successful use of the L-M method is based on the argument that for a specific stress there is a single temperature-time compensated parameter. The L-M parameter is given by [21],

$$P_{LM} = f(\sigma) = T(\log t_f + C), \tag{2.3}$$

where the L-M parameter P_{LM} is written in terms of the temperature T, the failure time t_f, and a constant C. When formulating the L-M parameter, the failure time t_f could be defined as either the time to actual material rupture t_r, or alternatively, as the time to reach a specific amount of strain, for example the time to the onset of tertiary creep t_{ter} [22]. The premise of this methodology is that the time-temperature parameter can be plotted against stress, and a polynomial of sufficient order fitted through this data.

This polynomial can then be used to make inferences for other arbitrary temperature and stress combinations. The form of this polynomial is usually given by [10],

$$f(\sigma) = c_0 + c_1 \log(T) + c_2 \log(\sigma)^2 + c_3 \log(\sigma)^3 + c_4 \log(\sigma)^4. \quad (2.4)$$

Other time-temperature parameters, such as the Orr-Sherby-Dorn parameter or Manson-Haferd parameter, also exist [23]. These parameters have their own time-temperature relations. The L-M parameter is however the simplest of the methods.

2.5 Creep resistant materials

The importance of considering creep during the design of components subjected to loads at elevated temperatures is clear. More specifically, components in power plants need to be designed with creep in mind. The efficiency of steam turbines is directly related to the inlet temperature and pressure of the steam, and can be increased by raising this inlet temperature and pressure. It is for this reason that creep resistant steels are extremely important in power stations.

Creep resistant steels are those which are designed to withstand loads at high temperatures, for prolonged periods of time. Boilers and boiler pipes, turbine blades and casings, as well as casing bolts are all examples of components which are susceptible to creep in power plants [24]. As a result of the long life times required by such components, the selection of proper creep resistant steels is important to ensure failure does not occur during operating life.

In the early 1900s the use of non-alloyed steels allowed inlet conditions of approximately 1.5 MPa and 350°C in turbines. At the beginning of the 1920s the design of low alloyed steels developed increasing interest, with these steels allowing for inlet conditions of around 3.5 MPa and 450°C [25]. The high creep resistance of these low alloyed steels is due to the precipitation and solid solution strengthening resulting from the addition of alloying elements of Cr, Mo, V, Nb, Ti and B. Various steel versions have been developed over the years, with the 1Cr-Mo-V being the most commonly used in the manufacturing of turbine rotors, casings, valves and bolts [23, 25]. Figure 2.9 shows the maximum operating temperatures of some of the creep resistant steels developed to date. It can be seen that the maximum operating temperatures vary quite significantly for the different materials. Caution must thus be exercised when selecting a grade of steel for a component.

The 1CrMoV alloy is the most widely used creep resistant steel and finds widely accepted use in the power generation sector, specifically in steam turbines. This alloy is commonly used for components such as HP and IP turbines, where service temperatures can reach up to 565°C [25]. Various chemical compositions of the alloy exist depending on the size and location of the part. Typically these chemical compositions are roughly 0.2-0.3%C, 1-1.5%Cr, 0.7-1.25%Mo, 0.25-0.35%V and 0.5-0.75%Ni [23].

Developments in creep resistant steels have allowed for increases in inlet steam properties to approximately 30 MPa and 620°C in [25]. Figure 2.9 shows that the various

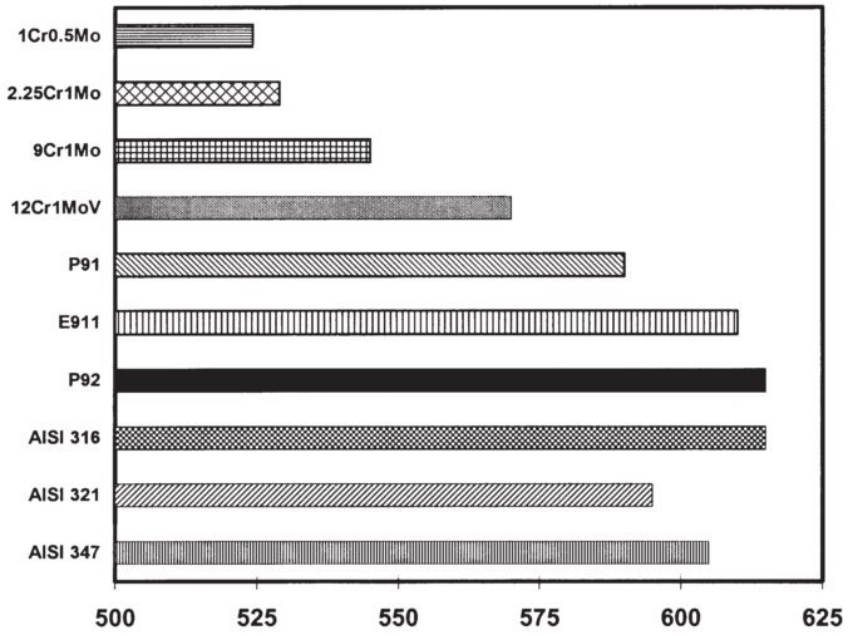

Figure 2.9: Maximum operating temperature ($^{\circ}C$) of various creep resistant steels, based on 10^5 h average stress rupture strength of 100MPa [26]

creep resistant steels available have a wide range of maximum operating temperatures. Choice of the correct steel for use in the correct component is therefore of the utmost importance. Table 2.1 shows the creep resistant steels commonly used in the different components of a steam turbine plant.

Table 2.1: Steam turbine components requiring creep resistant materials [24]

	Inlet steam conditions		
Component	18MPa, $540^{\circ}C$	24MPa, $565^{\circ}C$	30MPa, $600^{\circ}C$
Rotor	1CrMoV, 2CrNiMoWV	1CrMoV, 2CrNiMoWV	10CrMoVNb
Blades	12CrMoV	12CrMoVNb, Alloy-80A	11CrMoVNb, Alloy-80A
Casings	$2\frac{1}{4}$CrMo, $\frac{1}{2}$CrMoV, 1CrMoV	$\frac{1}{2}$CrMoV, 1CrMoV, 9CrMoVNb	9CrMoVNb
Casing bolts	1CrMoVTiB, 12CrMoVNb	1CrMoVTiB, 12CrMoVNb, Alloy-80A	11CrMoVNb, Alloy-80A
Piping	$2\frac{1}{4}$CrMo, $\frac{1}{2}$CrMoV, 1CrMoV	$\frac{1}{2}$CrMoV, 1CrMoV, 9CrMoVNb	9CrMoVNb

2.6 Mathematical models

2.6.1 Constitutive creep models

Constitutive equations characterise the response of materials to applied loading, material state, and environmental conditions. These material models are necessary inputs to analysis, including FEA. In the simulation of the long term creep behaviour of structures operating at elevated temperatures, we make use of constitutive models for both the creep strain and the creep strain rate. Creep strain constitutive models relate the creep strain ε_{cr} to time t, operating temperature T, and local stress σ in the form $\varepsilon_{cr} = f(t, T, \sigma)$. Creep strain rate models can also include the creep strain as a

variable, $\dot{\varepsilon}_{cr} = f(\varepsilon, t, T, \sigma)$ [27]. Various constitutive models are available to represent the creep behaviour of engineering materials at elevated temperatures, in which each regime (primary, secondary and tertiary) is usually modelled separately. Total creep strain can then be modelled with a weighted addition of various models, in order to obtain a fully defined creep curve. The purpose of this section is not to give an exhaustive breakdown of all creep constitutive models that are available, but rather to touch on the more common models and demonstrate the basics behind the formulations of such models.

A summary of some of the most common ***primary creep*** models is given in Table 2.2. All of these models have the capability of representing the decreasing creep strain rate that occurs in the primary creep regime over time t. The rate of this decrease and magnitude of the accumulated creep strain is adjusted by the constants A, B and c. An interesting fact regarding the primary creep models is that they all, barring the exponential model, have the ability to model secondary creep as well. In the special case in which the deformation mechanism does not change between the primary and secondary creep regimes this could prove to be useful.

Table 2.2: Constitutive models for primary creep [27]

Model	Constitutive equation
Logarithmic [28]	$\varepsilon = A\log(1 + Bt)$
Power [29]	$\varepsilon = At^c$
Exponential [30]	$\varepsilon = A[1 - \exp(-Bt)]$
Hyperbolic sine [31]	$\varepsilon = A\sinh(Bt^c)$

In a similar fashion the steady state creep rate $\dot{\varepsilon}_{min}$ of ***secondary creep*** can also be represented by power, exponential or hyperbolic sine functions of stress. The classical form of these equations is tabulated in Table 2.3.

Table 2.3: Constitutive models for secondary creep [27]

Model	Constitutive equation
Power [32]	$\dot{\varepsilon}_{min} = A\sigma^n$
Exponential [33]	$\dot{\varepsilon}_{min} = A\exp(B\sigma)$
Hyperbolic sine [33]	$\dot{\varepsilon}_{min} = A\sinh(B\sigma)$

Tertiary creep models are rare due to this regime's association with failure. However, when necessary, a damage parameter is often used in conjunction with power or exponential functions (i.e.: [34, 35, 36]) to model this often short lived regime. These models will be discussed further in Section 2.7.

It is worth noting that there is not one single creep model that is best suited for all creep problems, rather a model is chosen that best fits the available data. Due to the long time frames associated with creep, it is often hard to obtain usable creep data. In order to obtain correct estimations for constitutive creep model coefficients the analyst

will often need to do a considerable amount of work with the use of justified assumptions.

Commonly, an engineer will make use of the simplest creep model and add complexity to the model as necessary. One of the most common models used is the secondary power law creep model. This model however does not account for changes in dominant deformation mechanism that are accompanied by a varying stress (i.e.: Figure 2.5). In these scenarios a solution would be to use a switching creep model, in which the model parameters are varied according to the current conditions. This is represented by [23],

$$\dot{\varepsilon}_{min} = \begin{cases} A_1\sigma^{n_1}, & \text{if } \sigma \leq \sigma^* \\ A_2\sigma^{n_2}, & \text{if } \sigma > \sigma^*, \end{cases} \tag{2.5}$$

where σ is the stress and σ^* is the switching condition. This formulation can be modified to a more physical model, in which the deformation mechanism gradually changes as the stress approaches the switching stress. This is represented by [23],

$$\dot{\varepsilon}_{min} = A_1\sigma^{n_1} + A_2\sigma^{n_2}. \tag{2.6}$$

A comparison of these approaches is shown in Figure 2.10. Here it can be clearly seen that a switching model results in an abrupt change in stress exponent n, which is seen as the gradient of the curve. The smooth switching model more closely represents what one would expect to see during a deformation mechanism change.

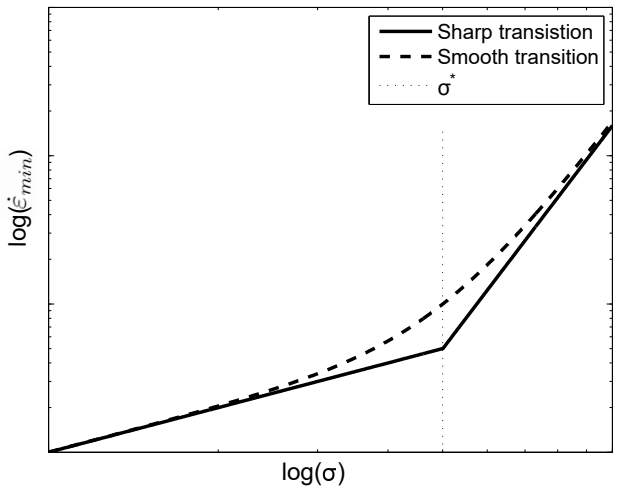

Figure 2.10: Comparison of power law creep models given in Equations 2.5 and 2.6

2.6.2 Reduced normalised models

The Larson-Miller, Sherby-Dorn and Manson-Haferd parameters have shown good results for design purposes when attempting to approximate creep life. Wilshire and Scharning [37] have however proposed a different method of predicting the long term

creep data from available experimental creep data. The authors proposed that the behaviour patterns of a material could be defined in terms of just a few standard parameters, which can be simply monitored and measured. In order to do this the authors made use of the available NIMS creep data for 1Cr-1Mo-0.25V steel forgings [38], and attempted to characterize the experimental data with three "master curves".

The first master curve attempts to predict the long term stress rupture data. In order to create a master curve for all available data, the stress σ was normalised by the correct ultimate tensile strength σ_{UTS} and the activation energy Q normalised to a single value of $Q^* = 300\text{kJmol}^{-1}$, which is the expected value for alloy steels. The master curve is given by [37],

$$\sigma/\sigma_{UTS} = e^{-k_1[t_f e^{-Q^*/RT}]^u}, \tag{2.7}$$

where t_r is the time to fracture, and k_1 and u are constants determined for different levels of applied stress.

Similar master curves were developed for the prediction of the steady state creep strain rate $\dot{\varepsilon}_{min}$ and time to specific strain t_ε. These are given by [37],

$$\sigma/\sigma_{UTS} = e^{-k_2[\dot{\varepsilon}_{min} e^{-Q^*/RT}]^v}, \tag{2.8}$$

$$\sigma/\sigma_{UTS} = e^{-k_3[t_\varepsilon e^{-Q^*/RT}]^w}, \tag{2.9}$$

where k_2, k_3, v and w are again constants that are to be determined.

As an example consider the application of Equation 2.9 shown in Figure 2.11. Here it can be seen that when the correct constants are determined, the master curves can be derived with good correlation to the experimental data.

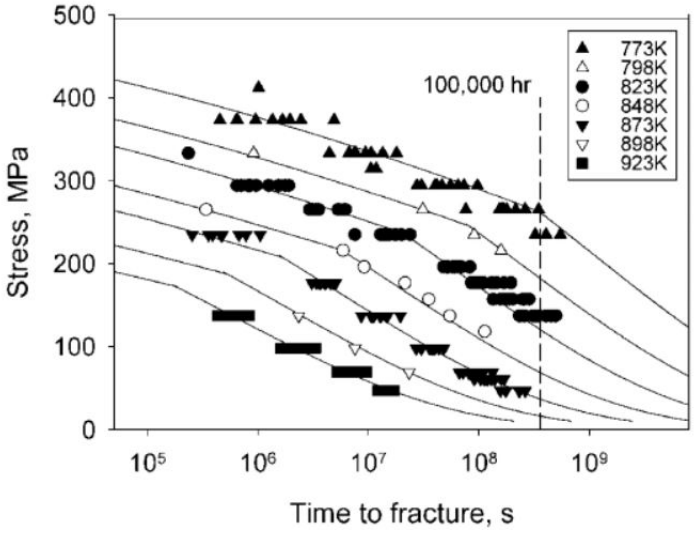

Figure 2.11: Master curves describing the time to specific strain values [37]

From the results it can be seen that the creep data is characterised relatively well. These three master curves, denoted as the Wilshire curves, have shown promise for other alloys such as 1Cr-0.5Mo, 2.25Cr-1Mo and 9Cr steels [39]. These equations therefore offer an alternative approach to calculation of creep and creep fracture. These equations can be implemented into commercial FE code with the use of user programmed subroutines. This is however outside the scope of this thesis, and will not be investigated further.

2.7 FE modelling of creep

2.7.1 Previous work

The use of Finite Element (FE) software to model the behaviour of materials at higher temperatures allows engineers to make informed decisions on the remaining useful life of components, as well as analyse failures to improve future designs. Effectively modelling creep using Finite Element Analysis (FEA) allows engineers to obtain time-efficient results of accumulated creep strain and stress distributions within components, eliminating the need for the costly and time consuming methods outlined in Section 2.3.

To date, many authors have done work in developing FE creep models, most of which incorporate a damage model to account for the tertiary creep regime that leads to eventual failure. The majority of these damage models make use of a scalar creep damage parameter ω which varies between $\omega = 0$ (no damage) and $\omega = 1$ (fully damaged) [34, 35, 36, 40]. Becker et al. [35] defined the evolution of this damage parameter with the time rate formula given by [35],

$$\frac{d\omega}{dt} = A\frac{\sigma_r^{\chi}}{(1+\phi)(1-\omega)^{\phi}}t^m, \tag{2.10}$$

where A, χ, ϕ and m are model coefficients that need to be determined, and σ_r is the rupture stress.

The damage parameter is then used to calculate the updated creep strain at each time step. The uniaxial form of this strain update is given by [35],

$$\frac{d\varepsilon_{cr}}{dt} = B\left(\frac{\sigma}{1-\omega}\right)^n t^m, \tag{2.11}$$

where B and n are again model coefficients that need to be determined. Note the resemblence of Equation 2.11 to the simple power law model for both the primary ($\varepsilon_{cr} = At^c$ from Table 2.2) and secondary ($\dot{\varepsilon}_{cr} = A\sigma^n$ from Table 2.3) creep regimes. This model is capable of capturing a primary and secondary creep response with the multiplicative power law, as well as tertiary creep with its damage accumulation parameter.

The results from these damage models have shown good correlation with experimental data. The benefit to using the damage parameter ω is that the time to failure can

be analysed by the time for ω to reach some upper threshold. Figure 2.12 shows an example from a study done on a notched bar at elevated temperatures where the distribution of the damage parameter ω is shown [34]. Analyses like this make it possible to determine at what time the damage parameter reaches a critical value, and where this occurs.

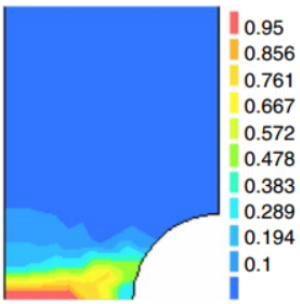

Figure 2.12: Distribution of damage parameter ω from FE study of a notched bar[34]

Such damage models are rarely included in commercial FEA code, and users need to make use of either in-house FE code, or user subroutines to explicitly calculate damage parameters and input them back into creep strain calculations. Most commercial codes do offer this functionality, however users have to be very knowledgeable in the software to obtain accurate, converged results. This is however outside the scope of this work, and only the built in commercial code models will be investigated.

The ANSYS FEA package, for example, does not make use of these damage models. Rather, creep is included in a problem through the use of creep strain material models. Ellis and Zielke [41] have shown that, through the use of optimisation, these models can be used to accurately predict the creep behaviour of materials. Figure 2.13 shows the comparison of one of these creep strain models to a set of experimental creep data. It can be seen that the model is able to accurately predict the creep strain data for a variety of stresses.

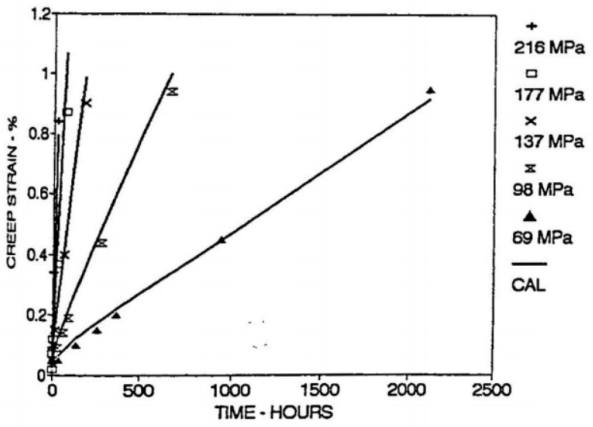

Figure 2.13: Comparison of ANSYS creep strain model to experimental data at 823 K and varying stresses [41]

2.7.2 ANSYS FE code

Thus far it has been shown that there are various methods available to model creep. The use of creep constitutive models with some sort of damage parameter has proved to be a popular technique from literature. This Section will discuss the modelling of creep using commercial FEA code, where the use of pre-developed models becomes more appealing. FE codes such as NASTRAN and ABAQUS are some examples of the available software. However, predefined outcomes for this thesis require the use of ANSYS, and hence only the use of ANSYS FEA software will be discussed.

As mentioned, ANSYS makes use of strain based creep material models, as opposed to the damage based creep models. These strain based material models make use of the additive strain decomposition when calculating elastic, plastic and creep strain. This additive law is given by [42],

$$\dot{\varepsilon}_{tot} = \dot{\varepsilon}_{el} + \dot{\varepsilon}_{pl} + \dot{\varepsilon}_{cr}, \tag{2.12}$$

where each strain component is calculated separately. The stress-strain relationship is then given by [42],

$$\dot{\sigma} = D : \dot{\varepsilon}_{el}, \tag{2.13}$$

where D is the elasticity matrix. An important note is that the elastic, plastic and creep strains are calculated independently, and do not affect each other in any way. The creep strain rate is therefore explicitly defined as $\dot{\varepsilon}_{cr} = f(t, T, \sigma, \varepsilon)$, or creep strain models as $\varepsilon_{cr} = f(t, T, \sigma)$, where the specific form is dependent on the material being modelled, as well as the available experimental data.

ANSYS has 13 available creep models that are capable of modelling either primary creep, secondary creep, or both primary and secondary creep. ANSYS does not attempt to model tertiary creep due to its association with failure. The tertiary creep regime is also associated with large strains, and hence large element distortions. This leads to additional convergence issues, further complicating the analysis.

Before presenting the 13 creep models available in ANSYS it is worth discussing some common features amongst all the models. Due to the fact that creep effects are thermally activated, the temperature dependence of the process is usually represented through the Arrhenius law, represented by [43],

$$\dot{\varepsilon}_{cr} \propto \exp\left(-\frac{Q}{RT}\right), \tag{2.14}$$

where Q is the activation energy for creep, R is the universal gas constant, and T is the absolute temperature. Similarly, the stress dependency of the creep process is represented with a power law relation of the form given by,

$$\dot{\varepsilon}_{cr} \propto \sigma^n, \tag{2.15}$$

where n is known as the stress sensitivity exponent, and needs to be determined from experimental data. When considering primary creep, ANSYS makes use of either a

time-hardening or strain-hardening model to account for the decreasing creep strain rate. The time-hardening and strain-hardening are given respectively by,

$$\dot{\varepsilon}_{cr} \propto t^{m_1}, \tag{2.16}$$
$$\dot{\varepsilon}_{cr} \propto \varepsilon^{m_2}, \tag{2.17}$$

where m_1 and m_2 are again sensitivity exponents that need to be determined. Note that in order to model a decreasing creep strain rate these sensitivity exponents need to be negative.

With the above background, consider the 13 available creep models listed in Table 2.4, where x_1, x_2, ..., x_{12} are model coefficients that need to be determined by the user. It can be seen that the models presented here have several similarities to the constitutive models presented in Section 2.6.1. Also shown is the specific creep regime represented by the model. Here it can be seen that the primary creep models all contain a time-dependent term which is used to model the decreasing strain rate over time.

When picking the correct ANSYS model many factors have to be considered. Perhaps the most influential factor when deciding on an adequate model is the form of experimental data available for use to determine the required model coefficients. The ANSYS creep models in Table 2.4 are discussed in more detail in the following subsections.

Strain hardening ($\dot{\varepsilon}_{cr} = x_1\sigma^{x_2}\varepsilon^{x_3}e^{-x_4/T}$) The strain hardening model contains both Norton's law (power law) and a strain hardening term. In order for the model to capture the decreasing strain rate of the primary regime, the constant x_3 is usually negative. Also to be noted is that the model can capture some of the secondary regime because as time increases the creep strain rate approaches a constant value. The constant x_4 is used to model the temperature dependency of the problem.

Creep strain rate is written implicitly as a function of creep strain. The creep strain rate is therefore dependent on the strain history and thus use of this model would usually require one to have creep strain and creep strain rate experimental data available. This is rarely the case, limiting the use of this model to special cases where specialised experimental tests are conducted that allow one to record strain as well as strain rate.

Time hardening ($\dot{\varepsilon}_{cr} = x_1\sigma^{x_2}t^{x_3}e^{-x_4/T}$) The time hardening model contains the Arrhenius equation, Norton's law, and a time hardening term. Again the constant x_3 is usually negative to model the decreasing strain rate with time, with a value between -0.5 and -1.0. The time hardening model can also model a significant portion of the secondary creep regime for the same reasons as above. The constant x_4 is again used to model the temperature dependency of the problem.

The time hardening model is a lot more flexible in terms of required experimental data. Only creep strain rate data over time is required to fit the required model coefficients. Additionally this model can be integrated with respect to time, to require only creep

Table 2.4: Summary of available ANSYS creep models [42]

	Name	Equation	Regime
1	Strain hardening	$\dot{\varepsilon}_{cr} = x_1 \sigma^{x_2} \varepsilon_{cr}^{x_3} e^{-x_4/T}$	Primary
2	Time hardening	$\dot{\varepsilon}_{cr} = x_1 \sigma^{x_2} t^{x_3} e^{-x_4/T}$	Primary
3	Generalised exponential	$\dot{\varepsilon}_{cr} = x_1 \sigma^{x_2} r e^{-r/T}$ $r = x_5 \sigma^{x_3} e^{-x_4/T}$	Primary
4	Generalised Graham	$\dot{\varepsilon}_{cr} = x_1 \sigma^{x_2} \left(t^{x_3} + x_4 t^{x_5} + x_6 t^{x_7}\right) e^{-x_8/T}$	Primary
5	Generalised Blackburn	$\dot{\varepsilon}_{cr} = f(1 - e^{-rt}) + gt$ $f = x_1 e^{x_2 \sigma},\ r = x_3 (\sigma / x_4)^{x_5},\ g = x_6 e^{x_7 \sigma}$	Primary
6	Modified time hardening	$\varepsilon_{cr} = x_1 \sigma^{x_2} t^{x_3+1} e^{-x_4/T} / (x_3 + 1)$	Primary
7	Modified strain hardening	$\dot{\varepsilon}_{cr} = \left(x_1 \sigma^{x_2} [(x_3 + 1)\varepsilon_{cr}]^{x_3}\right)^{1/(x_3+1)} e^{-x_4/T}$	Primary
8	Generalised Garofalo	$\dot{\varepsilon}_{cr} = x_1 \left[sinh(x_2 \sigma)\right]^{x_3} e^{-x_4/T}$	Secondary
9	Exponential form	$\dot{\varepsilon}_{cr} = x_1 e^{\sigma/x_2} e^{-x_3/T}$	Secondary
10	Norton	$\dot{\varepsilon}_{cr} = x_1 \sigma^{x_2} e^{-x_3/T}$	Secondary
11	Combined time hardening	$\varepsilon_{cr} = x_1 \sigma^{x_2} t^{x_3+1} e^{-x_4/T} / (x_3 + 1) + x_5 \sigma^{x_6} t e^{-x_7/T}$	Both
12	Rational polynomial	$\dot{\varepsilon}_{cr} = x_1 \dfrac{\partial \varepsilon_c}{\partial t}$ $\varepsilon_c = \dfrac{cpt}{1 + pt} + \dot{\varepsilon}_m t$ $\dot{\varepsilon}_m = x_2 10^{x_3 \sigma} \sigma^{x_4}$ $c = x_7 \dot{\varepsilon}_m^{x_8} \sigma^{x_9},\ p = x_{10} \dot{\varepsilon}_m^{x_{11}} \sigma^{x_{12}}$	Both
13	Generalised time hardening	$\dot{\varepsilon}_{cr} = f t^r e^{-x_6/T}$ $f = x_1 \sigma + x_2 \sigma^2 + x_3 \sigma^3$ $r = x_4 + x_5 \sigma$	Primary

strain over time experimental data.

Generalised exponential ($\dot{\varepsilon}_{cr} = x_1 \sigma^{x_2} r e^{-r/T}$) The generalised exponential law is one of the variations of a time hardening creep law. Here the decreasing strain rate is modelled with an exponential term that decreases as time increases. The rate at which this decrease occurs depends on the coefficients chosen. The constant x_4 is again used to model the temperature dependency of the problem.

When looking at the function $r = x_5 \sigma^{x_3} e^{-x_4/T}$, it is seen that stress appears in the exponential term. This therefore requires that the coefficient x_5 be chosen such that the exponential power is close to unity to avoid overtaking effects of this term. This is

possible for cases where the stress range is small. However, for cases where the stress range of interest is large, this coefficient will be unable to reduce the exponential power to unity over the entire stress range.

Generalised Graham ($\dot{\varepsilon}_{cr} = x_1\sigma^{x_2}\left(t^{x_3} + x_4 t^{x_5} + x_6 t^{x_7}\right) e^{-x_8/T}$) The generalised Graham model is another variant of the time hardening model. The decreasing strain rate is modelled with negative coefficients for x_3, x_5 and x_7. Here the constant x_8 is used to model the temperature dependency of the problem.

The multiple time exponents in this model will allow for more flexibility in modelling the decaying strain rate of the primary regime. This model will therefore be useful for primary regimes that have a significantly complex primary creep regime, where a single time exponent cannot accurately capture the decaying strain rate.

Generalised Blackburn ($\dot{\varepsilon}_{cr} = f(1 - e^{-rt}) + gt$) Similarly to the generalised exponential model, the generalised Blackburn model is a variant of the time hardening model that uses an exponential function to model the decreasing strain rate. This model does not not have a term that can be used to model temperature dependency of the problem.

Similar to the generalised exponential model, the functions f, r and g require the coefficients to attain values such that unity is obtained when multiplying with stress. This therefore means the model is limited to small stress ranges, as large stress ranges will lead to overpowering terms.

Modified time hardening ($\varepsilon_{cr} = x_1\sigma^{x_2}t^{x_3+1}e^{-x_4/T}/(x_3+1)$) Upon close inspection of the modified time hardening model it can be seen that the model is simply the integrated form of the original time hardening model. The model therefore has creep strain as the subject of the equation, as opposed to creep strain rate in the time hardening model. The constant x_4 is again used to model the temperature dependency of the problem.

Modified strain hardening ($\dot{\varepsilon}_{cr} = \left(x_1\sigma^{x_2}[(x_3+1)\varepsilon_{cr}]^{x_3}\right)^{1/(x_3+1)} e^{-x_4/T}$) The modified strain hardening model is a variant of the original strain hardening model. The constant x_3 is again usually negative to modelling the strain hardening that takes place as time increases. Once again, the constant x_4 is used to model the temperature dependency of the problem. Due to the model's similarity to the original strain hardening model, it suffers from the same drawbacks as previously noted.

Generalised Garofalo ($\dot{\varepsilon}_{cr} = x_1\left[sinh(x_2\sigma)\right]^{x_3} e^{-x_4/T}$**)** The generalised Garofalo model does not include any time or strain hardening dependence and thus is used to model the secondary creep regime where the strain rate is approximately constant. The constant x_4 is used to model the temperature dependency of the problem.

The hyperbolic sine term should be kept close to unity to avoid dominating explosive affects. This means that the stress range of interest is limited, with large stress ranges leading to either under or overestimating creep strain rate.

Exponential form ($\dot{\varepsilon}_{cr} = x_1 e^{\sigma/x_2} e^{-x_3/T}$) The exponential form model is another model that doesn't include any time or strain hardening dependence and thus is used to model the approximate constant steady state creep strain rate in the secondary regime. Here the constant x_3 is used to model the temperature dependency of the problem.

In order to avoid dominating exponential affects, the exponential term should be kept close to unity. For the same reasons as previously discussed, the model should be used for small stress ranges of interest.

Norton ($\dot{\varepsilon}_{cr} = x_1 \sigma^{x_2} e^{-x_3/T}$) The Norton model is the last model used to model the approximately constant steady state creep strain rate in the secondary regime. This model is probably considered the simplest of all secondary models, where the constant x_2 is the stress sensitivity parameter discussed in previous sections. The constant x_3 is again used to model the temperature dependency of the problem. The Norton model is possibly the most widely used secondary creep model, and sees common use in most theoretical creep life and design calculations.

Combined time hardening ($\varepsilon_{cr} = x_1 \sigma^{x_2} t^{x_3+1} e^{-x_4/T}/(x_3+1) + x_5 \sigma^{x_6} t e^{-x_7/T}$) The combined time hardening law is the first law that is capable of modelling both the primary and secondary creep regimes. It can be seen that the model incorporates both a time hardening and Norton model. As time increases the time hardening component decays away, leaving Norton's model for the secondary creep regime.

Theoretically this is the most promising model, being able to capture both primary and secondary effects. The inclusion of both primary and secondary models allows one to more accurately capture the creep curve where primary or secondary models alone are unable to do so.

Rational polynomial ($\dot{\varepsilon}_{cr} = x_1 \frac{\partial \varepsilon_c}{\partial t}$) The rational polynomial model is possibly the most complex of all the models discussed. It is the second and last model that can be used to model both the primary and secondary creep regimes. Its over complexity is often its downfall, with the complexity allowing almost any curve to be approximated. For this reason the model is usually limited to metals in the nuclear industry, where other models are unable to capture the complexities of the creep curves.

Generalised time hardening ($\dot{\varepsilon}_{cr} = f t^r e^{-x_6/T}$) The generalised time hardening model is a variation of the original time hardening model which can be used to model the primary creep regime. The exponential constant for time is again usually negative to model decreasing strain rate with time. Here, the constant x_6 is used to model the temperature dependency of the problem. It is noted from the equation that there is no coefficient for the stress sensitivity exponent, which can lead to problems in accurately modelling the stress dependency of the creep curve. This model should therefore be used in cases where a low stress sensitivity is present.

2.8 Determination of model parameters

Modelling of creep requires the determination of model coefficients for the chosen model. Depending on the complexity of the model chosen, and the available experimental data, these coefficients can either be determined directly from the experimental data with analytical methods, or through the use of optimisation algorithms. The following subsections will discuss the use of optimisation to determine these model parameters. The theory reported in this section is heavily based on the optimisation theory presented by Arora [44].

Optimisation is defined as a mathematical technique of finding a maximum or minimum value of a function of several variables subject to a set of constraints. When attempting to fit a curve through a set of data points this function is usually written in the form of a cost function, which is the difference between the function approximation and the experimental data points. This cost function is then iteratively decreased in order to find a minimum.

The most commonly used cost function is the Least Squares Error (LSE) which can be described by Equation 2.18,

$$LSE = \sum_{i=1}^{N} \left(data_i - f(\boldsymbol{x}_i)\right)^2, \tag{2.18}$$

where the square difference between the i^{th} experimental data point and the function approximation at this point is summed over all N experimental data points. The set of coefficients that results in a minimised LSE is then considered the converged solution $\boldsymbol{x}^*$. This is demonstrated in Figure 2.14 where the function $y = mx$ is fitted through the experimental data by minimising the LSE.

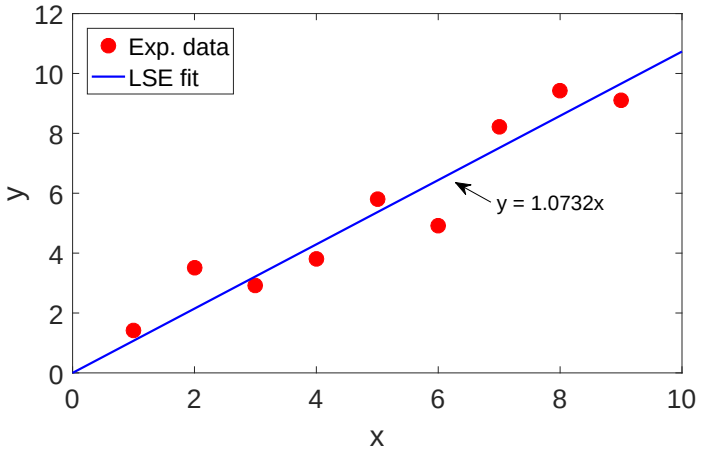

Figure 2.14: Regression line through experimental data using LSE cost function

Consider a plot of the LSE for this sample problem shown in Figure 2.15. Here it can clearly be seen that the converged solution of $m = 1.0732$ is located at the minimum of the LSE.

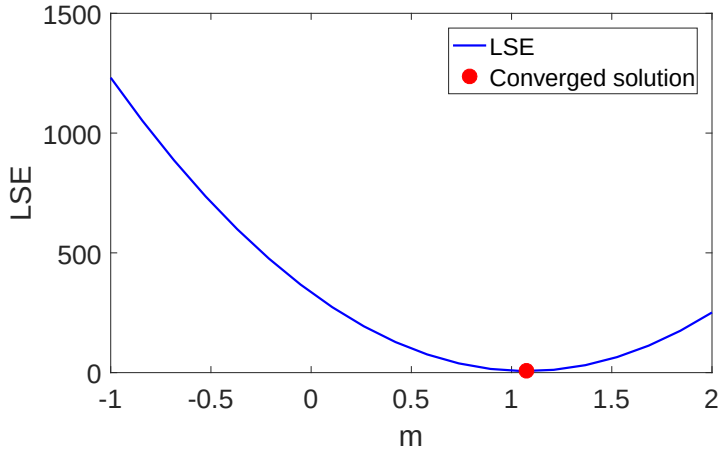

Figure 2.15: LSE for sample problem

The following subsections will discuss a few of the key points outlining the optimisation procedure. It should be noted that the purpose of these sections is not to give a detailed overview of optimisation, but rather to touch on a few of the key concepts.

2.8.1 Search methods

Search methods broadly refer to the methods used to locate a local minimum for the cost function. Two of the most common methods will be discussed here, namely *gradient based search methods* and *direct search methods*.

Gradient based search methods make use of the cost function gradient to search for a minimum. These gradients can either be calculated analytically, or approximated using methods, such as forward difference or central difference approximations. Due to these methods' dependence on function gradients, it is a requirement that the function is smooth and at least twice continuously differentiable around the feasible domain.

Direct search methods on the other hand do not make use of gradients in searching for a minimum. These methods only make use of function values in the search process, and are therefore significantly cheaper computationally. Additionally, these methods require less information, and can therefore be quickly implemented in scenarios where there is not much experimental data available.

2.8.2 Problem constraints

Problem constraints refer to the constraints on the function variables that need to be solved. These constraints can be in the form of either inequalities, which set limits on the maximum or minimum values of coefficients, or equality constraints which fix coefficient values to specific user requirements. These constraints effectively reduce the size of the design space to a space containing only predefined feasible solutions.

Unconstrained optimisation algorithms on the other hand refer to the complete freedom of variable solutions. Variables are not constrained in any way, resulting in an infinitely wide design space.

2.8.3 Stop criterion

The stopping criterion is the tolerance set by the user to terminate the optimisation algorithm at a local or global minimum. The most common tolerance is the tolerance on the change in function value or function gradient value. It is assumed that once this change is less than a specified tolerance, the optimisation algorithm reached either a local or global minimum.

Care must be taken to ensure that optimisation algorithms have converged at a global minimum and not a local minimum. A global minimum is defined when $f(\boldsymbol{x}^*) < f(\boldsymbol{x})$ for any point in the feasible domain. A local minimum on the other hand is defined when $f(\boldsymbol{x}^*) < f(\boldsymbol{x})$ for any point in a small vicinity of $\boldsymbol{x}^*$. This is depicted in Figure 2.16.

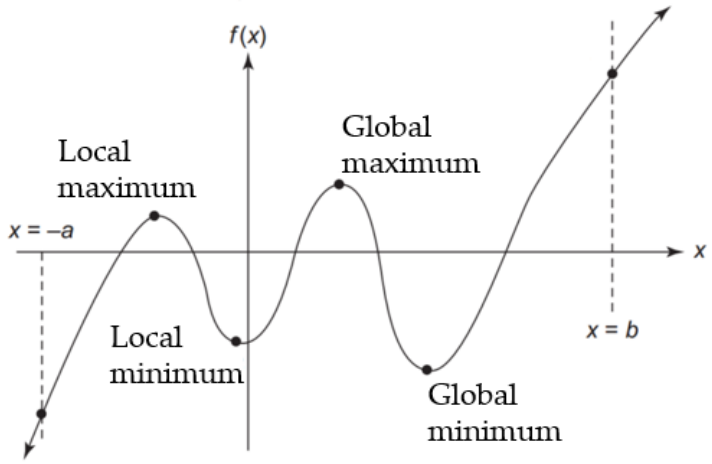

Figure 2.16: Illustration of local and global function properties, adapted from [44]

Chapter 3

Creep model characterisation

The accuracy of FE creep models depends on the accuracy of the chosen creep model. It has been seen that there are various methods in place to model creep using FE methods. ANSYS makes use of strain based creep models to calculate updated displacements and stresses over time. This chapter will focus on the use of optimisation techniques to obtain the creep material models capable of representing the available experimental data.

3.1 Experimental data

3.1.1 The problem

The time scales associated with creep can be in excess of 100kh (>10 years), making creep experiments extremely long. This inevitably means that long term experimental creep results are extremely rare and hard to come by. This problem is commonly solved by the use of accelerated creep tests. However, the results from these tests require extrapolation techniques such as the Larson-Miller calculations briefly described in the literature overview. In order to create accurate constitutive creep models, long term creep data is required. For this reason the author has decided to use the openly available creep data supplied by the Japanese National Institute for Material Science (NIMS). More specifically, the NIMS data base for 1Cr-1Mo-0.25V cast alloy steel will be used. This is a commonly used steel in the manufacturing of turbine casings and valves, and is the material specification of the component being analysed in this research.

The NIMS data base is one of the largest in the world, with the launch of 100kh creep rupture tests in 1966. Access to this experimental creep data allows for the use of creep models which require long term creep data, allowing for a wider variety of models to be used.

3.1.2 NIMS creep database

Variations between casting processes result in a variation of material properties. This is due to the different tempering rates which, in short, result in different grain sizes. This can lead to different material properties for “paper equivalent” materials ordered from different manufacturers. Additionally, when casting large parts, different areas of the part are exposed to different cooling and tempering rates, leading to a natural material property variation through the part. In order to take this into account the experimental

data from NIMS is presented for nine different castings, all having undergone different tempering processes. These casting specifications can be found in Appendix A. For the purpose of further discussion one needs only consider the names of these castings, which are VbA, VbB, VbD, VbF, VbG, VbH, VbJ, VbM and VbN.

Consider the IP valve of interest, shown in Figure 3.1. It can be seen that the component has dimensions greater than 1 m, with an average wall thickness of approximately 80 mm. It is therefore not hard to imagine that an alloy steel component of these large dimensions will experience different cooling and tempering rates throughout the casting process.

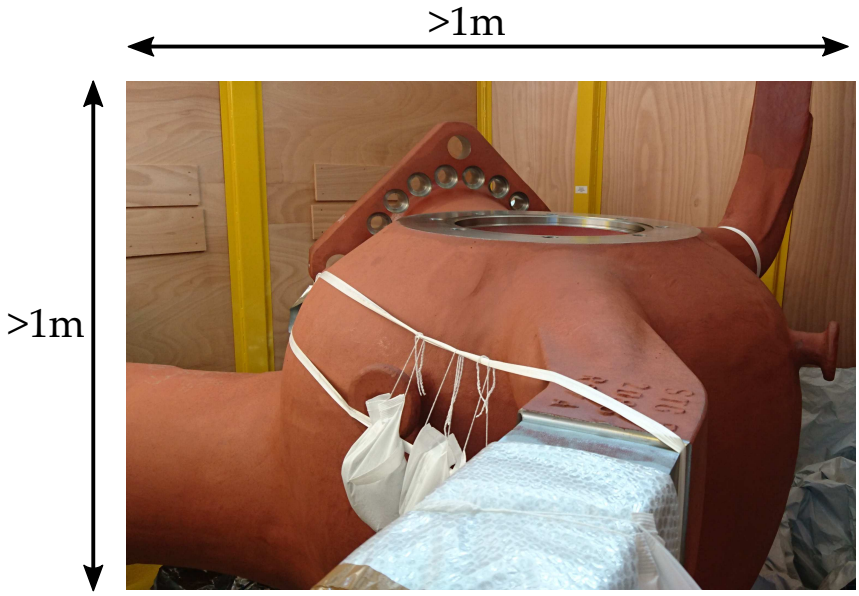

Figure 3.1: Photo of IP valve of interest

In order to fit constitutive creep models ($\varepsilon_{cr} = f(t, T, \sigma)$, $\dot{\varepsilon}_{cr} = f(\varepsilon, t, T, \sigma)$), it is necessary to arrange the experimental data in a similar form. For this reason, creep rupture data is of no use when attempting to generate creep constitutive models. An example of the creep data presented for a single casting is shown in Table 3.1. Each casting has experimental data for a variety of temperature and stress combinations. The time to reach a set of pre-specified creep strains (0.5%, 1%, 2% and 5%) is then recorded for each of these combinations. Along with time to specific strains, data for instantaneous strain ε_0, time to tertiary creep t_{ter}, minimum creep strain rate $\dot{\varepsilon}_{min}$, and time to rupture t_r is also given. A schematic showing how each of these properties are determined is shown in Figure 3.2. It can be seen that all properties are as previously defined, with the time to tertiary creep determined by the intersection with the 0.2% minimum creep offset.

As was noted in the section on constitutive models for creep, the different creep regimes are modelled with different equations, with tertiary creep often not modelled in FEA packages. It is therefore necessary to determine which experimental data is in the tertiary creep regime, and omit these points from the experimental data which will be used to fit the models. From the data it can be seen that the time to 5% strain $t_{5\%}$ is

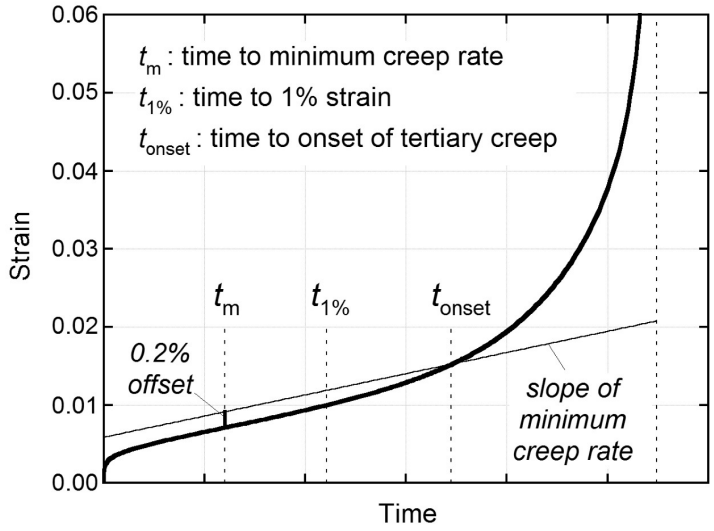

Figure 3.2: Schematic of creep curve showing how various properties are determined [45]

approximately equal to the time to fracture t_f for all cases. Additionally, there are data points for which the time to total strain is greater than the time to tertiary creep ($t_{\%} > t_{ter}$). With all of these data points omitted from the usable set, data points falling into either the primary or secondary creep regime are left. These are shown highlighted in Table 3.1.

Table 3.1: Extract for casting VbA from NIMS data sheet [46]. Primary and secondary creep data is shown with highlighted cells.

T (K)	σ (MPa)	ε_0 (%)	Time to total strain, $t_{\%}$ (hrs)				Time to tertiary creep, t_{ter} (hrs)	$\dot{\varepsilon}_{min}$ (%/hr)	Time to rupture, t_r (hrs)
			0.50%	1.00%	2.00%	5.00%			
723	412	0.257	5890	15600	19400	NA	15100	2.6E-05	19841.6
	373	0.238	24400	36500	40500	NA	30000	6.1E-06	40712.2
	333	0.199	46300	68900	80400	85300	53000	2.9E-06	85835.9
773	294	0.193	1400	2120	2680	3180	1580	1.1E-04	3373.0
	265	0.175	1870	2890	3870	4850	1780	5.9E-05	5283.2
	235	0.145	6700	28600	NA	NA	43800	2.1 E-05	44004.8
	196	0.114	6980	16700	33100	59100	37200	5.4 E-05	60844.8
823	235	0.150	106	201	324	457	168	2.2 E-03	524.0
	196	0.122	500	1720	4250	NA	5040	3.8 E-04	5425.0
	196	0.138	373	1510	NA	NA	NA	NA	NA

Note that the creep strain at zero time is exactly zero, and any instantaneous strain is due to the initial application of the load. The data supplied by NIMS does not make any distinction between the different strains in the specimen (e.g. elastic, plastic and

creep), and thus the reported strains are total strains ε_{tot}. Constitutive creep models normally do not include any contributions for this initial instantaneous creep, and model only creep strain. Therefore the total strains reported in the NIMS data have to be adjusted by instantaneous strains for each specific temperature and stress combination. An example of processed data is tabulated in Table 3.2 for casting VbA at 723 K, where ε_{cr} is the corrected creep strain. It can be seen that the data is now in the desired form of $\varepsilon_{cr} = f(t, T, \sigma)$.

Table 3.2: Pre-processed extract for casting VbA at 723 K

ε_{tot} (%)	ε_0 (%)	ε_{cr} (%)	t (hrs)	T (K)	σ (MPa)
0.50	0.257	0.243	5890	723	412
0.50	0.238	0.262	24400	723	373
0.50	0.199	0.301	46300	723	333

The preprocessed data shown in Table 3.2 is now in a form that represents the constitutive creep equations presented in Chapter 2. Note that for the remainder of this thesis there will be no differentiation between total strain ε_{tot}, and creep strain ε_{cr}. The creep strain will therefore be denoted by strain ε, unless otherwise stated. The following sections of this chapter will focus on model choice, and parameter determination for said model.

3.2 Model selection

ANSYS is the chosen FEA package for this research, and thus the creep model to be used is limited to the 13 models listed in Table 2.4. Figure 3.3 shows the NIMS experimental data for multiple castings at 823 K and 196 MPa. Looking at the data it is immediately clear that there is significant variation amongst the castings, a factor that will undoubtedly affect the confidence of the creep model prediction.

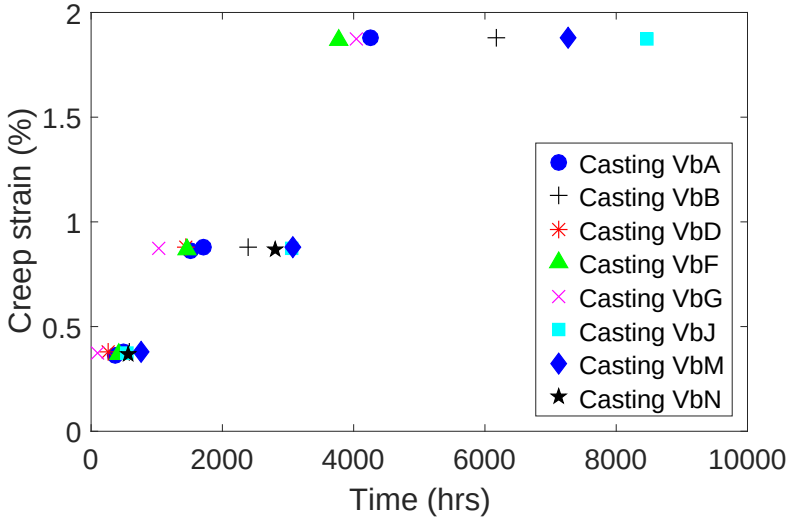

Figure 3.3: Scatter plot of NIMS experimental creep data for multiple castings at 823 K and 196 MPa

Ignoring the variation amongst castings, a creep model is still required. From the data it is evident that the model is not primary creep dominant, and thus the primary only creep models can be eliminated from the selection list. This leaves the option of a secondary creep model, or a model capable of modelling both primary and secondary creep. Figure 3.4 shows an initial fit of two models against the NIMS experimental data for a fixed temperature and stress. These models are the Norton secondary creep model and the combined time hardening (CTH) creep model, capable of representing both primary and secondary creep. From this initial fit it is clear that the amount of primary creep is **not** negligible, and hence a secondary creep model is perhaps not the correct model choice. The CTH model on the other hand has the added benefit of being able to capture this initial primary creep.

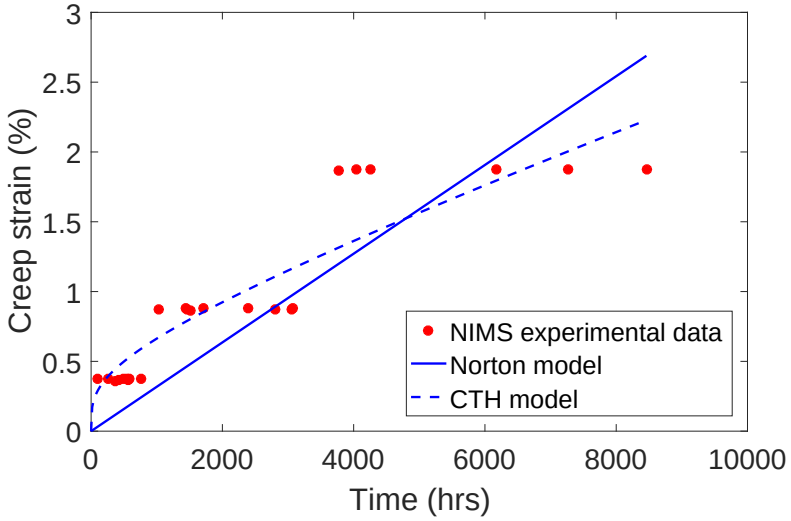

Figure 3.4: Initial estimate of model fits for all castings at fixed temperature $T = 823$ K and stress $\sigma = 196$ MPa

The CTH model is clearly the simplest of the two available primary and secondary models (Table 2.4), and is hence the chosen model for this data set. For fluidity the CTH model is repeated here, given by,

$$\varepsilon = \frac{x_1 \sigma^{x_2} t^{x_3+1} \exp\left(-\frac{x_4}{T}\right)}{x_3 + 1} + x_5 \sigma^{x_6} t \exp\left(-\frac{x_7}{T}\right). \tag{3.1}$$

Note that, for the fixed temperature and stress data shown above, the confidence in the CTH model prediction is limited by the data scatter. However, the CTH model is the only model, of the 13 available, that is capable of capturing the general form of the data and is therefore the obvious choice for this data set.

Before continuing, consider the units associated with the CTH model. Creep strain, a unitless parameter, is calculated from stress (MPa), time (sec) and temperature (K). Due to the large magnitude of these variables it is expected that the magnitude of the scaling factors x_1 and x_5 will be extremely small. Additionally, coefficients x_4 and x_7 are expected to be large, of magnitude order 10^4, due to their Arrhenius temperature association. In order to avoid convergence issues in the optimisation algorithm, the

CTH model of Equation 3.1 is scaled to ensure parameters of similar order of magnitude are obtained. This scaled CTH model is given by,

$$\varepsilon = \frac{\chi_1 \sigma^{\chi_2} t^{\chi_3+1} \exp\left(-\frac{\chi_4}{T}\right)}{\chi_3 + 1} + \chi_5 \sigma^{\chi_6} t \exp\left(-\frac{\chi_7}{T}\right), \tag{3.2}$$

where χ_1, χ_2, ..., χ_7 are the scaled parameters. These are scaled such that $x_1 = 10^{\chi_1}$, $x_2 = \chi_2$, $x_3 = \chi_3$, $x_4 = 10^4\chi_4$, $x_5 = 10^{\chi_5}$, $x_6 = \chi_6$ and $x_7 = 10^4\chi_7$.

Consider the results from Figure 3.4 which shows a fit for a fixed temperature and stress ($\varepsilon = f(t)$). This type of model is discouraged for two reasons:

1. The large scatter in the data leads to little confidence in predictions.
2. The form of the model ($\varepsilon = f(t)$) makes modelling for arbitrary temperatures and stresses inaccurate.

A possible alternative is to fit each casting separately, allowing for optimal results for each specific casting. By utilising this approach the engineer is no longer assuming each casting is the same material, but rather treating each casting as a separate material, which is more accurate due to the variations in microstructes. This approach then allows for the temperature and stress dimensionality to be added into the optimisation problem, making modelling for arbitrary conditions more accurate. A "family" of creep models can then be used as input to Finite Element (FE) simulations, and the resulting variation analysed to identify worst case scenarios.

3.3 Problem formulation

By modelling each casting separately and including the temperature and stress dimensions in the optimisation problem, the scaled CTH model in Equation 3.2 models strain as a function of time, temperature and stress ($\varepsilon = f(t, T, \sigma)$). The coefficients for this model can be solved for by modelling the LSE in a minimisation problem given by,

$$f = \sum_{i=1}^{n} \left(\frac{10^{\chi_1} \sigma_i^{\chi_2} t_i^{\chi_3+1} \exp\left(-\frac{10^4\chi_4}{T_i}\right)}{\chi_3 + 1} + 10^{\chi_5} \sigma_i^{\chi_6} t_i \exp\left(-\frac{10^4\chi_7}{T_i}\right) - \frac{\varepsilon_{data,i}}{100} \right)^2, \tag{3.3}$$

where n is the number of experimental data points available, and $\varepsilon_{data,i}$ is the i-th experimental data point. The LSE error cost function f is then minimised through the use of a multi-start unconstrained optimisation algorithm.

Due to the non-linear nature of the cost function, a downhill simplex method was used in the optimisation algorithm. The downhill simplex method, also called the Nelder-Mead method, requires only function evaluations and no derivatives [47]. Figure 3.5 demonstrates the procedure associated with the simplex method. The method works by constructing a simplex, which is a geometrical figure in N dimensions, consisting of $N+1$ points (or vertices). In two dimensions this results in a simplex which is a triangle,

and so on. The method calculates the function value at each of the simplex points to determine the maximum function value. Convergence to at least a local minimum is achieved by taking a series of steps, called reflections, that move the point with the largest function value through the opposite face of the simplex. When the method reaches a local minimum it contracts itself in all directions until it converges to a result within the user defined convergence criterion.

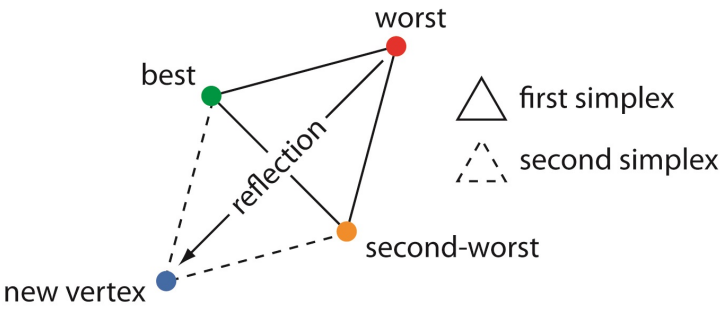

Figure 3.5: Schematic of downhill simplex method [48]

Due to the fact that the downhill simplex method easily converges to local minima, the problem is termed illposed. In order to try and locate a global minimum, a multi-start process is utilised in which multiple random starting points are used and the best solution saved.

From the NIMS experimental data in Figure 3.3 it can be seen that although the amount of primary creep is not negligible, the time associated with primary creep is. This means that majority of the experimental data is associated with the secondary creep regime. Looking at the CTH model it can be seen that four coefficients are associated with primary creep, where little data is available, and three associated with secondary creep, where majority of the data lies. Therefore, in order to limit the uncertainty associated with the coefficients that are solved, a three step process is adopted. This three step process is summarised by:

1. Make an initial guess of the secondary creep coefficients based on available data.
2. Formulate the LSE cost function for a simplified CTH model in which the secondary creep coefficients (χ_5, χ_6 and χ_7) are solved for.
3. Formulate the LSE cost function for the full original CTH model in which all coefficients are solved for with a bias to the solution obtained in step 2.

This three step process is discussed in more detail in the following three subsections.

3.3.1 Initial guess

Optimisation algorithms usually require an initial guess of the coefficients to be made. The closer this initial guess is to the solution, the faster convergence will occur. Due to the fact that few of the coefficients have known values, it is very difficult to determine adequate orders of magnitude for the initial guess. Coefficients χ_4 and χ_7 are expected to be large due to the Arrhenius temperature association, setting them close to the order

of unity (recall the 10^4 scaling). An initial guess for χ_6, the secondary stress exponent, can be obtained by considering the simple Power law creep model ($\dot{\varepsilon}_{min} = A\sigma^n$). By using the available minimum strain rate data it is possible to get an approximation for χ_6 by determining the gradient of the $\log(\sigma) - \log(\dot{\varepsilon}_{min})$ experimental data. The results from this analysis are shown in Figure 3.6 for casting VbB. It can be seen that the stress exponent χ_6 is approximately of order magnitude 10.

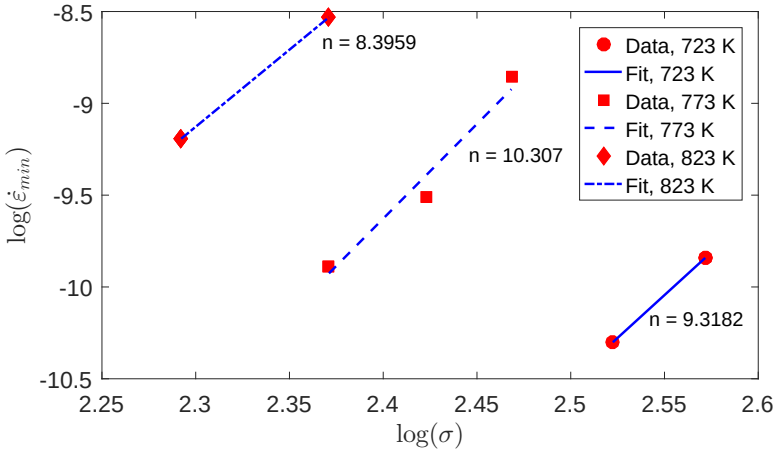

Figure 3.6: Casting VbB curve fit results for power law creep model

The uncertainty associated with the remaining coefficients meant that a trial and error procedure needed to be followed. It was determined that numbers of magnitude order 10 for these remaining coefficients resulted in the best results. Using these random numbers in conjunction with the initial guesses for χ_4, χ_6 and χ_7 it was possible to generate a complete set of random starting points with the correct order of magnitude. In order to avoid the solution converging to the same local minimum with each restart the initial guess was randomised for each restart. However the magnitude order for the initial guess remained the same.

3.3.2 Simplified CTH model

The use of a simplified CTH model can be utilised to first determine the secondary model coefficients for the full CTH model. From the experimental data it appears that the data is analogous to a straight line with a y-intercept greater than zero. By omitting the time exponent from the CTH model of Equation 3.1 it is possible to obtain a secondary model which incorporates a constant primary creep offset. This therefore models an instantaneous primary creep, with a constant secondary creep. This simplified model is given by,

$$\varepsilon = 10^{\chi_1}\sigma^{\chi_2}\exp\left(-\frac{10^4\chi_4}{T}\right) + 10^{\chi_5}\sigma^{\chi_6}t\exp\left(-\frac{10^4\chi_7}{T}\right), \tag{3.4}$$

where the exponential time coefficient χ_3 is omitted, with the primary term now solely representing the magnitude of primary creep. This is analogous to a straight line with a y-intercept, as shown in Figure 3.7a. This model can be used in a LSE formulation

similar to Equation 3.3 and solved for to obtain a good estimate of the secondary creep coefficients χ_5, χ_6 and χ_7. A summary of the two step process is given in Figure 3.7, where it is seen that the simplified CTH model provides a reliable estimate for the full CTH model.

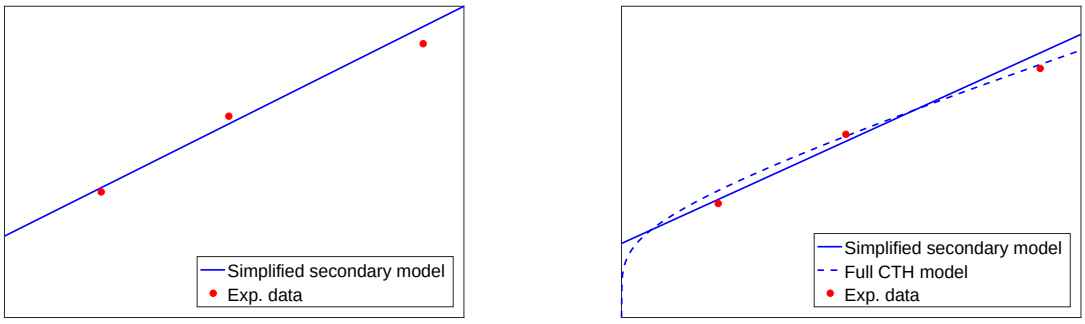

(a) (b)

Figure 3.7: Multi-step optimisation process showing (a) use of simplified CTH to determine secondary coefficients, and (b) use of full CTH model to obtain better fit

3.3.3 Full CTH model

The multi-start unconstrained simplex optimisation strategy is applied to the simplified CTH, a good estimate of the secondary creep model coefficients are obtained. By biasing the coefficient results of the full CTH model to these results it is possible to optimise the full CTH model coefficients, and obtain a model capable of modelling both primary and secondary creep. In order to do this the use of regularisation is considered, where an extra term is added to the initial least squares residual objective function which penalises deviations of the coefficients from a chosen solution. The penalty term P is given by,

$$P = \boldsymbol{w}\left(\frac{\boldsymbol{x}}{\boldsymbol{x^*}} - 1\right)^2, \tag{3.5}$$

where P is written in terms of the weighting vector $\boldsymbol{w}$, the preferred solution $\boldsymbol{x}^*$, and the current solution $\boldsymbol{x}$. The preferred solution here refers to the solution obtained from optimisation of the simplified CTH model. This means that any deviations away from the coefficients determined from this simplified model are penalised, biasing the result to the coefficients previously determined.

Adding the penalty function from Equation 3.5 to Equation 3.3, a new objective function is formulated which will allow one to solve the full CTH model coefficients, but with a solution biased to that obtained from solving the simplified model of Equation 3.4. This new objective function f is given by,

$$f = \sum_{i=1}^{n} \left(\frac{10^{\chi_1} \sigma_i^{\chi_2} t_i^{\chi_3+1} \exp\left(-\frac{10^4 \chi_4}{T_i}\right)}{\chi_3 + 1} + 10^{\chi_5} \sigma_i^{\chi_6} t_i \exp\left(-\frac{10^4 \chi_7}{T_i}\right) - \frac{\varepsilon_{data,i}}{100} \right)^2 + \boldsymbol{w} \left(\frac{\boldsymbol{x}}{\boldsymbol{x^*}} - 1 \right)^2. \tag{3.6}$$

Again one must implement multi-start technique to try and converge to a global minimum.

Although minimisation of the above objective function is unconstrained, one can choose to constrain the sign of specific coefficients with the use of absolute values. This is in order to force the coefficient solutions to be physically possible. For example, it is known that the stress sensitivity exponents are required to be positive. Additionally, in order for the creep model to predict an expected creep curve the coefficients χ_1, χ_3 and χ_5 are required to be negative, with all other coefficients positive. With this in mind, the objective function of Equation 3.6 is therefore modified to obtain,

$$f = \sum_{i=1}^{n} \left(\frac{10^{-|\chi_1|} \sigma_i^{|\chi_2|} t_i^{-|\chi_3|+1} \exp\left(-\frac{10^4 |\chi_4|}{T_i}\right)}{-|\chi_3| + 1} + 10^{-|\chi_5|} \sigma_i^{|\chi_6|} t_i \exp\left(-\frac{10^4 |\chi_7|}{T_i}\right) - \frac{\varepsilon_{data,i}}{100} \right)^2 + \boldsymbol{w} \left(\frac{\boldsymbol{x}}{\boldsymbol{x^*}} - 1 \right)^2, \tag{3.7}$$

which constrains the signs of the coefficients.

3.4 Preliminary results

The results of the best converged coefficients for the simplified combined time hardening model are tabulated in Table 3.3. The best solution was determined from that with the lowest mean percentage error, $\bar{E}$, between the model and experimental data. Due to the fact that the model is primarily based on a secondary model, one would like to focus on the converged secondary constants, namely χ_5, χ_6 and χ_7. It is interesting to note that there is a large variation in the secondary stress sensitivity exponent χ_6, which strongly controls the gradient of the secondary component of the curve. This again shows the large variation amongst the castings.

Considering the results reported in Table 3.3 it is clear that the results for casting VbA and VbF are significantly different to the others. Upon inspection of the experimental data for these castings it is seen that these castings do not show the same stress relationship as the other castings. This is shown in Figure 3.8 where the experimental data appears to be insensitive to stress variations. This could be due to differences in testing conditions or the microstructure of the castings. The CTH model is incapable of modelling this small sensitivity to stress, and therefore these castings have to be omitted from the data set. Similar results are seen for casting VbH. It can therefore

Table 3.3: Converged coefficient results for simplified CTH model (Equation 3.4)

Casting	$\bar{E}$	χ_1	χ_2	χ_4	χ_5	χ_6	χ_7
VbA	0.1729	5.03	2.39	0.7066	0.01	1.54	2.3713
VbB	0.1126	0.11	1.40	1.0992	7.60	8.84	4.1356
VbD	0.1492	4.94	2.40	0.6629	6.96	8.64	4.1193
VbF	0.1787	5.35	2.33	0.5940	0.27	0.98	2.1041
VbG	0.1106	3.00	2.61	1.0816	7.52	10.27	4.7293
VbH	0.0667	1.55	1.54	0.8357	8.41	7.59	3.7090
VbJ	0.0695	5.20	2.42	0.6722	7.60	9.82	4.5720
VbM	0.1105	4.99	2.51	0.6627	8.46	12.26	5.4548
VbN	0.1322	5.00	2.46	0.6459	8.77	11.23	4.9545

be concluded that the CTH model is incapable of modelling the response for castings VbA, VbF and VbH, and they can therefore be removed from the experimental data set for all future analysis.

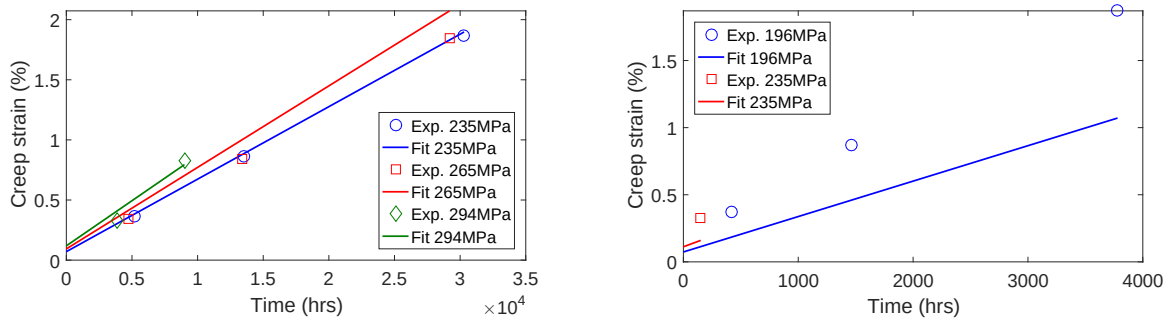

(a) (b)

Figure 3.8: Simplified CTH model results for casting VbF creep strain results which appear to be insensitive to stress at (a) 773 K and (b) 823 K

Figure 3.9 shows the results for castings which yielded sensible coefficient solutions. The graphs depict the NIMS data as experimental data points, as well as the model approximations at the given stress and temperature. It can be seen that a good approximation to the data is achieved, with an offset accounting for the amount of primary creep.

From the results it is possible to choose a set of model coefficients $\boldsymbol{x}^*$ that represent a preferred solution, where the preferred solution refers to a solution that the user feels is a good representation of the global minimum. This preferred solution is chosen to give an average representation of the simplified CTH model results, and is used to bias the results of the full CTH model. This means that the user is "driving" the solution close to the preferred solution, and thus avoiding other minimums that are not a good representation of the active creep deformation mechanisms. There is no exact science to this process and the results are based mainly on trial and error, and experimentation with various combinations of coefficients. With this in mind the preferred solution $\boldsymbol{x}^*$ and weighting vector $\boldsymbol{w}$ are tabulated in Table 3.4, where the values were chosen to

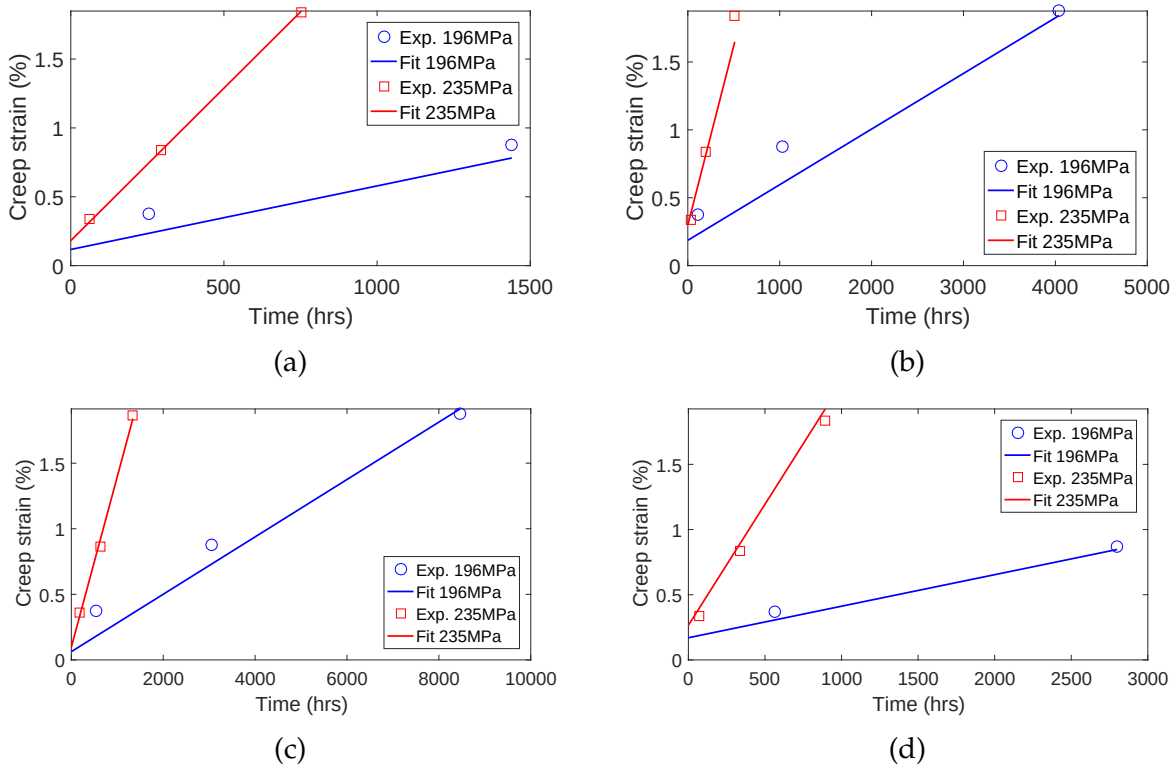

Figure 3.9: Simplified CTH model results for (a) casting VbD at 823 K, (b) casting VbG at 823 K, (c) casting VbJ at 823 K and (d) casting VbN at 823 K

give the best seen average representation of the results from Table 3.3. Note that no weighting is applied to coefficient χ_3 due to the fact that no information is available for it. Coefficients χ_1 and χ_5 were set based on user preference as these are simply constant multiples in the equations.

Table 3.4: Preferred solution and weighting vector for penalty function

	χ_1	χ_2	χ_3	χ_4	χ_5	χ_6	χ_7
$\boldsymbol{x}^*$	6	2	-0.9	0.85	8	10	4.50
$\boldsymbol{w}$	1	1	0	1	1	1	1

Optimising the full combined time hardening model results in the coefficients tabulated in Table 3.5. Notice that casting VbA, VbF and VbH has been excluded in these results. The average error over the range of castings is approximately 0.15% in the creep strain, which instils confidence in the results.

The results for castings VbB and VbD are shown in Figure 3.10 and Figure 3.11 respectively. It can be seen from the results in Tables 3.3 and 3.5 that the gradient for the secondary creep stage (χ_6) remains relatively constant for both the simplified and full model. This is due to the regularisation that was used to penalise deviations away from the preferred solution. Note however that the full CTH model captures the primary creep response of the material. This is highlighted in Figure 3.10 for casting VbB.

Table 3.5: Converged coefficient results for full CTH model (Equation 3.2)

Casting	$\bar{E}$	χ_1	χ_2	χ_3	χ_4	χ_5	χ_6	χ_7
VbB	0.1039	2.38	1.76	-0.882	1.1345	7.25	8.42	4.0234
VbD	0.1330	4.47	1.45	-0.935	0.5805	5.60	8.07	4.1285
VbG	0.3137	2.81	1.54	-0.932	0.9154	6.34	9.97	4.8262
VbJ	0.0646	5.34	2.15	-0.905	0.7950	7.57	9.92	4.6272
VbM	0.1223	0.05	1.32	-0.910	1.3416	9.95	13.21	5.6011
VbN	0.2653	3.43	1.67	-0.814	0.9177	11.92	12.99	5.1573

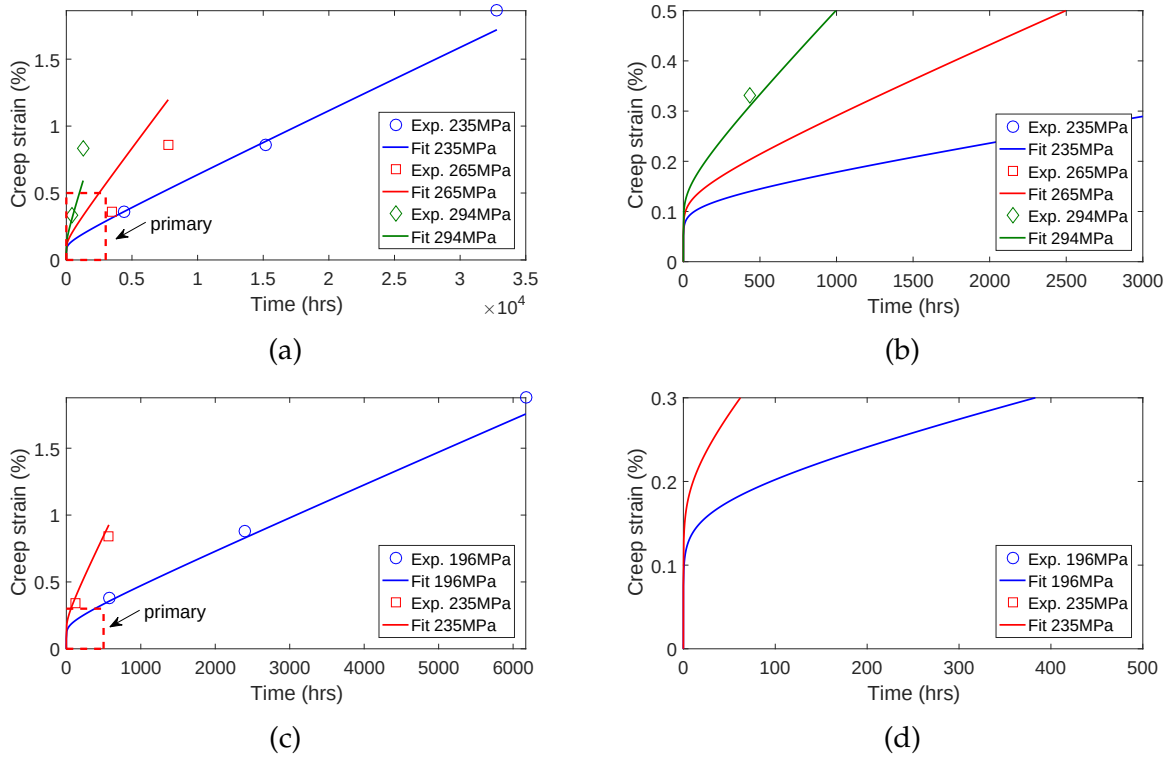

Figure 3.10: CTH model results for casting VbB at (a) 773 K, (b) zoomed primary creep area at 773 K, (c) 823 K, and (d) zoomed primary creep area at 823 K

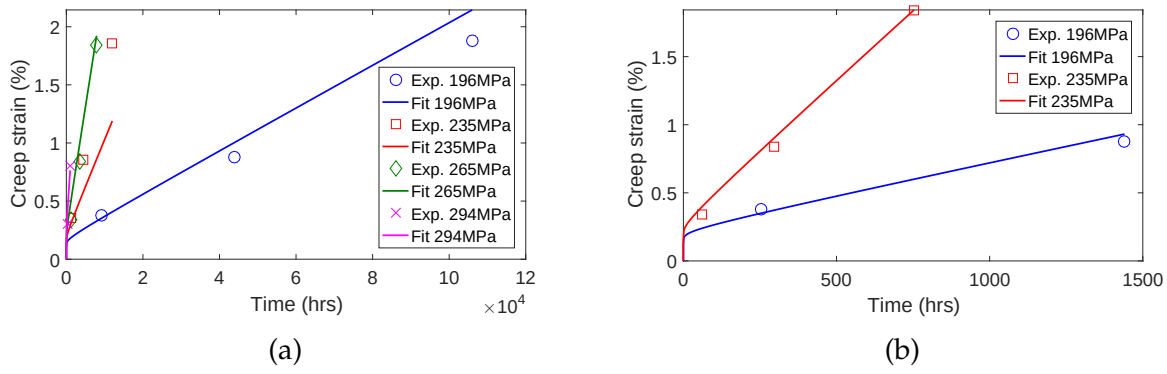

Figure 3.11: CTH model results for casting VbD at (a) 773 K and (b) 823 K

A more complete set of results for all castings is reported in Appendix B, where the results for both simplified and full CTH models are documented for the entire temperature range. A point worth highlighting at this point is that the creep models shown thus far are multidimensional. This means that only one model is used for each casting to capture the entire temperature and stress range. These multidimensional models are useful in that they can be used to model for arbitrary temperature and stress combinations. This multidimensionality is better seen when looking at the models on a log time scale. The results for casting VbD at 773 K are presented on a log time scale in Figure 3.12 where the stress multidimensionality is made more clear. Note that the same model captures a variety of stresses accurately. In a similar manner the model captures the data over the entire temperature range. The model is therefore a four dimensional model of creep strain, time, temperature and stress.

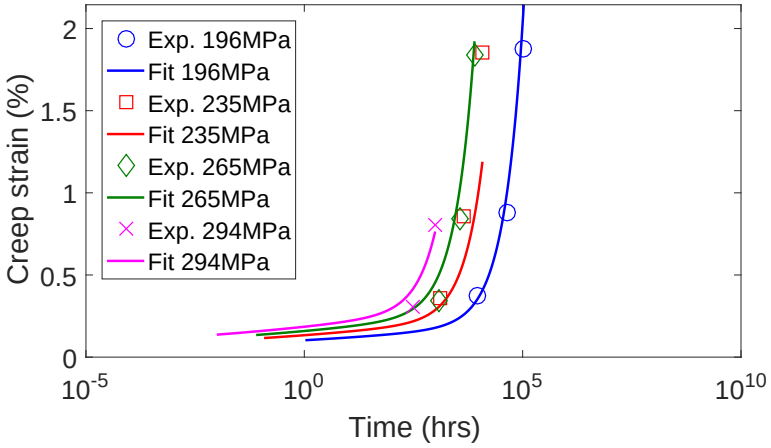

Figure 3.12: CTH model approximation for casting VbD at 773 K and multiple stresses

Lastly, consider Figure 3.13 which shows all of the creep models along with the entire NIMS creep dataset. It can be seen that by utilising all of the models it is possible to capture the entirety of the data set. The benefit of this approach is that no two models in the family of creep models are parallel to each other. This means that a variety of primary creep transients and secondary creep rates are modelled.

3.5 Stochastic analysis

Thus far it has been shown that by fitting each casting separately it is possible to generate a family of creep curves that captures the entire data set. In order to obtain a more complete view of the data set, a stochastic approach is proposed where random creep models are generated. In order to generate these random models it was proposed that additional data should be generated. New random models can then be determined from this new additional data. It is however required that this data have the same form as the available experimental data, meaning the original and additional random data sets should have similar distributions.

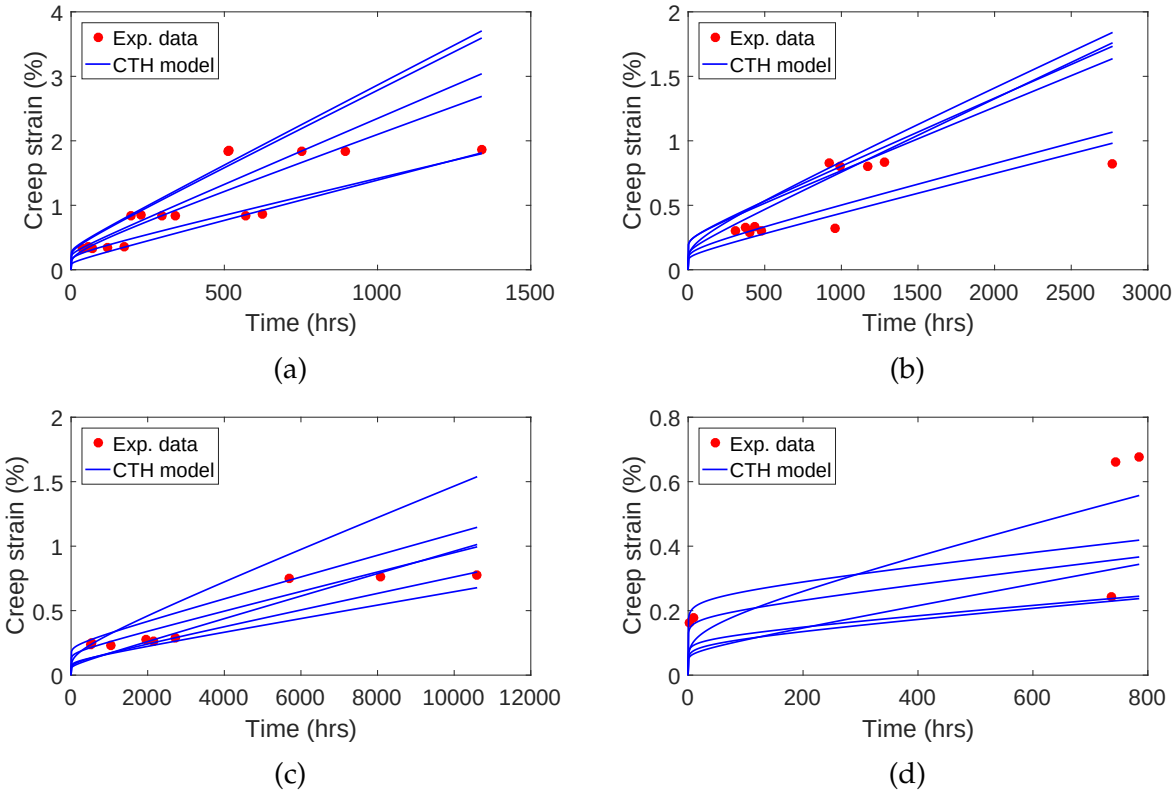

Figure 3.13: Family of creep models for all castings at (a) 823 K and 235 MPa, (b) 773 K and 294 MPa, (c) 723 K and 373 MPa, and (d) 723 K and 412 MPa,

This methodology requires one to fit a multimodal PDF to the experimental data, and sample random data from this distribution. Random creep models can then be determined by applying the above mentioned optimisation algorithm to the new random data. This PDF is given by the multimodal Gaussian distribution in Equation 3.8 [49],

$$p(x) = \frac{1}{N}\Sigma_{n=1}^{N}\frac{1}{(2\pi h^2)^{1/2}}\exp\left\{-\frac{||x-x_n||^2}{2h^2}\right\}, \tag{3.8}$$

where N is the total number of data points and h is the standard deviation of the points being fitted. One can then use the cumulative probability distribution to sample a set of new data for use in the existing optimisation algorithms. Note that in this process each dataset is broken up into its representative 0.5%, 1% and 2% creep strain subsets from which the PDF of each of the subsets is determined from Equation 3.8 separately. A summary of this methodology is explained in the flow diagram in Figure 3.14. It can be seen that new random data has been generated that has the same form as the original data, better resembling experimental data that would commonly be available. Note that the flow diagram shows the process for a single subset of the data, with the creep strain not explicitly shown. The random data set is then generated by sampling from each PDF separately. The steps associated with this are summarised by:

1. Fit a multimodal PDF to the experimental data. Note that the data is normalised with respect to time.

2. Calculate the cumulative probability distribution of the PDF.

3. Random numbers between 0 and 1 are generated, and the corresponding normalised time determined from these points.

4. Use sampled data as random data resembling the PDF of the original data.

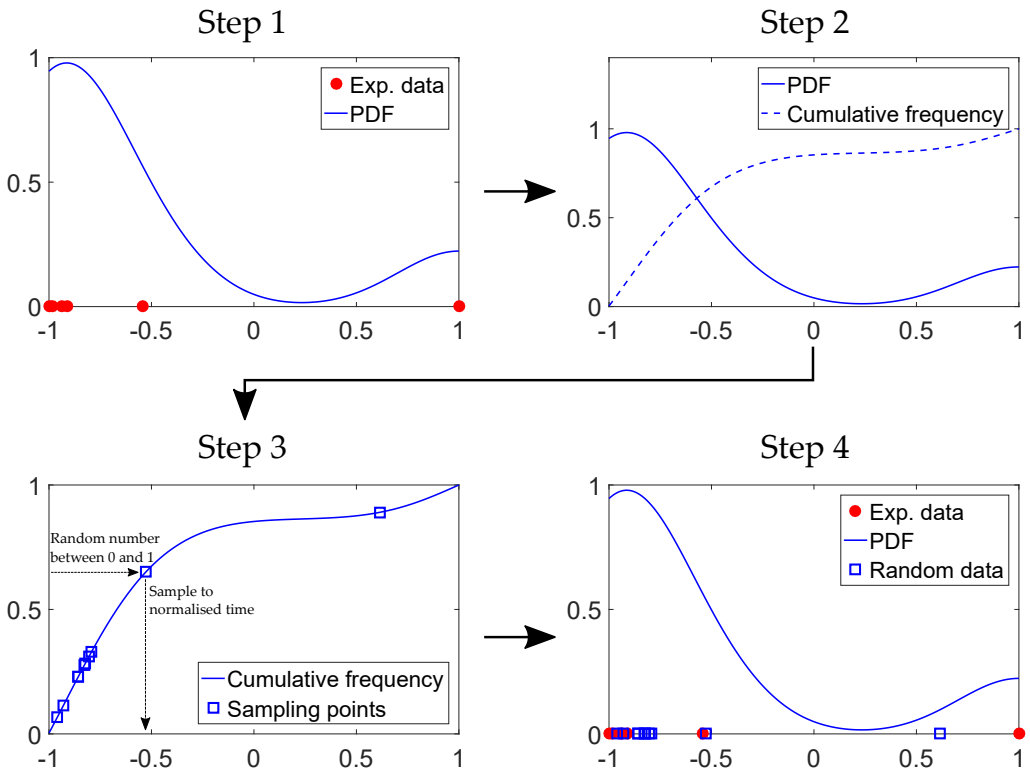

Figure 3.14: Flow diagram of multimodal PDF sampling methodology. Step 1: Fit PDF, Step 2: Cumulative frequency, Step 3: Sample from cumulative frequency, and Step 4: Sampled data used as additional random data.

Using this method an additional five creep models were generated using the optimisation methodology previously described. A complete set of results, including both the original casting models and random models, is shown in Figure 3.15. It can be seen that a more complete representation of the data is now achieved, where the data refers only to the original creep data and not the randomly generated data. The benefit of using the stochastic methodology outlined in this section is that the random models generated are not necessarily constrained to the upper and lower bounds of the original models. Instead, they add additional variation to the total model set, each representing different transients and minimum creep gradients. A "fuller" view of the data region is therefore achieved.

The converged coefficient results for these five random models are summarised in Table 3.6. It can be seen that these coefficients show resemblance to the original coefficients obtained, meaning that similar deformation mechanisms are represented with the random models.

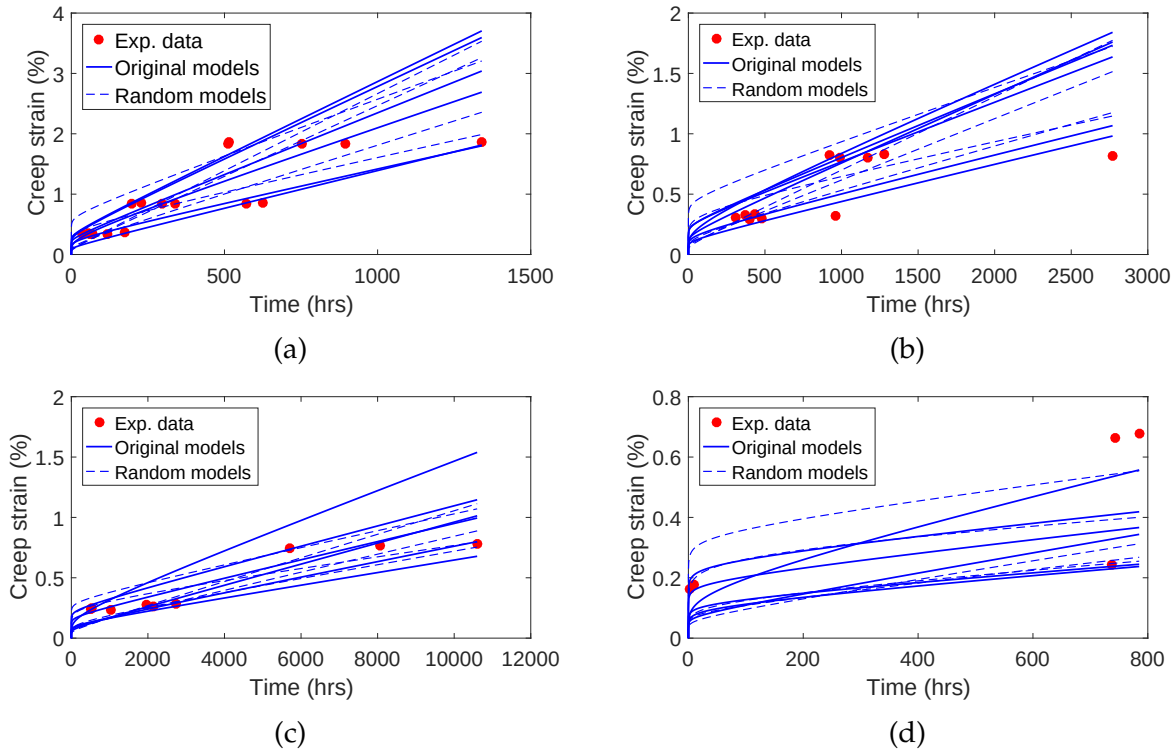

Figure 3.15: Complete set of creep models for all castings at (a) 823 K and 235 MPa, (b) 773 K and 294 MPa, (c) 723 K and 373 MPa, and (d) 723 K and 412 MPa,

Table 3.6: Converged random data coefficient results for full CTH model (Equation 3.2)

Description	χ_1	χ_2	χ_3	χ_4	χ_5	χ_6	χ_7
Set 1	4.92	1.98	-0.901	0.8105	6.84	10.34	4.9018
Set 2	3.65	2.11	-0.891	1.0050	7.13	9.44	4.5061
Set 3	4.41	1.80	-0.889	0.8401	8.15	11.16	5.0148
Set 4	2.96	2.14	-0.942	1.1099	8.99	12.01	5.2647
Set 5	4.11	1.67	-0.850	0.8101	6.07	9.06	4.5049

3.6 Discussion of results

Looking at the experimental data and creep model results it is clear that, due to the spread in experimental data, it is not feasible to use a single model through the data. Rather, a family of creep models should be used to capture the entirety of the data set. The single fit models, as shown in Figure 3.4, utilised a creep model that was only a function of time t. Using the multiple model approach and fitting each casting separately allowed for the temperature T and stress σ dimensions to be added into the model, making for a more robust model.

Lastly, consider Figure 3.16 which shows the 95% confidence intervals for casting VbJ at 823 K and 235 MPa. It can be seen that there is high confidence during the secondary creep regime where more experimental data is available. However, during the initial stages (primary creep) the confidence bands widen, representing the decrease in confidence during this time. This is due to the fact that little to no data is available at the

small times associated with primary creep. These wide confidence bands indicate that caution should be used when making model predictions in these regions, and are by no means a representation of the actual creep model which is expected. Note the use of the log time scale once again, to aid in clarity of the results.

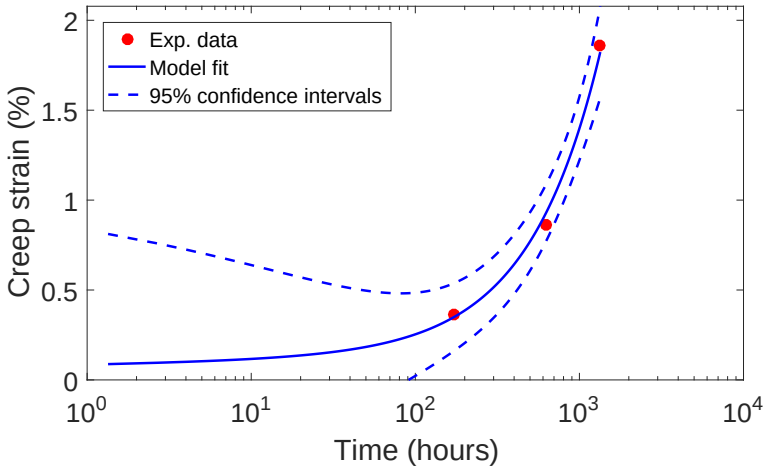

Figure 3.16: 95% Confidence band for casting VbJ at 823 K and 235MPa

3.7 Concluding remarks

This chapter has shown that, by using a simple unconstrained optimisation algorithm, the openly available NIMS creep data can be used to fit creep material models that can be implemented into ANSYS.

It was shown that a simple secondary creep model is not capable of capturing an almost instantaneous primary creep. The CTH model implemented has separate terms for both primary and secondary creep, which allows the model to capture this initial instantaneous primary creep, as well as the change in deformation mechanisms between creep regime changes.

Finally, and possibly the most significant output of the chapter, it was shown that by using a multiple model approach the entirety of the data set can be more accurately captured. By implementing this approach the creep models are able to capture the inherent natural variation of material properties through large components. Additionally, a stochastic approach was followed to generate random creep models, giving a more rounded fit to the data.

Chapter 4

Initial FE modelling and elastic analysis

Complicated time-dependent models can take anywhere from a few hours to a few days to solve. As a result, checking model accuracy and convergence criterion with a full time-dependent model is very inefficient and can take several weeks or more to complete. The elastic model can often be used as a tool to quickly asses the affect that changes in the model will have on the desired outputs before running a full time-dependent analysis. In this case the elastic model refers to the time-independent model in which loads and boundary conditions are applied statically. A full elastic model analysis is thus required before full time-dependent creep models are run. This chapter highlights the elastic model analysis that was conducted to ensure accurate and efficient use of the full time-dependent model.

4.1 Modelling geometry

Before one can begin to set up a FE model, an accurate geometry model is required. Depending on the type of analysis, it is up to the engineers discretion as to how accurate the model needs to be. Modelling of all small entities such as fillets, O-Ring grooves and bolt holes leads to an increase in mesh density due to all the small geometric elements that need to be captured. In circumstances where these small entities do not have an affect on the structural integrity around the area of concern they can be removed in order to achieve a better mesh count.

Due to the complex nature of IP valve operations, it is to be expected that the valve casing will have many small geometric entities to account for correct seating and lubrication of components, as well as firm and solid fixing of mounts to connecting entities. In order to simplify the model and decrease solving time these small entities were ignored. This meant that all small radii, seating/sealing steps and bolt holes were omitted from the simplified geometry, with the exception of those close to the high stress areas at the inlet and outlet flanges. A comprehensive study was conducted to ensure that the results obtained from the simplified geometry did not differ significantly from those of the original body.

Due to copyright issues, a complete drawing of the IP valve to be modelled cannot be included. However, a dimensionless cross section of the part showing all major component details is shown in Figure 4.1.

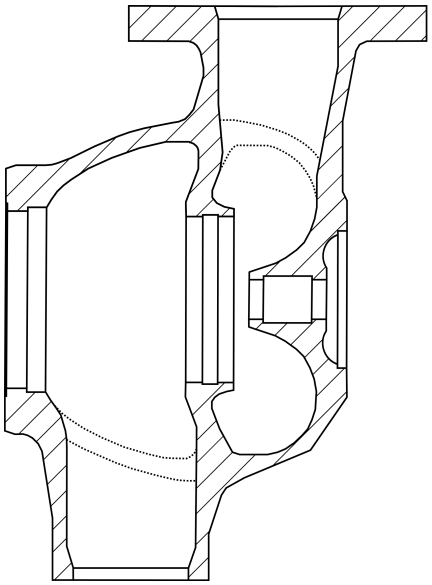

Figure 4.1: Sketch of IP valve

4.2 Problem definition

4.2.1 Component operating conditions

Close representation of the operating conditions are required in order to generate accurate results. Before further discussing the operating conditions of the component, consider a representation of the hydraulic component assembly shown in Figure 4.2. The hydraulics move along a centre shaft (not shown in the figure) and are held in place by the control side assembly (left) and axially located by a hydraulic cap (right). Also shown is the high stress area noted from a previous confidential study conducted by the OEM.

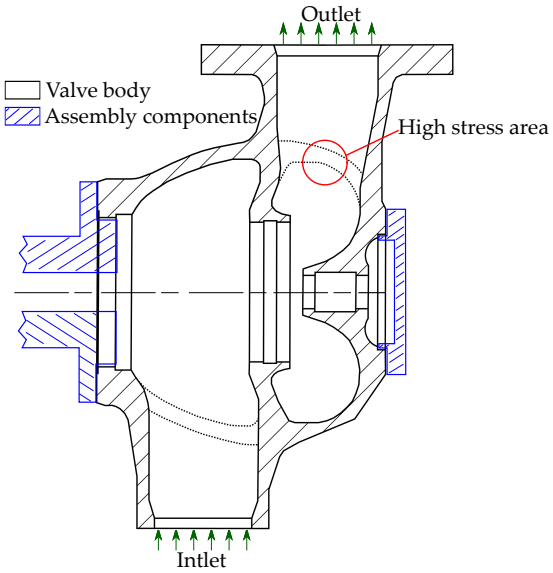

Figure 4.2: Representation of IP valve assembly

During steady state operating conditions the valve operates completely open with negligible pressure or temperature drop from inlet to outlet. Due to the high operating temperatures the entire valve body is insulated with fibreglass blankets to ensure minimal heat loss to the environment. For this reason it is assumed that there is zero temperature differential through the body material. The pressure P and temperature T are therefore assumed constant throughout the whole body at steady state operating conditions of $P = 3.2$ MPa and $T = 510$ ° C respectively.

On plant the valve is connected via a welded pipe to the inlet steam, and bolted via a flange connection at the outlet. These connections are designed such that during steady state operating conditions there are negligible reaction forces at these connections. The hydraulic control side is located left of the body (as depicted in the assembly sketch), with a hydraulic cap on the right side of the body, locating the shaft axially. Furthermore, the valve body is supported by the turbine floor, but is allowed to move laterally along the floor to accommodate expansion and contraction of other components on the turbine floor.

4.2.2 Material properties

The FE equations that are solved require accurate material properties if realistic results are to be obtained from the analysis. Due to the high operating temperatures, the IP valve is cast from the creep resistant 1Cr-1Mo-0.25V alloy steel. The temperature dependent material properties are tabulated in Table 4.1, where RT refers to room temperature of 20°C and CTE refers to the coefficient of thermal expansion. Steel is incompressible and thus has constant density over the temperature range of interest. Additionally, the change in Poisson ration has been assumed negligible over the temperature range.

Table 4.1: Temperature dependent material properties for 1Cr-1Mo-0.25V alloy steel

			Temperature °C						
	Symbol	Unit	RT	100	200	300	400	500	550
Density	ρ	kg/m^3	7840						
Young's modulus	E	GPa	206	205	201	193	181	164	155
Poisson's ratio	ν	-	0.3						
CTE	α	$10^{-6}/K$	-	12.2	12.9	13.4	13.9	14.3	14.5

4.2.3 FE model boundary conditions

First consider the support boundary conditions at the inlet and outlet of the valve. Frictionless roller supports were applied at these locations to simulate the removal of material. Additionally, frictionless roller supports were applied on the left side of the valve where the hydraulic controls would be located. These roller supports could be replaced with a mean pressure derived from closed cap conditions. Both scenarios are equally correct, with the choice of roller supports based solely on user preference. These three boundary conditions are depicted in Figure 4.3.

With respect to the loading conditions, it was mentioned above that the valve operates at a constant pressure and temperature of 3.2MPa and 510°C respectively. The internal pressure was applied to all internal faces as shown in Figure 4.3. Note the location of the seal preventing the pressure boundary condition acting past its' location. Due to the constant temperature throughout the entire body, the thermal boundary condition of 510°C was applied to every node in the system.

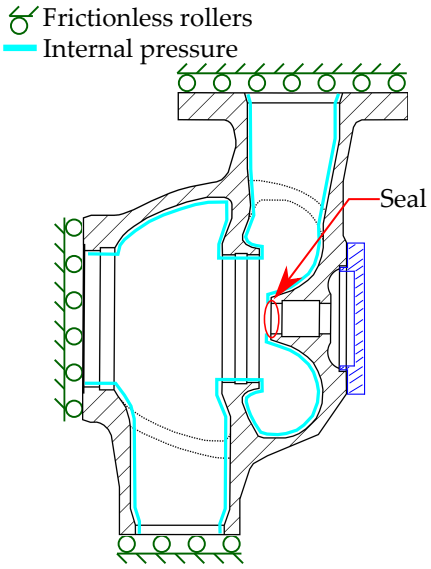

Figure 4.3: Schematic of pressure and frictionless support boundary conditions

Finally, consider the hydraulic cap located on the right of the body. It is clear that removing this cap without applying the correct boundary conditions will affect the high stress area noted from Figure 4.1. For this reason it is required to model the hydraulic cap in the assembly using contact between the cap and valve body. Consider the bolt layout in Figure 4.4a which shows the layout of bolts that connect the hydraulic cap to the valve body. Bolted connections are known to exert a pressure along a pressure cone rather than directly along its area of contact [50]. This so called pressure zone is depicted in Figure 4.4b.

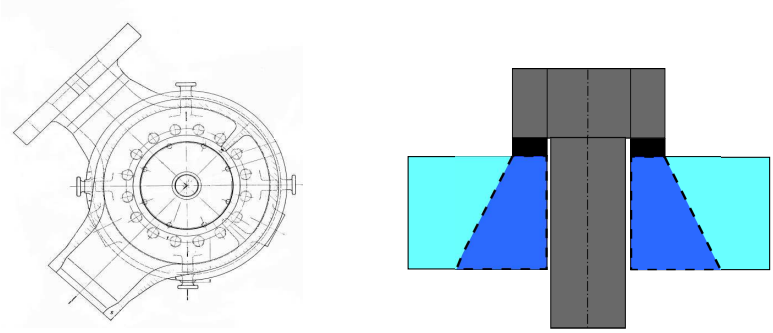

(a) Bolt layout (b) Pressure cone

Figure 4.4: Schematics showing (a) Bolt layout for hydraulic cap attachment and (b) Pressure cone caused by bolt fasteners (adapted from [50])

The hydraulic cap adds significant stiffness to the valve assembly, and hence a combination of bonded, frictionless and frictional contact is required to accurately model the contact between the valve body and said cap. By considering the pressure cone from Figure 4.4b, it can be assumed that the effective bolt area extends through the entire tangential area of the bolts. This connection is modelled using a bonded contact between the two bodies. The areas directly above and below the bolts are then modelled with frictionless contact. The remaining area of contact between the cap and body is modelled with a frictional contact. The coefficient of static friction $\mu_s = 0.5$ is assumed from the static coefficient of friction between two steel bodies. A summary of the contact conditions are shown in Figure 4.5. The ANSYS implementation of these three contact regions is shown in Figure 4.6.

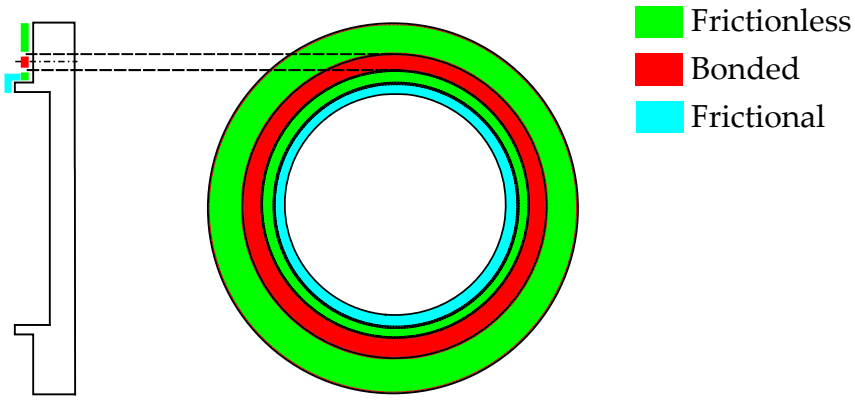

Figure 4.5: Schematic of contact between hydraulic cap and valve body

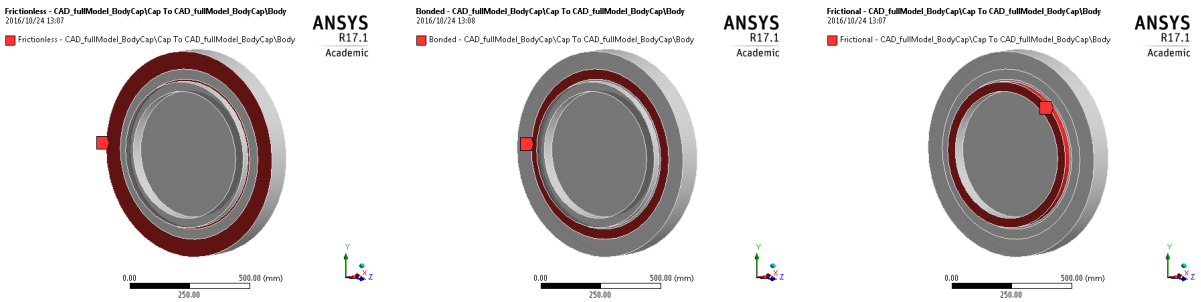

(a) (b) (c)

Figure 4.6: Hydraulic cap contact regions for (a) Frictionless contact, (b) Bonded contact, and (c) Frictional contact

4.2.4 Mesh convergence

By representing a body volume by a set of discrete elements one is inherently introducing errors into the model. For this reason mesh convergence is an essential part of any FEA project. Mesh convergence refers to the process of iteratively increasing the mesh density and determining resulting effect on the required outputs. As one would expect, larger mesh densities result in longer solving times due to the increased number of equations that need to be solved. The aim of a mesh convergence study is to

obtain a mesh density that results in a solution that is not affected by further refining the mesh. This is, of course, to a certain extent up to engineering judgement, and the engineer needs to make a decision on whether the increased solution accuracy is worth the additional solving time.

By reducing the element size in the component it is possible to monitor the effect of mesh size on the final stress solution. More specifically, the peak stress at the area of interest is monitored. This peak stress location is the inner radius of the outlet flange, as depicted earlier in Figure 4.2. The value of this peak stress is plotted against the number of nodes in Figure 4.7 where it can be seen that increasing the mesh size past approximately 800 000 nodes has little to no effect on the peak stress. Assuming that the result for the finest mesh is the exact solution, it can be seen that the solution converges to a result that varies by less than 2%. It can therefore be said that the final stress solution is converged.

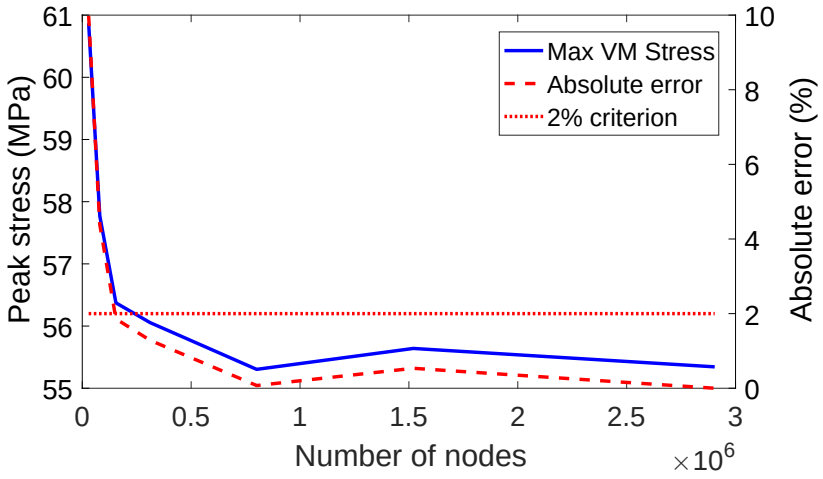

Figure 4.7: Mesh convergence for full model using uniform mesh

4.3 Model simplification

Thus far the elastic model has incorporated the modelling of contact between the valve body and the hydraulic cap (Figure 4.2). Contact models are highly non-linear and hence require multiple iterations to solve. Due to the high coefficient of friction ($\mu = 0.5$) between the components, the model is highly non-linear and takes 11 iterations to solve. When considering the time-dependent model, which in itself is expected to take more than 50 iterations to solve, a highly non-linear model will result in extremely long solving times. By incorporating these contact non-linearities into the model the solving time is expected to increase approximately ten fold (from approximately 50 to 550 iterations).

With the above in mind it is clear that further simplification of the model is required if the solving time for the time-dependent model is to be reduced. Possibly, the largest

time savings can be achieved by eliminating the contact non-linearities. However, simply omitting this contact and fixing the two bodies will result in an overly stiff model due to the lost flexibility between the two bodies. In order to account for this loss in flexibility the hydraulic cap stiffness can be reduced to add a certain amount of compliance between the two bodies, the amount of which depends on the reduction in stiffness.

By reducing the hydraulic cap stiffness, a simulated contact is created from the added cap compliance. This resultant hybrid model is now linear, requiring only a single iteration to solve. Two steps, the results of which are reported thereafter, are required when attempting to simulate the non-linear body contact with a hybrid model of reduced cap stiffness:

1. The model boundary conditions have changed and thus a new mesh convergence study needs to be conducted

2. The correct cap stiffness needs to be determined to simulate the correct amount of contact

In a similar manner to before, mesh density is increased uniformly throughout the component and the peak stress at the area of interest monitored. The results of this mesh convergence study are depicted in Figure 4.8 where it can again be seen that a converged mesh is achieved. By assuming the result for the finest mesh is the exact solution, it can be seen that the stress converges to within 2% of the exact solution.

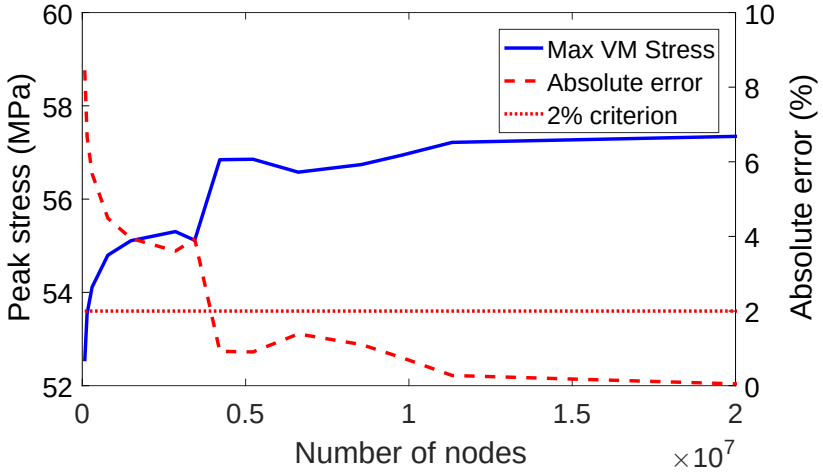

Figure 4.8: Mesh convergence for hybrid cap model using uniform mesh

Along with a mesh convergence study, a mesh refinement was also conducted whereby the mesh density was refined in the area of interest and coarsened far away from this area. This newly designed mesh has the added benefit of a smaller node count, aiding in solution time, but with a similar accuracy. A comparison of the results from the original and designed mesh are tabulated in Table 4.2. Note that the 2% is not achieved, however, the added reduction in solving time outweighs the slight loss in accuracy.

Table 4.2: Comparison of results for uniform and designed mesh of hybrid model

Mesh type	Node count (10^5)	Peak stress (MPa)	Absolute error (%)
Uniform	42.11	56.84	0.92
Designed	20.50	55.91	2.55

The mesh comparison results reported in Table4.2 are a perfect example of how engineering judgement needs to be used when using FE software. Although the designed mesh yielded a larger error, the approximate 50% reduction in the node count results in a solution time which is considerably reduced. This designed mesh along with the hybrid cap implementation will result in extreme time savings, in total reducing the solving time by more than a factor of ten.

Figure 4.9 shows the final mesh of the valve, where important aspects such as the refined area, mesh continuity across the hybrid cap, and minimum element criterion through thin sections can be seen. This is shown in more detail in Figure 4.10.

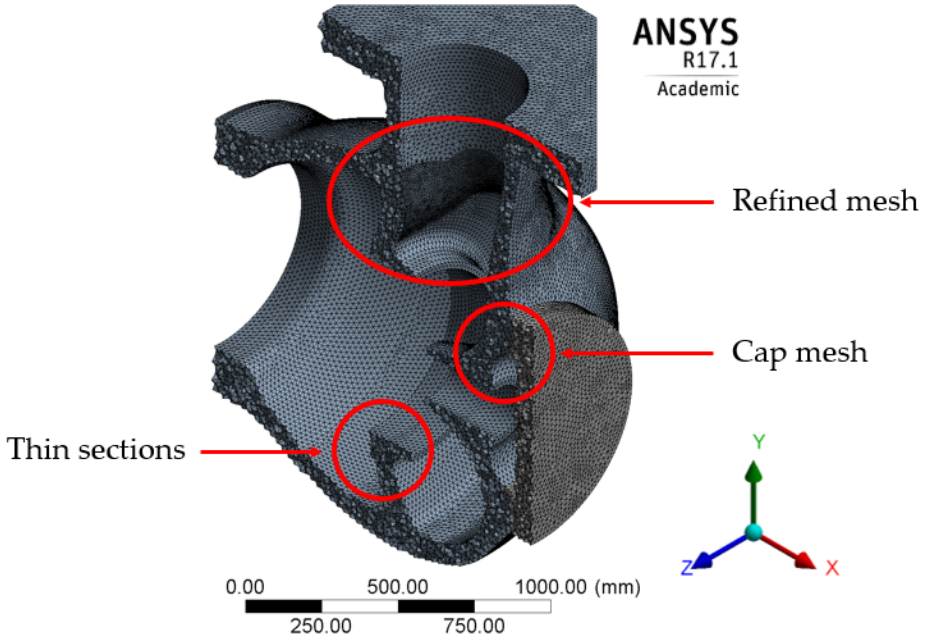

Figure 4.9: Mesh of entire valve body

Finally, the correct cap stiffness has to be selected in order to simulate the right amount of contact. Reducing the cap stiffness introduces more compliance between the two bodies, simulating a reduction in the coefficient of friction between the bodies. Similarly, increasing the stiffness leads to less compliance and a higher simulated coefficient of friction.

By systematically altering the cap stiffness and again monitoring the peak stress, the correct stiffness can be chosen to achieve a simulated coefficient of friction of $\mu = 0.5$ [51] between the bodies. Figure 4.11 shows the results of this stiffness study. From the results it is clear that a higher stiffness results in a higher stress, which is clear evidence of less compliance (more friction) between the two bodies. Using linear interpolation it

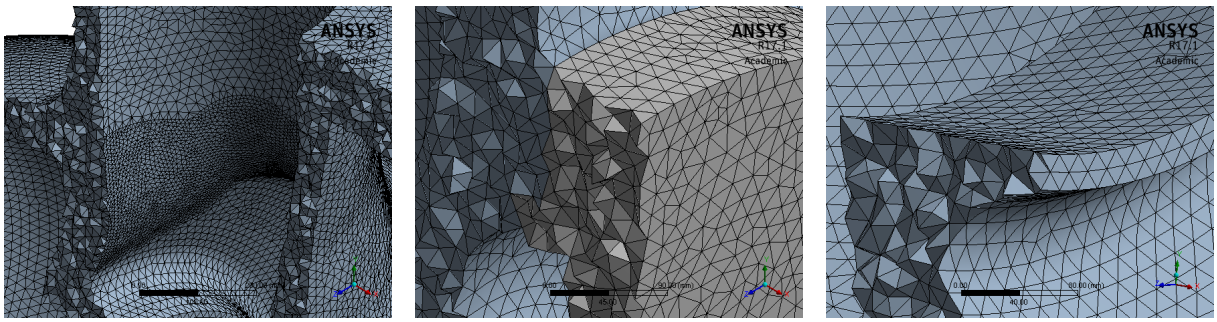

(a) (b) (c)

Figure 4.10: Geometry mesh showing (a) Refined mesh at area of interest, (b) Uniform mesh between valve body and cap, and (c) Minimum of two elements through thickness of thin sections

was determined that a cap stiffness of 81 GPa results in the correct compliance between the two bodies, resulting in, for all intents and purposes, the exact same stress results.

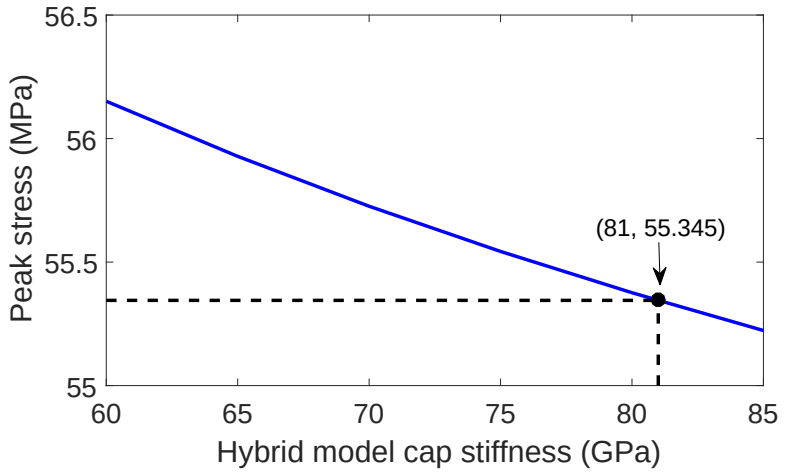

Figure 4.11: Maximum Von-Mises stress at critical flange location for a variation of hybrid cap Young's Modulus

4.4 Model verification

Before one can trust the results from an FEA the model must be verified against analytical calculations and, where possible, validated against experimental results. The processes followed in order to ensure that a valid FE model is used are discussed in the following Section.

4.4.1 Boundary condition verification

At this point it is worth noting that boundary conditions applied to a FE model are often not an exact representation of the actual conditions encountered in practice. However, they are close enough that the small errors introduced are negligible. The frictionless roller supports applied to the valve are assumed to be more restrictive than conditions that would actually be encountered in practice, meaning that artificial forces

are being applied at these supports. However, before adding more complexity to the model it is worth checking that the reaction forces developed at these constraints are close to the expected values.

The valve studied in this thesis is analogous to a pipe with an internal pressure. With this in mind, it is necessary to determine whether the correct axial loads are present in the body by checking that the sum of forces from the internal pressure is equal to the sum of forces normal to the frictionless roller supports. This is checked by ensuring the following criterion, given by Equation 4.1,

$$F_{P_i} - F_R = 0, \tag{4.1}$$

where F_{P_i} are the axial forces caused by the internal pressure P_i, and F_R are the axial reaction forces at the roller supports. The axial forces due to the internal pressure are calculated from the pressure exerted on the internal axial area where the roller supports act. A detailed explanation and set of calculations for these forces are given in Appendix C

The results of from the above test are summarised in Table 4.3 where it can be seen that the largest error of 6.6% occurs at the control side where roller supports were used. This error is sufficiently small to be neglected. One can assume this is due to discrepancies in the calculation simplifications made, as well as the inherent FE error present from modelling a continuous body with discrete elements.

Table 4.3: Summary of boundary condition validation results

Support	F_{P_i} (kN)	F_R (kN)	% Error
Steam inlet	555.2	555.2	0.0
Steam outlet	579.1	579.1	0.0
Control side	1376.3	1285.5	6.6

It is realised that the assumption of frictionless roller supports at the steam inlet and outlet is incorrect, adding artificial displacement restrictions. However, from the results it is clear that the errors introduced are so small that they cannot be seen.

4.4.2 Results verification

Due to the complex geometry of the valve being analysed it is unlikely that analytical models will exist that accurately describe its stress state. However, there are parts of the valve body that resemble simple geometries for which analytical models do exist. More specifically the inlet and outlet flanges resemble thick walled pipes with an inner pressure applied to them. Consider the geometry schematic in Figure 4.12 which highlights the parts on the valve that resemble thick walled pipes. Also shown are two points A and B which will be the locations that are verified against the analytical models.

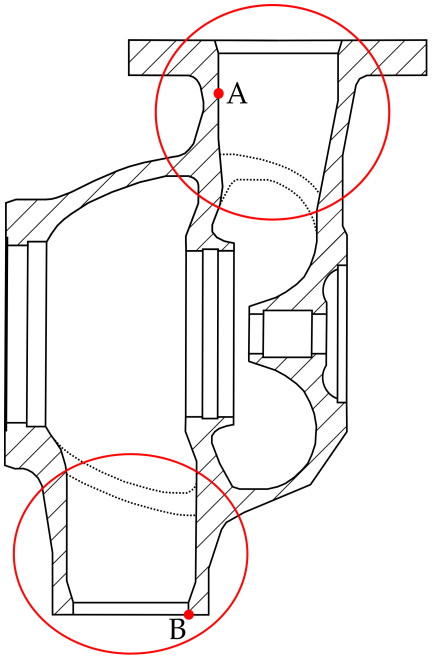

Figure 4.12: Locations of valve body representing thick wall pipes

Consider the axial stress σ_a, hoop stress σ_h and radial stress σ_r in a thick wall cylinder. Thick wall theory states that these three stresses are calculated according to Equations 4.2 through 4.4 [52],

$$\sigma_a = \frac{P_i r_i^2}{r_o^2 - r_i^2}, \tag{4.2}$$

$$\sigma_h = \frac{P_i r_i^2}{r_o^2 - r_i^2}\left(1 - \frac{r_o^2}{r^2}\right), \tag{4.3}$$

$$\sigma_r = \frac{P_i r_i^2}{r_o^2 - r_i^2}\left(1 + \frac{r_o^2}{r^2}\right), \tag{4.4}$$

where r_i is the inner radius, r_o the outer radius, and r the radius to the point in the wall where the stress is required. Note that the location of the verification points is on the inner radius, meaning that $r = r_i$.

The dimensions at both points A and B are summarised in Table 4.4. Note that the inlet and output pipes are not exactly cylindrical, and hence average dimensions were taken close to the point of interest.

Table 4.4: Dimensions at locations A and B

	P_i (MPa)	r_i (mm)	r_o (mm)
A	3.2	260	315
B		240	300

Substituting the dimension values from Table 4.4 into Equations 4.2 to 4.4, and comparing with the results from the FE model shows that a general good agreement is

achieved. The results from this analysis are tabulated in Table 4.5. These errors are due to the fact that the body is not a perfect cylinder at the points of interest. Additionally, the surrounding complex geometry affects the stiffness in the assumed thick walled pipes. Note that the results for point A differ from the theoretical values more than point B. This is due to the fact that the cylinder assumption is more incorrect near point A than it is at point B.

Table 4.5: Dimensions at locations A and B

		Theoretical (MPa)	FEA (MPa)	% Error
A	σ_a	5.69	4.76	16.34
	σ_h	14.58	12.01	17.63
	σ_r	-3.2	-3.18	0.63
B	σ_a	6.84	6.24	8.78
	σ_h	16.88	16.09	4.68
	σ_r	-3.2	-3.18	0.63

The axial stress results documented above add extra confidence in the frictionless roller supports applied at the inlet and outlet. There is an almost exact correspondence between the theoretical and FEA results, meaning that the boundary conditions are not resisting the development of an axial load in these locations.

From the results above it can be concluded that the FEA model corresponds well with expected stress values. The small differences that were noted can be assumed to a more complex geometry than assumed in the theoretical calculations, and not due to an error made in the FE model. With this in mind it can be concluded that the FE model is verified, and the stress distribution throughout the component correct.

4.5 Concluding remarks

This chapter presented the use of an elastic model to quickly determine that convergence criterion were reached. From the studies presented above it can be concluded that a converged elastic model has been achieved. Geometry simplifications were used to decrease mesh size and reduce solving time. The resultant geometry resembles the structural characteristics of the valve, with unnecessary details omitted. The model uses a designed mesh which is refined around the area of interest, reducing the node count with an acceptable error of 2.55%. Lastly, a hybrid cap was introduced into the model. This hybrid cap linearised the model by getting rid of contact between the two bodies. The reduced stiffness of the cap allows for a certain compliance between the bodies without the need to solve highly non-linear equations.

The final reduced model resulted in solving times that were dramatically decreased from the initial full elastic model. With this in mind it can be concluded that the elastic model developed here will result in converged creep results that are both accurate and efficient.

Chapter 5

Steady state FE creep model

From Chapter 3 a methodology was presented that generates a family of creep curves through fitting each of the castings. This methodology was taken a step further, and a stochastic element introduced into the family of creep curves through the use of a multimodal PDF. In Chapter 4 an elastic model was then developed in order to ensure a converged FE solution was obtained. This chapter makes use of both these results to create a steady state FE creep model, where steady state refers to constant loads over time. Results from the implementation of the family of creep curves are reported, and the use of such a model in industry discussed.

5.1 Material model implementation

The creep material model is used in the ANSYS FE code to calculate the creep strain component of the total strain. The total strain is then calculated according to the summation law (Equation 2.12). By Implementing a family of creep curves it is possible to capture the spread of the data and determine worst case scenarios. As has already been made clear, the CTH creep model will be used throughout this study. The original CTH model, repeated here for consistency, is given by Equation 3.1,

$$\varepsilon_{cr} = \frac{x_1 \sigma^{x_2} t^{x_3+1} \exp\left(-\frac{x_4}{T}\right)}{x_3 + 1} + x_5 \sigma^{x_6} t \exp\left(-\frac{x_7}{T}\right), \tag{3.1}$$

where the original unscaled coefficients (x_1, x_2, ..., x_7) are used, as opposed to the scaled coefficients (χ_1, χ_2, ..., χ_7). The coefficients therefore represent the exact coefficients used in ANSYS. A summary of these coefficients for the original castings is reported in Table 5.1. Note that from the optimisation only six of the nine castings resulted in usable castings.

Table 5.1: Summary of original casting CTH model coefficients used in steady state FE creep model

Casting	x_1	x_2	x_3	x_4	x_5	x_6	x_7
VbB	4.16×10^{-3}	1,76	-0,882	11345	5.68×10^{-8}	8,42	40234
VbD	3.40×10^{-5}	1,45	-0,935	5805	2.49×10^{-6}	8,07	41285
VbG	1.57×10^{-3}	1,54	-0,932	9154	4.59×10^{-7}	9,97	48262
VbJ	4.55×10^{-6}	2,15	-0,905	7950	2.72×10^{-8}	9,92	46272
VbM	8.91×10^{-1}	1,32	-0,910	13416	1.13×10^{-10}	13,21	56011
VbN	3.69×10^{-4}	1,67	-0,814	9177	1.22×10^{-12}	12,99	51573

In order to get a more stochastic view of the experimental data, random creep curves were generated using the methods discussed in Section 3.5. The coefficient results from this analysis are summarised in Table 5.2.

Table 5.2: Summary of random CTH model coefficients used in steady state FE creep model

Description	x_1	x_2	x_3	x_4	x_5	x_6	x_7
Set 1	1.20×10^{-5}	1.98	-0.901	0.8105	1.45×10^{-7}	10.34	4.9018
Set 2	2.24×10^{-4}	2.11	-0.891	1.0050	7.41×10^{-8}	9.44	4.5061
Set 3	3.89×10^{-5}	1.80	-0.889	0.8401	7.08×10^{-9}	11.16	5.0148
Set 4	1.10×10^{-3}	2.14	-0.942	1.1099	1.02×10^{-9}	12.01	5.2647
Set 5	7.76×10^{-5}	1.67	-0.850	0.8101	8.51×10^{-7}	9.06	4.5049

By implementing the above CTH models into an ANSYS steady state creep analysis one is able to obtain the creep state in the valve body. Before looking at the results, two key points should be noted:

1. The model was run at steady state conditions. This means it was assumed the valve operates at constant pressure with no temperature gradient through the material (i.e.: No start up or shut down simulated).

2. The ANSYS creep model is not a damage-based model, but rather a strain based material model. This means that tertiary creep is not simulated and the model will theoretically carry on a secondary creep path as time t approaches infinity. This is discussed in more detail in Chapter 6.

5.2 Results

Before displaying the entire set of results, first consider the results for a single casting. The peak Von-Mises creep strain accumulation for casting VbN is plotted over a 100 kh period in Figure 5.1. The peak Von-Mises creep strain distribution at selected time points is shown in Figure 5.2 thereafter. Note that creep strain does not occur instantaneously under load, as does elastic and plastic strain. Rather the creep strain develops slowly over time according to the creep material model used.

In a similar manner the peak Von-Mises stress for casting VbN is plotted over a 100 kh period in Figure 5.3. Note that the stress relaxes over time, and reaches an almost constant value at approximately 20 kh. The relaxation of the peak Von-Mises stress distribution is shown in Figure 5.4. Again, four selected time points are chosen which highlight important changes in the stress distribution. Notice that at time zero the stress distribution is equivalent to the static model stress distribution. This is due to the fact that no creep has occurred.

From the initial results for casting VbN it is clear that the majority of stress relaxation occurs in the initial stages of creep exposure, and the stress remains relatively constant thereafter. In the initial 5 kh period for casting VbN the stress relaxes by 21.5%, thereafter the stress only relaxes a further 7.3% between 5 kh and 100 kh.

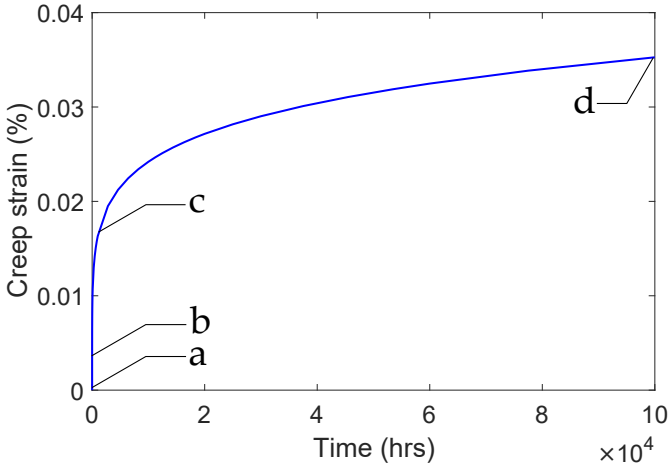

Figure 5.1: Critical Von-Mises creep strain accumulation for casting VbN

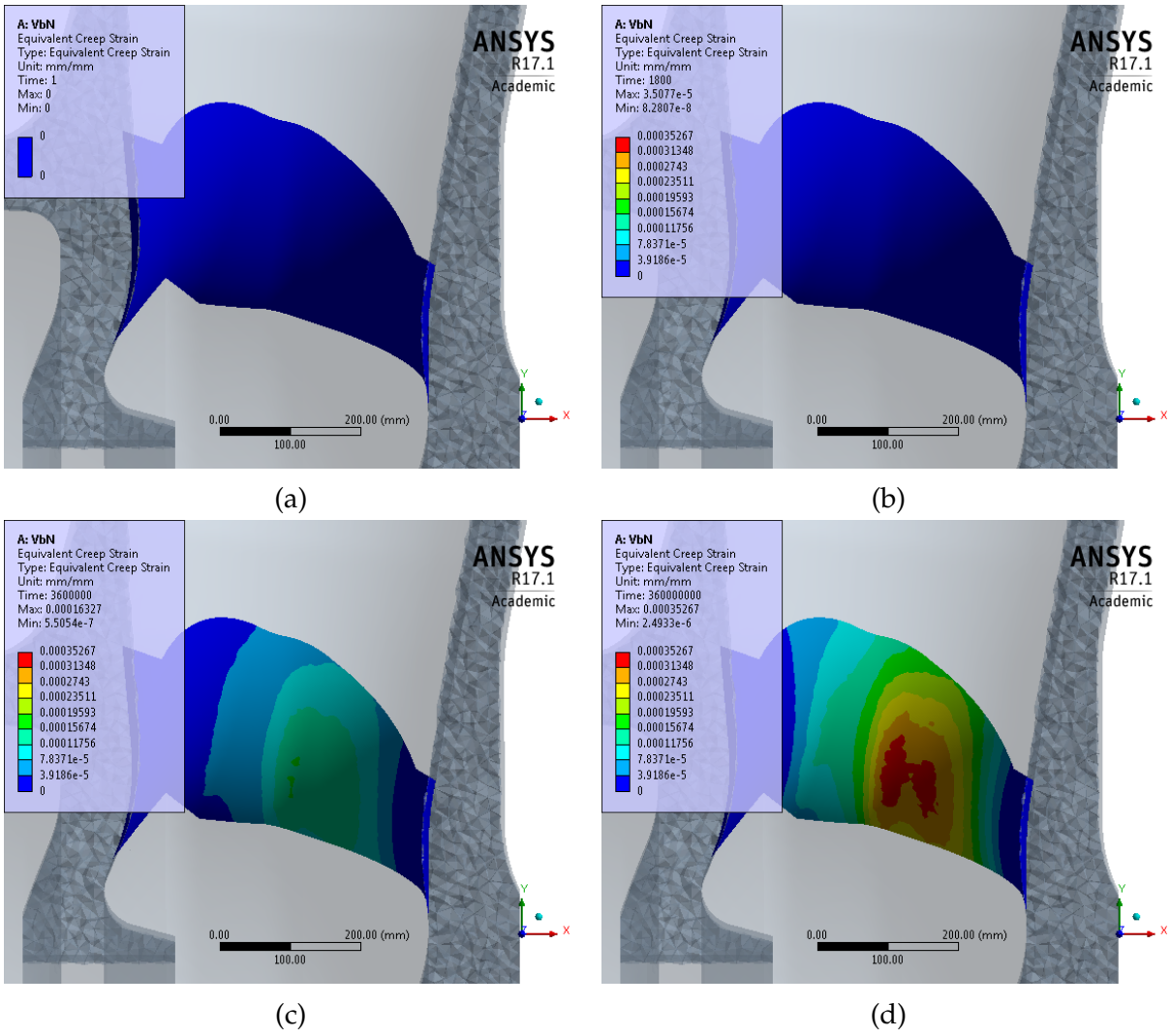

Figure 5.2: Evolution of the peak Von-Mises creep strain distribution over time for (a) t = 0 h, (b) t = 0.5 h, (c) t = 1 kh, and (d) t = 100 kh

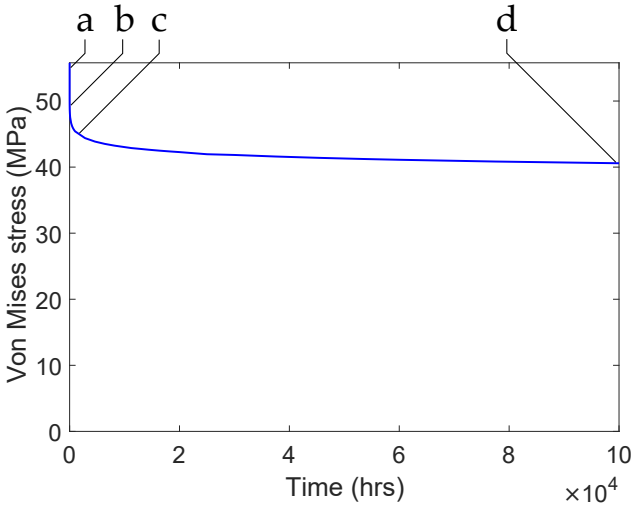

Figure 5.3: Critical Von-Mises stress relaxation for casting VbN

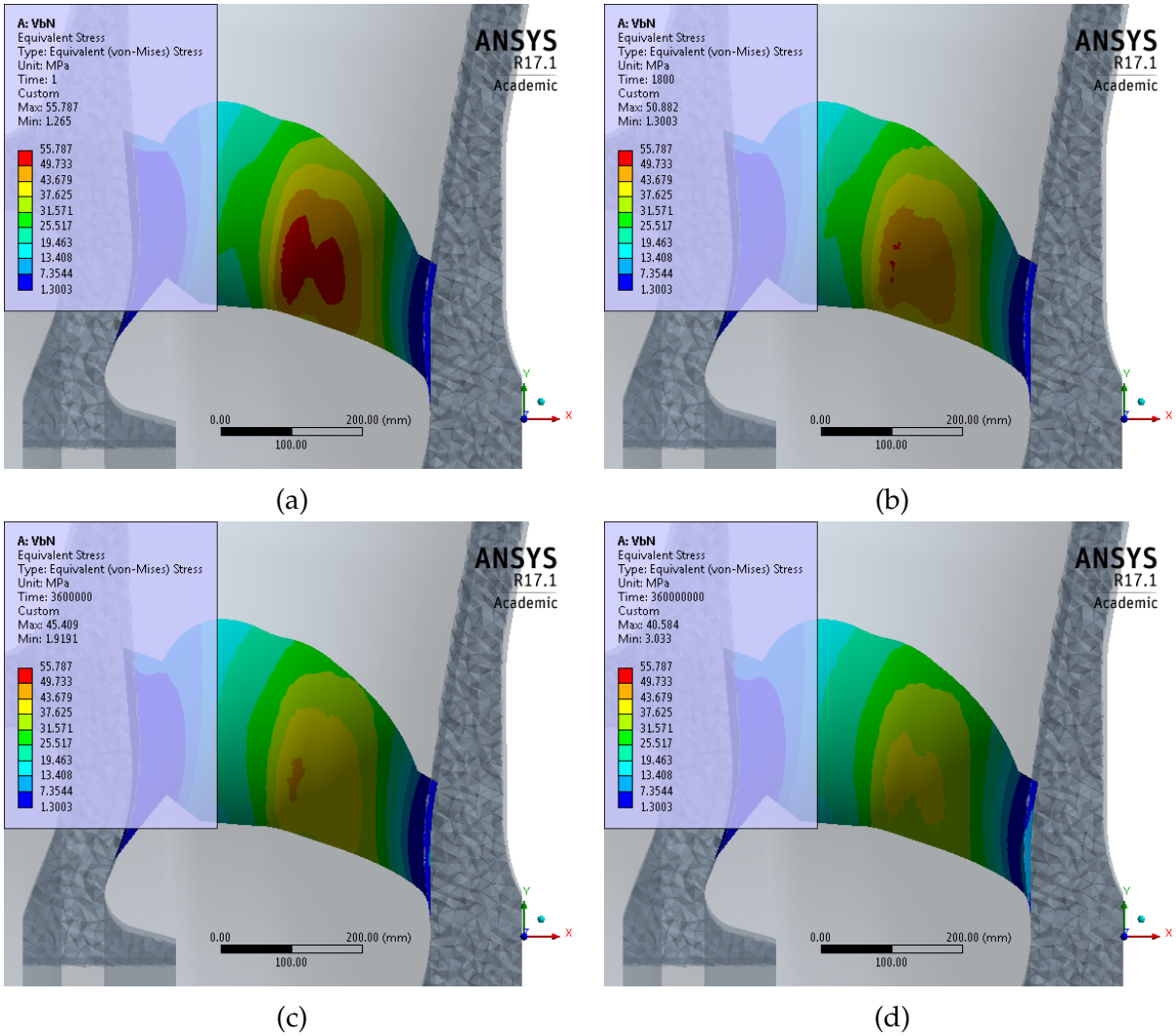

Figure 5.4: Relaxation of peak Von-Mises stress distribution over time for (a) t = 0 h, (b) t = 0.5 h, (c) t = 1 kh, and (d) t = 100 kh

From this initial analysis on casting VbN it can be hypothesised that the majority of stress relaxation is related to the primary creep regime, whereas the secondary creep regime is not necessarily responsible for major stress relaxation. The validity of this statement can be checked by considering the results from the rest of the original castings, as well as the probabilistic models created.

Figure 5.5 plots the accumulation of the peak Von-Mises creep strain over time for all the original castings of Table 5.1. From the results it is immediately clear that the accumulated creep strain is extremely sensitive to the CTH model coefficients. This is the inherent uncertainty which is introduced by the initial scatter in the experimental creep data.

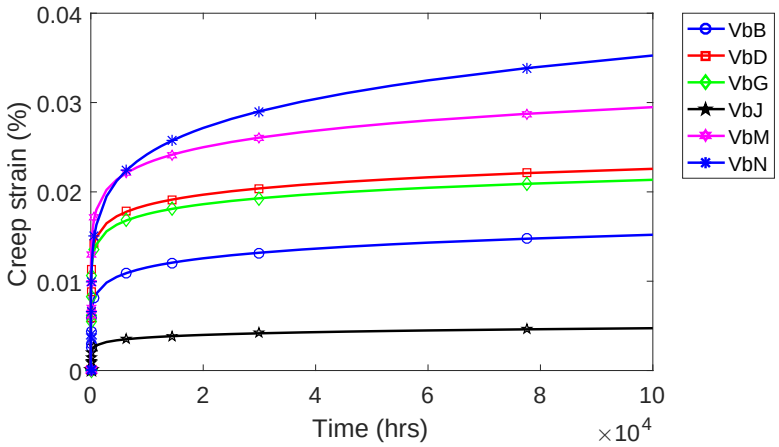

Figure 5.5: Accumulation of peak Von-Mises creep strain for original castings (Note that 10×10^4 h $=$ 100 kh)

The relaxed stress curves for all castings are shown in Figure 5.6. From these results it can be seen that the relaxed stress curves for all the castings do not differ significantly. The reason for this is believed to be the result of the non-linear interaction between stress and strain in the CTH model. It can be seen from the results that although the accumulated creep strains vary quite drastically, by 153%, the final relaxed stresses for the original castings differ by no more than 20%. This result is encouraging and shows that although there is wide scatter in the experimental creep data, and hence the predicted creep strain, the final relaxed stress is relatively constant for the various creep models.

Before continuing it is necessary to ask the question, why is a long term steady state FE creep model required? If the relaxed stress remains constant past approximately 5 kh, is it possible to predict the creep strain using this relaxed stress? The FE model is then only required to determine the relaxed stress in the initial period, and the creep strain is extrapolated thereafter.

A small study done, again using casting VbN, showed that by assuming a constant stress after 5 kh, 10 kh and 20 kh, the creep strain could be almost exactly predicted. The results for each of these approximations in comparison to the actual model are reported in Table 5.3. Note that as we use a more accurate relaxed stress, which is a stress

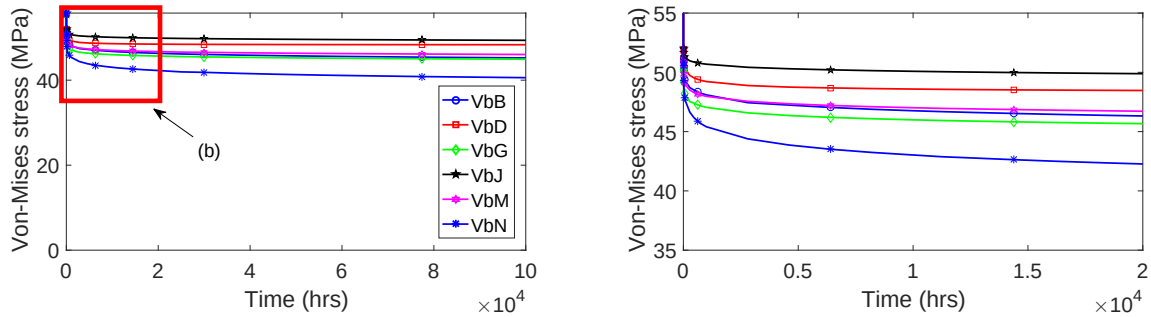

Figure 5.6: Relaxation of peak Von-Mises stress for original castings for (a) entire stress relaxtion over 100 kh, and (b) initial relaxation over 20 kh

at a larger time period, the error gets smaller. However, the error for all three approximations is less than 5%, and it can therefore be assumed that a 5 kh approximation is sufficient. The results from this study are shown in Figure 5.7. Note that although an error is introduced into the result, the approximation is conservative.

Table 5.3: Summary of extrapolation errors made for a variety of approximation times

Approximation time	100 kh creep strain	% Error
5 kh	0.02329	3.14
10 kh	0.02313	2.43
20 kh	0.02297	1.72

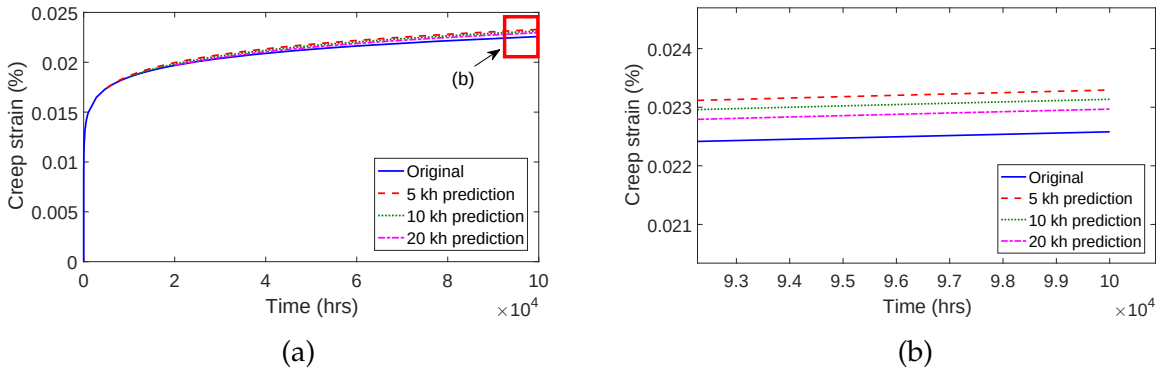

Figure 5.7: Comparison of extrapolation results for casting VbN creep strain at multiple approximation times for (a) the entire 100 kh range, and (b) final results at 100 kh

From this analysis it can be concluded that it is not necessary to run a steady state creep model to 100 kh. Rather, it can be run up to 5 kh to determine the relaxed stress, and the creep strain extrapolated thereafter using this assumed constant relaxed stress.

With the above results in mind, the random creep models generated were run for 5 kh and the accumulated creep strain predicted up to 100 kh. The peak creep strain and stress results for all models, original and random, are shown in Figure 5.8. From the

results it can again be seen that although there is a large variation amongst the input creep curves, there is, in comparison, a very small difference between the the relaxed stress. More specifically, the relaxed stresses differ by no more than 21% for variations of up to 153% in the creep strain models.

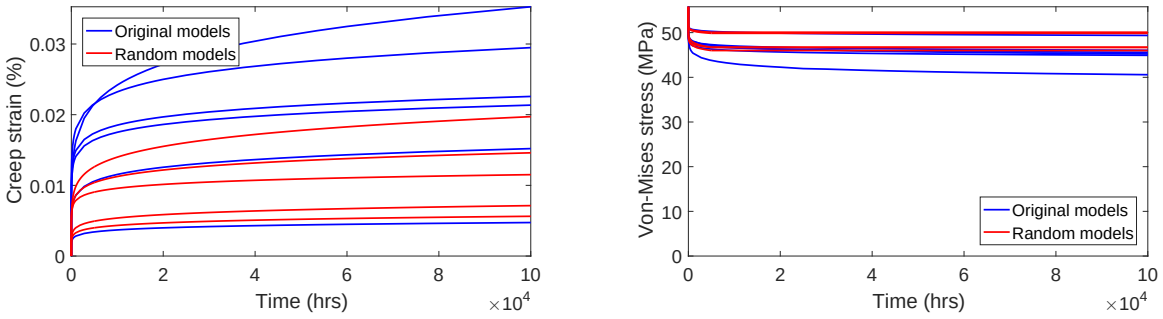

(a) (b)

Figure 5.8: Complete set of results for both original and random castings for (a) peak Von-Mises creep strain, and (b) peak Von-Mises stress

5.3 Discussion of results

This chapter has presented the results from a steady state FE creep analysis using the CTH creep models that were developed in Chapter 3, and the FE model from Chapter 4. The original scatter in the experimental data, due to a combination of different casting microstructures and normal creep data scatter, leads to a large variation in the accumulated creep strain. However, although the accumulated creep strain over time varies by up to 152.6% amongst the castings, the non-linear interaction between stress and strain leads to relaxed stresses that vary by no more than 21.1%.

Additionally, it was hypothesised that the initial stress relaxation is related to the primary creep regime, whilst the almost steady state stress thereafter is related to the secondary creep regime. From looking at the complete set of results it can be concluded that this is in fact true, and the initial stress relaxation is related to the primary creep regime. The time frame associated with this relationship is probably of more importance than the relationship itself. The time frame means that the relaxed stress can be assumed constant after a relatively short period of time. In this case, the relaxed stress can be assumed constant after only 5 kh. The accumulated creep strain can then be calculated analytically from the creep material model used, meaning that long term FE creep models are not necessary. This greatly reduces the time required for single runs, promoting the use of multiple creep models to get a stochastic view of all possible stress scenarios.

When running a single model the that fits experimental data in an average sense, the engineer is inherently introducing errors into their analysis. When material scatter is severe, as is usually the case with creep, these errors are magnified. However, by utilising the above results, one is capable of running multiple models over reduced time

periods, thus making use of models that capture the entire set.

The next chapter will discuss the use of the above results in making remaining useful life predictions, using both time-based and strain-based formulae.

Chapter 6

Failure prediction

One of the objectives of this study is to develop a methodology to quantify the creep life of components through the use of FEA. This chapter will discuss two methods for estimating creep life, namely time-based and strain-based methodologies. The results from Chapter 5 will be heavily relied upon for both of these methodologies. It should however be noted that the operating conditions of the IP valve are outside the range of the experimental data, and thus there will be an inherent error introduced into the failure predictions.

6.1 Time-based analysis

When calculating component creep life the engineer will commonly make use of the time-temperature parameters discussed in Section 2.4. These parameters make use of creep rupture data for a variety of temperature and stress combinations, which are commonly elevated to higher values to accelerate the creep tests. The benefit of using the time-temperature parameters is that they are deformation mechanism independent, and are therefore not affected by the different deformation mechanisms present at these elevated temperatures and stresses.

An extract of a rupture data set from the NIMS database is given in Table 6.1, where the rupture data for casting VbD is tabulated for 773 K and 823 K. Note the increasing rupture times, from small times of approximately 24 h, to longer times of approximately 100 kh. The variation in temperature and stress combinations therefore results in a mixture of accelerated and long term creep tests.

Table 6.1: Extract of NIMS creep rupture data for casting VbD at a variety of temperature and stress combinations [46]

T (K)	σ (MPa)	t_r (h)	T (K)	σ (MPa)	t_r (h)
773	412	23.6	823	294	64.0
	373	170.0		235	1414.0
	294	2992.8		196	5742.5
	265	12130.7		176	12195.9
	235	22533.5		157	19216.8
	196	111232.9		137	40616.6

The form of the NIMS rupture data encourages the use of the Larson-Miller (L-M) parameter, which is one of the time-temperature parameters used in the calculation of

creep lifetime. The L-M parameter P_{LM} is given as a function of the temperature T and time to failure t_f,

$$P_{LM} = f(\sigma) = T(\log t_f + C), \tag{2.3}$$

where C is a constant [21]. C is reported to be approximately 20 [53, 54], and this is the value that has been chosen for these calculations.

When formulating the L-M parameter, the failure time t_f can be defined as either the time to actual component rupture t_r, or the time to a specific predefined strain, such as the time to tertiary creep t_{ter} [22]. The latter is the more conservative assumption, and would be preferred in an industrial application. Both formulations of the failure time t_f will be investigated here.

As discussed in Section 2.4, the L-M parameter can be plotted against stress, with a polynomial of sufficient order fitted through the data. This polynomial is then used to make failure time estimations at different temperature and stress combinations. For this data set it was determined that a simple logarithmic polynomial is sufficient to capture the data. This polynomial is given by,

$$\sigma = A + B\log(P_{LM}), \tag{6.1}$$

where A and B are constants that need to be determined.

Equation 6.1 is fitted to both the creep rupture and time to tertiary creep NIMS data,

$$\sigma_r = 13901.74 - 3192.86\log(P_{LM}), \tag{6.2}$$
$$\sigma_{ter} = 14575.22 - 3352.88\log(P_{LM}). \tag{6.3}$$

The results for each fit are shown in Figure 6.1.

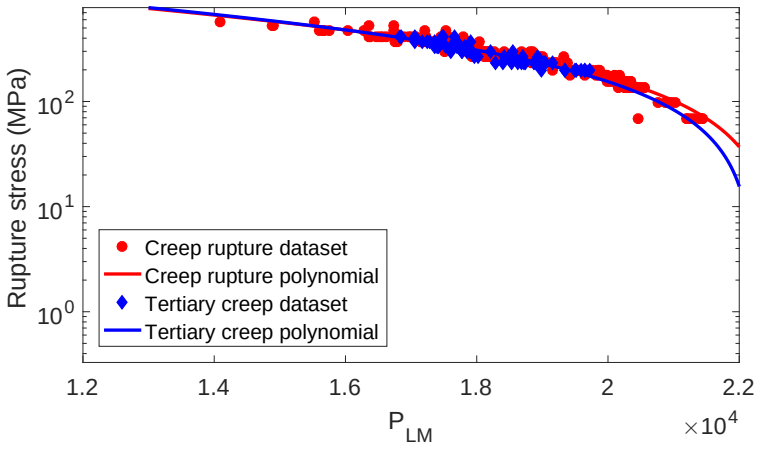

Figure 6.1: Plot of stress vs L-M parameter using NIMS creep rupture data [46]

In order to demonstrate the application of a time based failure analysis, consider the worst case scenario results from Chapter 5. By using the worst case scenario relaxed

stress the engineer is making a conservative calculation, assuming that the microstructure at the location of the peak stress is such that the largest relaxed stress will occur there. From Chapter 5 the worst case relaxed stress is 50.09 MPa. Lifetime calculations were carried out through manipulation of the L-M parameter, allowing one to estimate creep life for arbitrary temperature and stress combinations. A sample lifetime calculation showing this is given in Appendix D.

The results from using both the rupture and tertiary creep formulation are summarised in Table 6.2. From the results it is clear that at these low stresses failure will not occur due to creep alone. Additionally, as expected, the tertiary creep formulation is more conservative. This is due to the fact that failure is associated with the onset of tertiary creep as opposed to actual material rupture.

Table 6.2: Life time results for worst case scenario relaxed stress

Problem formulation	Stress (MPa)	P_{LM}	t_r (h)	t_r (years)
Rupture	50.09	21793.17	68.06×10^6	7764
Tertiary creep		21485.00	27.50×10^6	3137

It should be noted from the results that very small differences in the L-M parameter result in large differences in the predicted time to failure. This is due to the sensitivity and uncertainty in the L-M parameter formulation. However, by utilising the tertiary creep formulation the user is automatically adding a safety factor to the analysis that accounts for this uncertainty in the L-M formulation.

In a similar manner, one can predict the stress at which failure will occur at 100 kh, 200 kh and 300 kh, at the operating temperature of 783 K. These stresses are reported in Table 6.3, where the tertiary creep L-M formulation has been used for conservatism. It can be seen that these stresses are significantly higher than the relaxed stresses obtained in Chapter 5.

Table 6.3: Maximum relaxed stress calculated for specified required lifetimes

Required lifetime, t_r (10^3 h)	P_{LM}	Stress (MPa)
100	19575	185.66
200	19811	168.21
300	19949	158.10

Assuming a worst case scenario, in which no stress relaxation occurs, it is possible to estimate the operating pressure at which these reported failure stresses will occur. Due to the 1:1 (stress:pressure) scaling of the linear static model from Chapter 4 it is possible to estimate the required operating pressure for failure at any of the above lifetimes. This is accomplished by utilising the operating pressure of 3.2 MPa and resultant static model stress of 55.35 MPa as follows for a 200 kh lifetime,

$$\begin{aligned}\frac{P_{200\text{ kh}}}{3.2} &= \frac{\sigma_{200\text{ kh}}}{55.35}\\ P_{200\text{ kh}} &= 3.2\left(\frac{168.21}{55.35}\right)\\ &= 9.73\text{ MPa}.\end{aligned} \tag{6.4}$$

Commonly, in pressure vessel analysis, the linearised membrane stress is considered as opposed to the peak stress. Peak stresses are known to cause localised yielding in pressure vessels. This stress usually then redistributes to the surroundings, and hence does not cause failure. the linearised membrane stress is therefore a better representation of the likelihood of global failure, and should be used when peak stresses warrant concern. However, using the peak stresses is conservative in life estimation.

6.2 Strain-based analysis

An alternative method of determining creep life is by a strain based analysis. The premise of this analysis is to ensure that the inelastic strain does not exceed the limits defined in codes such as the German Technical Guidelines for Steam Boilers [18], or the ASME Limits for inelastic strains [17]. This section will focus on the later, which states that limits for the principal strains defined in each direction are as follows [17]:

- 1% inelastic strain averaged over the wall thickness
- 2% inelastic strain determined at the surface and with a linear distribution of strain through the wall thickness
- 5% inelastic strain, local on any arbitrary spot

The variation in accumulated creep strains, due to the nature of the multi-model approach utilised, will inherently result in a variation in predicted lifetimes using a strain-based approach. Therefore, a worst case scenario will again have to be used in determining the time to the above strain limits. From the results presented in Chapter 5 it is seen that casting VbN results in the maximum accumulated creep strain.

Using the extrapolation technique developed in Chapter 5 it is possible to determine the creep strain analytically using the CTH model for any given strain. For consistency, consider the CTH model for casting VbN given by,

$$\varepsilon_{cr} = \frac{3.69\times10^{-4}\sigma^{1.67}t^{0.186}\exp\left(-\frac{9177}{T}\right)}{0.186} + 1.22\times10^{-12}\sigma^{12.99}t\exp\left(-\frac{51573}{T}\right), \tag{6.5}$$

where the model coefficients x_1, x_2, ..., x_7 are explicitly given in the equation. The creep strain can now be calculated for any arbitrary time t, stress σ and temperature T.

It should be noted that the CTH model is a combined primary and secondary creep model, and does not consider tertiary creep. The model will therefore continue infinitely without the exponential increase in creep strain, considered as tertiary creep. The user must thus exercise caution when predicting creep strains at long times with this model. In order to avoid this problem the user could consider the worst case time to tertiary creep calculated in Section 6.1, and assume the CTH model can not accurately predict the creep strain past this time t_{ter}. From Table 6.2 this time is 27.50×10^6 h.

The resultant accumulated creep strain extrapolated from the VbN casting is 0.1% at 27.50×10^6 h. This is only a small fraction of the surface strain limit of 2% inelastic strain defined by ASME [17]. This result confirms the findings from the time-based analysis, strengthening the argument that failure will not occur due to creep alone in the IP valve of interest.

6.3 Concluding remarks

The two approaches utilised prove that, under the specific set of operating conditions, the IP valve of interest is in no danger of failing due to creep alone. The time-based analysis showed that the low pressures result in a stress small enough that neither rupture or tertiary creep will occur in the foreseeable future. Similarly, the strain based analysis resulted in creep strains well below the ASME specifications [17]. The extrapolation time was limited to the predicted time to tertiary creep from the time-based analysis. This is due to the fact that the CTH model does not account for tertiary creep.

It should be noted that the two methods discussed in this chapter both include considerable uncertainty. They should therefore always be used with very conservative assumptions. Further, it is recommended that both tests should be applied, and the more conservative estimate should be taken.

Chapter 7

Conclusions and recommendations

The aim of this thesis was to make use of the available NIMS creep data for a 1Cr-1Mo-0.25V cast alloy steel, and develop a methodology that quantifies the creep state of components through the use of FEA. This thesis specifically focused on the application of this to an IP valve currently in operation in a South African power plant.

By making use of the NIMS creep data it was seen that a single creep model approach was infeasible. Variation in the data meant that a single model was not able to adequately characterise the data, resulting in little confidence in predictions. A multi-creep-model approach was therefore utilised to accurately capture the entirety of the data set. This method made use of an unconstrained optimisation algorithm to determine the CTH creep model coefficients for each casting separately. These models, along with five randomly generated models, were used to represent the entirety of the NIMS data set.

A static FE model was then utilised to ensure that the correct boundary conditions and mesh controls were applied. The complex nature of the geometry meant that few analytical calculations could be done to verify the FE results. However, by making adequate thick wall assumptions it was possible to verify the solution in specific locations. With a converged and verified model it was then possible to run a steady state FE creep model, incorporating the 11 creep models that were optimised.

A steady state model was considered, in which the temperature and pressure remained constant over time. By implementing the multi-creep-model approach into the ANSYS FEA software it was seen that large variations in creep strain models resulted in a, relatively speaking, narrow banded relaxed stress. Quantitatively, a variation of 153% in the creep strain only resulted in a 21% variation in the relaxed stress. Additionally it was shown that long term 100 kh FE simulations are not required to obtain useful results. It was shown that using a 5 kh FE simulation it is possible to accurately extrapolate both creep strain and relaxed stress results to longer times. These results were then used to make lifetime predictions for a worst case scenario, using both a time-based and strain-based approach. The results from this analysis showed that, due to the low operating pressures in the IP valve, the component would not fail due to creep, and in fact has an almost infinite creep life.

It should however be noted that the ANSYS creep model used in this research is only capable of modelling primary and secondary creep, and does not consider tertiary creep. The engineer is therefore required to make an offline decision on the extent to

which the model can be used. One possible method, introduced in Chapter 6, was the use of a tertiary based L-M formulation. This will allow the engineer to make estimations as to the time to tertiary creep, which can be used as a cut-off time for the FE model. However, it is recommended that future work investigates the use of an offline strain-based tertiary creep model, which can be used to alert the user that the FE model is no longer accurate.

Further improvements could be made to the results by incorporating a transient thermal analysis into the model. This study only considered a steady state situation, in which the temperature was considered constant with a zero differential through the material. More accurate results could therefore be achieved by including the transient start up and shut down periods, in which temperature differentials are present through the thickness of the component. These results could then be utilised in a life fraction calculation, where these transient conditions are all considered.

In concluding it can be said that through the use of the multi-creep-model approach introduced here, the engineer is able to more accurately characterise a creep data set. Large components, such as the IP valve analysed here, will inherently have a variation of microstructures through its volume. By utilising the multi-creep-model approach the engineer is including this microstructure uncertainty into their analysis, thus reducing the uncertainty in FE based life calculations. The narrow banded relaxed stress solution means that worst case scenario lifetime calculations can then be made through the use of either time-based or strain-based methods. The accuracy of these results is however limited by the steady state assumption made at the start of this investigation. An improvement in the results could be obtained by incorporating the thermal transients into the model, with an improved offline tertiary creep model.

Bibliography

[1] C. Borgnakke and R. E. Sonntag, *Fundamentals of Thermodynamics*. John Wiley and Sons, seventh ed., 2009.

[2] M. E. Kassner, *Fundamentals of creep in metals and alloys*. Elsevier, 2009.

[3] M. Hussain, *Use of replication and portable hardness testing for high temperature plant integrity and life assesment*, Power and plant operations seminar, Pakistan, May 2011.

[4] G. Sposito, C. Ward, P. Cawley, P. B. Nagy, and C. Scruby, "A review of non-destructive techniques for the detection of creep damage in power plant steels," *NDT and E International*, vol. 43, no. 7, pp. 555–567, 2010.

[5] G. E. Dieter, *Mechanical metallurgy*, ch. Creep and stress rupture. McGraw–Hill, 1986.

[6] G. E. Dieter, *Mechanical metallurgy*, ch. Metallurgical fundamentals. McGraw–Hill, 1986.

[7] R. W. Evans and B. Wilshire, *Creep of metals and alloys*. The institute of metals, 1985.

[8] D. Ando, Y. Sutou, and J. Koike, "Internal microstructure observation of enhanced grain-boundary sliding at room temperature in az31 magnesium alloy," *Materials Science and Engineering*, vol. 666, no. A, pp. 94–99, 2016.

[9] W. Stumpf, *Mechanical metallurgy*, ch. Creep deformation. University of Pretoria, 2015.

[10] R. W. Hertzberg, *Deformation and fracture mechanics of engineering materials*. John Wiley and Sons, 1st ed., 1976.

[11] R. L. Coble, "A model for boundary diffusion controlled creep in polycrystalline materials," *Journl of Applied Physics (U.S.)*, vol. 34, pp. 1679–1682, June 1963.

[12] M. F. Ashby, "A first report on deformation-mechanism maps," *Acta Metallurgica*, vol. 20, no. 7, pp. 887–897, 1972.

[13] M. F. Ashby, C. Gandhi, and D. M. R. Taplin, "Fracture mechanism maps and their construction for f.c.c. metals and alloys," *Acta Metallurgica*, vol. 27, pp. 699–729, May 1979.

[14] B. Wilshire and A. L. Battenbough, "Creep and creep fracture of polycrystalline copper," *Materials science and engineering*, vol. 443, pp. 156–166, 2007.

[15] J. Salonen, P. Auerkari, O. Lehtinen, and M. Pihkakoski, "Experience on in-service damage in power plant components," *Engineering Failure Analysis*, vol. 14, no. 6, pp. 970–977, 2007.

[16] M. Willcox and G. Downes, "A brief description of ndt techniques," *Insight NDT equipment Limited*, vol. 771, pp. 1–22, 2000.

[17] ASME, *Limits for inelastic strains*, section III, division 1 - NH, appendix T, article T - 1310 ed., n.d.

[18] *TRD 508: Technische Regeldn fur dampfkessel und Zusatzliche prufungen and Bauteilen berechnet mit zeitabhangign festigkeitskenwerten*, July 1986. Technical Guidlines for Steam Boilers.

[19] B. J. Cane, "Remaining creep life estimation by strain assesment on plant," *International Journal of Pressure Vessels and Piping*, vol. 10, pp. 11–30, 1981.

[20] N. E. Dowling, *Mechanical behaviour of materials: Engineering methods for deformation, fracture, and fatigue*. Pearson, 4th ed., 2012.

[21] F. R. Larson and J. E. Dorn, "A time-temperature relationship for rupture and creep stresses," *Transactions ASME*, vol. 74, no. 5, pp. 765–775, 1952.

[22] F. T. Furillo, S. Purushothaman, and J. K. Tien, "Understanding the Larson-Miller parameter," *Scripta Metallurgica*, pp. 493–496, 1977.

[23] E. Hosseini, *Prediction of long term creep rupture properties of welded joints using the results of short duration creep incubation tests*. PhD thesis, Sharif University of Technology, Tehran, Iran, 2013.

[24] S. R. Holdsworth, "Creep resistant materials for steam turbines," *Encyclopedia of Materials Science and Technology*, vol. 1–11, pp. 1837–1843, 2001.

[25] K. H. Mayer and F. Masuyama, *Creep resistant steels*, ch. The developement of creep resistant steels, pp. 15–70. Woodhead Publishing, 2008.

[26] P. J. Ennis and A. Czyrska-Filemonowicz, "Recent advances in creep resistant steels for power plant applications," *Ommi*, vol. 1, no. 1, pp. 1–28, 2002.

[27] S. R. Holdsworth, *Creep-Resistant Steels*, ch. Constitutive equations for creep curves and predicting service life, pp. 403–420. Woodhead Publishing, 2008.

[28] P. Phillips, "The slow stretch in indiarubber, glass, and metal wires when subjected to a constant pull," *Proceedings of the Physical Society of London*, vol. 19, no. 1, pp. 491–513, 1905.

[29] A. Graham and K. F. A. Walles, "Relations between long and short time properties of commercial alloys," *Journal of Iron and Steel Institute*, vol. 179, pp. 105–120, 1955.

[30] P. G. McVetty, "Factors affecting the choice of working stresses for high temperature service," *Transactions ASME*, vol. 55, pp. 13–99, 1933.

[31] J. B. Conway and M. J. Mullikin, "An evaluation of various first stage creep equations," in *Proceedings AIME Conference*, (Detroit, Michigan), 1962.

[32] F. H. Norton, *The creep of steel at high temperatures*. McGraw—Hill, 1929.

[33] A. Nadia, "The influence of time upon creep, the hyperbolic sine creep law," *Stephen Timoshenko Anniversary*, pp. 155–170, 1938.

[34] T. H. Hyde, A. A. Becker, W. Sun, and J. A. Williams, "Finite-element creep damage analyses of P91 pipes," *International journal of pressure vessels and piping*, vol. 83, no. 11, pp. 853–863, 2006.

[35] A. A. Becker, T. H. Hyde, W. Sun, and P. Andersson, "Benchmarks for finite element analysis of creep continuum damage mechanics," *Computational Materials Science*, vol. 25, pp. 34–41, 2002.

[36] T. H. Hyde, L. Xia, and A. A. Becker, "Prediction of creep failure in aeroengine materials under multi-axial stress states," *International journal of Mechanical Sciences*, vol. 38, no. 4, pp. 385–401, 1996.

[37] B. Wilshire and P. J. Scharning, "Prediction of long term creep data for forged 1cr-1mo-0.25v steel," *Materials Science and Technology*, vol. 24, no. 1, pp. 1–9, 2008.

[38] NIMS, "Data sheet 9B, data sheets on the elevated temperature properties of 1Cr–1Mo–0.25V steel forgings for turbine rotors and shafts," tech. rep., National Research Institute for Metals, Tokyo, Japan, 1990.

[39] B. Wilshire and M. Whittaker, "Recent developments in creep and creep fracture," tech. rep., Swansea University: Materials research centre, September 2012.

[40] S. Goyal, K. Laha, C. R. Das, P. Selvi, and M. D. Mathew, "Finite element analysis of uniaxial and multiaxial state of stress on creep rupture behaviour of 2.25Cr-1Mo steel," *Material science and engineering A*, vol. 563, pp. 68–77, 2012.

[41] F. Ellis and R. Zielke, "Creep constitutive equations for 1CrMoV bolt material," *ASME: Fitness for service evaluations and non-linear analysis*, pp. 75–82, 2002.

[42] ANSYS®Academic Research, Release 16, *Mechanical APDL Materials Reference: Rate-Dependant Plasticity*, ANSYS, Inc.

[43] ANSYS Inc, *ANSYS Mechanical: Advanced Nonliear Materials, Rate Dependent Creep*, July 2014.

[44] J. Arora, *Introduction to optimum design*. Elsevier, 3 ed., 2012.

[45] NIMS and K. Kimura, "Data sheet 31B, data sheets on the elevated temperature properties of 1Cr–1Mo–0.25V steel castings for steam turbine casings," March 2016. Email enquiry with NIMS institute.

[46] NIMS, "Data sheet 31B, data sheets on the elevated temperature properties of 1Cr–1Mo–0.25V steel castings for steam turbine casings," tech. rep., National Research Institute for Metals, Tokyo, Japan, 1990.

[47] W. H. Press, *Numerical recipes: The art of scientific computing*. Press sydicate of the University of Cambridge, 1987.

[48] S. Towers, "Polymatheia: Simplex method." `http://sherrytowers.com/2014/07/14/simplex-method/`, July 2014. Accessed: 10 February 2016.

[49] C. Bishop, *Pattern recognition and machine learning*, ch. 2: Probabilty distributions. Springer, 2006.

[50] R. G. Budynas and J. K. Nisbett, *Shigley's mechanical engineering design*, ch. Screws, Fasteners, and the Design of Permanent Joints. McGraw Hill, 2011.

[51] The Engineering Toolbox, "Friction and friction coefficients." `http://www.engineeringtoolbox.com/friction-coefficients-d_778.html`, nd. Accessed: 20 March 2016.

[52] P. Benham, R. Crawford, and C. Armstrong, *Mechanics of engineering materials*. Pearson, 2 ed., 1996.

[53] H. Kim, "Assessment of creep life fraction for in-service high-temperature components," *Engineering failure analysis*, vol. 12, no. 4, pp. 578–585, 2005.

[54] M. Santos, M. Guedes, R. Baptista, V. Infante, and R. Claudio, "Effect of severe operation conditions on the degradation state of radiant coils in pyrolysis furnaces," *Engineering failure analysis*, vol. 56, pp. 194–203, 2015.

Appendix A

NIMS casting specifications

This appendix summarises the specifications of the various NIMS castings used throughout the report. Table A.1 summarises the most important of the casting details. It is important to note that the different deoxidation processes and thermal histories results in a variation of grain sizes. Note that a mixture of water blast cooling (WBC), blast cooling (BC) and air cooling (AC) are made use of.

Table A.1: Summary of important details for 1Cr-1Mo-0.25V steel castings [46]

NIMS reference code	Deoxidation	Thermal history	Austenite grain size number	Rockwell hardness (HRB)
VbA	Ca-Si killed	1050°C/15h WBC 730°C/15h AC	5.9	96
VbF			6.2	98
VbH			6.1	101
VbB	Si killed	650°C/10h → 720°C/20h FC	6.3	98
VbG		1050°C/15h BC	5.9	97
VbM		720°C/20h FC	5.9	97
VbD	Ti killed	1025°C/8h AC 690°C/15h FC	7.3	98
VbJ			7.1	99
VbN			8	97

Finally, the chemical composition of the various castings is listed in Table A.2.

Table A.2: Chemical composition of 1Cr-1Mo-0.25V steel castings [46]

Ref.	Chemical composition (mass percent)											
	C	Si	Mn	P	S	Ni	Cr	Mo	Cu	V	Al	N
VbA	0,17	0,39	0,60	0,022	0,020	0,11	1,31	1,02	0,11	0,28	0,004	0,0078
VbB	0,16	0,47	0,62	0,010	0,010	0,19	1,01	0,92	0,15	0,24	0,003	0,0111
VbD	0,14	0,34	0,73	0,010	0,009	0,13	1,06	0,96	0,08	0,23	0,003	0,0102
VbF	0,18	0,37	0,66	0,018	0,017	0,10	1,07	1,03	0,12	0,30	0,020	0,0081
VbG	0,16	0,47	0,62	0,010	0,010	0,19	1,00	0,92	0,15	0,24	0,002	0,0104
VbH	0,18	0,37	0,61	0,019	0,018	0,11	1,09	1,12	0,07	0,28	0,016	0,0064
VbJ	0,16	0,52	0,79	0,010	0,008	0,13	1,16	0,97	0,11	0,23	0,003	0,0106
VbM	0,18	0,39	0,63	0,012	0,012	0,23	1,22	0,89	0,17	0,23	0,002	0,0103
VbN	0,15	0,52	0,78	0,010	0,009	0,12	1,17	0,98	0,08	0,23	0,003	0,0106

Appendix B

Creep model optimisation results

A summary of the optimisation results from Chapter 3 is included in this appendix. These results are shown in Figures B.1 to B.6. Each Figure includes the results for temperatures of (a) 723 K, (b) 773 K, and (c) 823 K. Note the scalar offset of the models which is to account for the amount of primary creep, which is assumed to occur instantaneously. It can be seen from the results that, in general, the fit for 723 K is less accurate than the other temperatures. This is due to the limited data available at this temperature.

A summary of the full CTH model results are shown in Figures B.7 to B.12 thereafter. It can be seen that the full CTH model better represents the transient primary creep regime. An important note regarding the models is that each casting is modelled by only one model for all temperature and stress combinations.

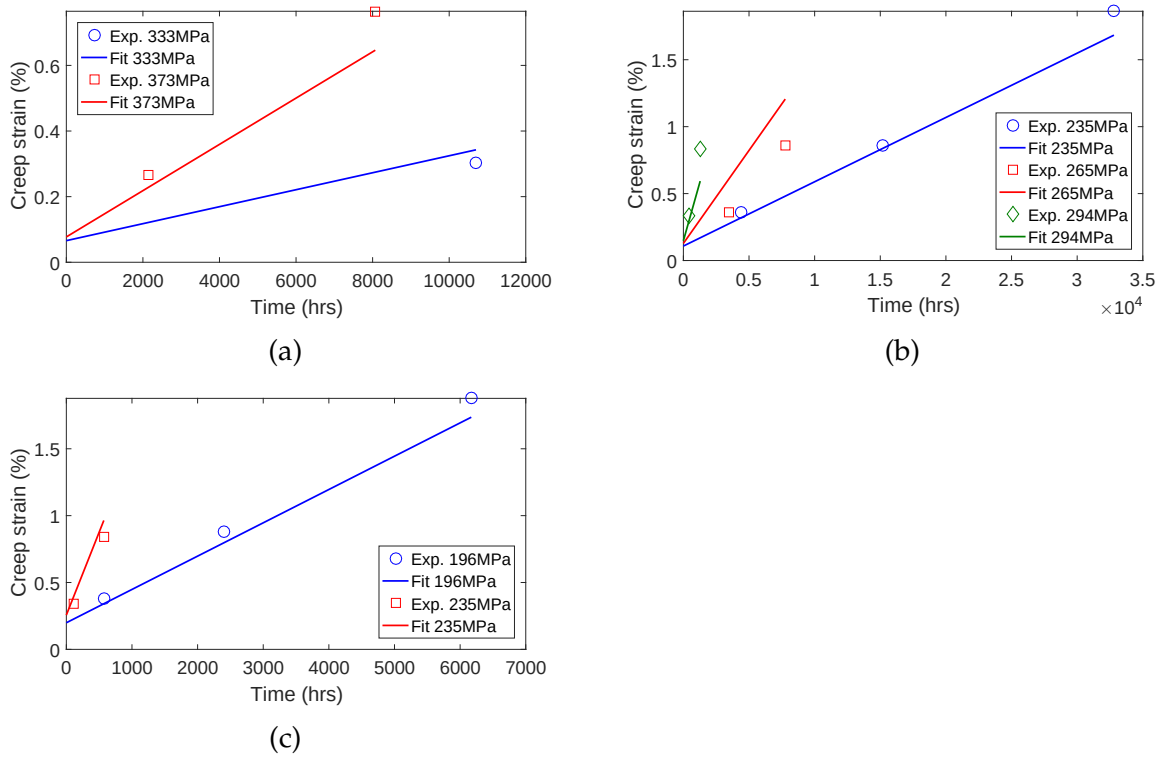

Figure B.1: Summary of simplified CTH model results for casting VbB at (a) 723 K, (b) 773 K, and (c) 823 K

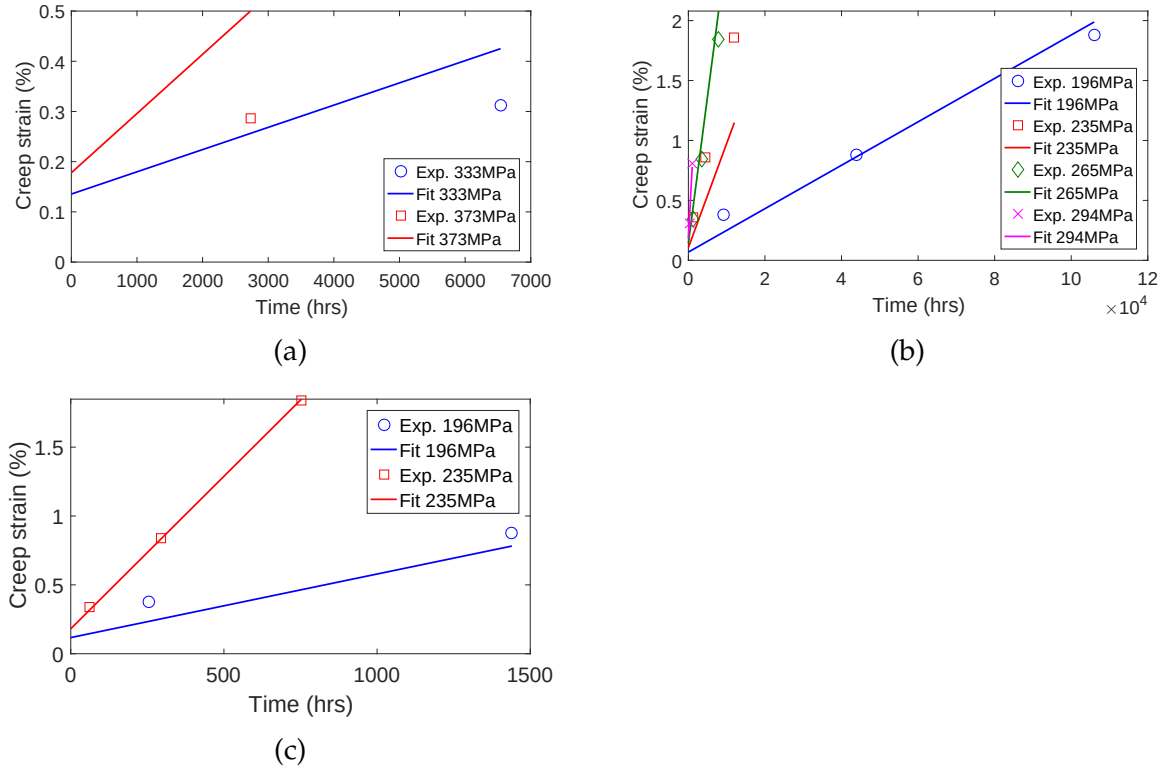

Figure B.2: Summary of simplified CTH model results for casting VbD at (a) 723 K, (b) 773 K, and (c) 823 K

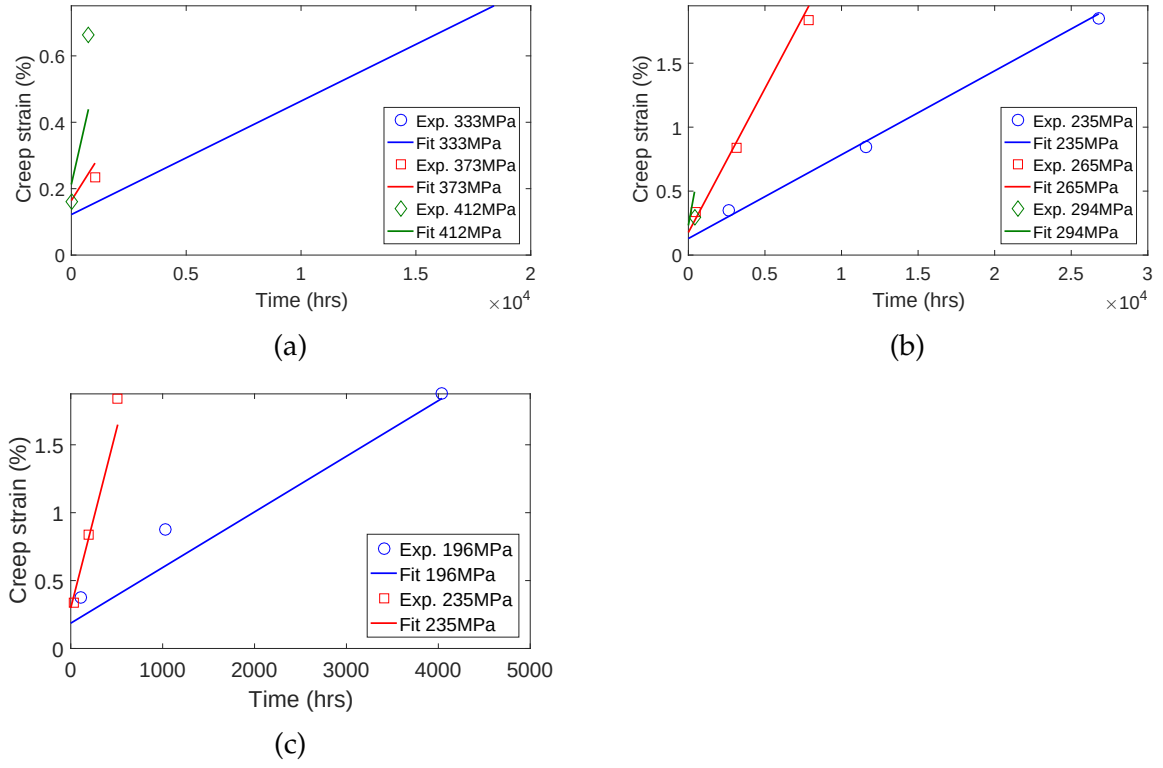

Figure B.3: Summary of simplified CTH model results for casting VbG at (a) 723 K, (b) 773 K, and (c) 823 K

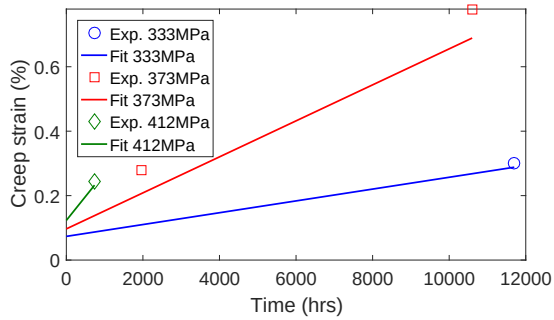

(a)

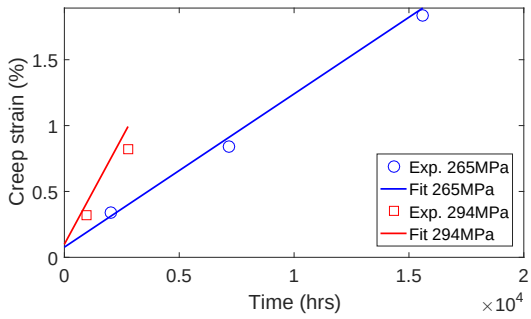

(b)

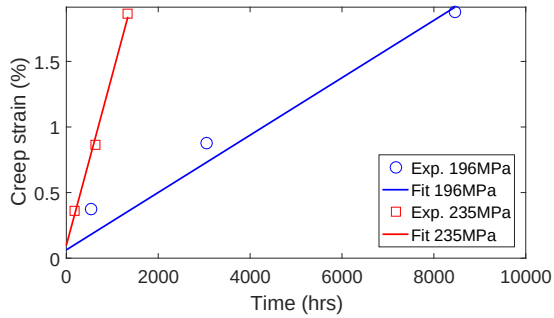

(c)

Figure B.4: Summary of simplified CTH model results for casting VbJ at (a) 723 K, (b) 773 K, and (c) 823 K

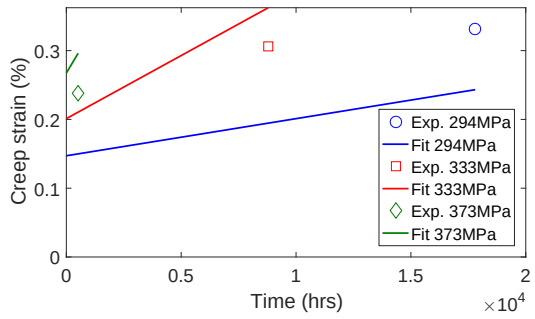

(a)

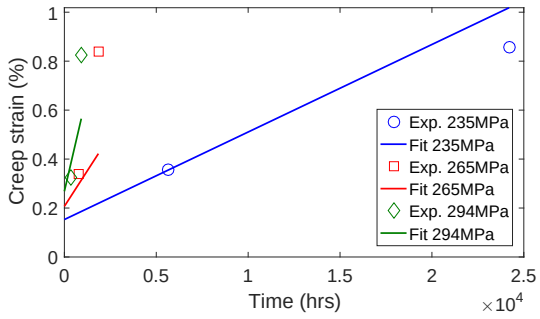

(b)

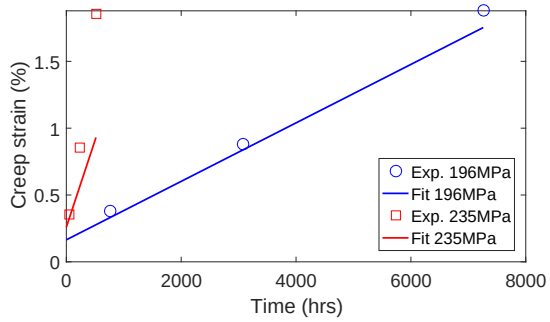

(c)

Figure B.5: Summary of simplified CTH model results for casting VbM at (a) 723 K, (b) 773 K, and (c) 823 K

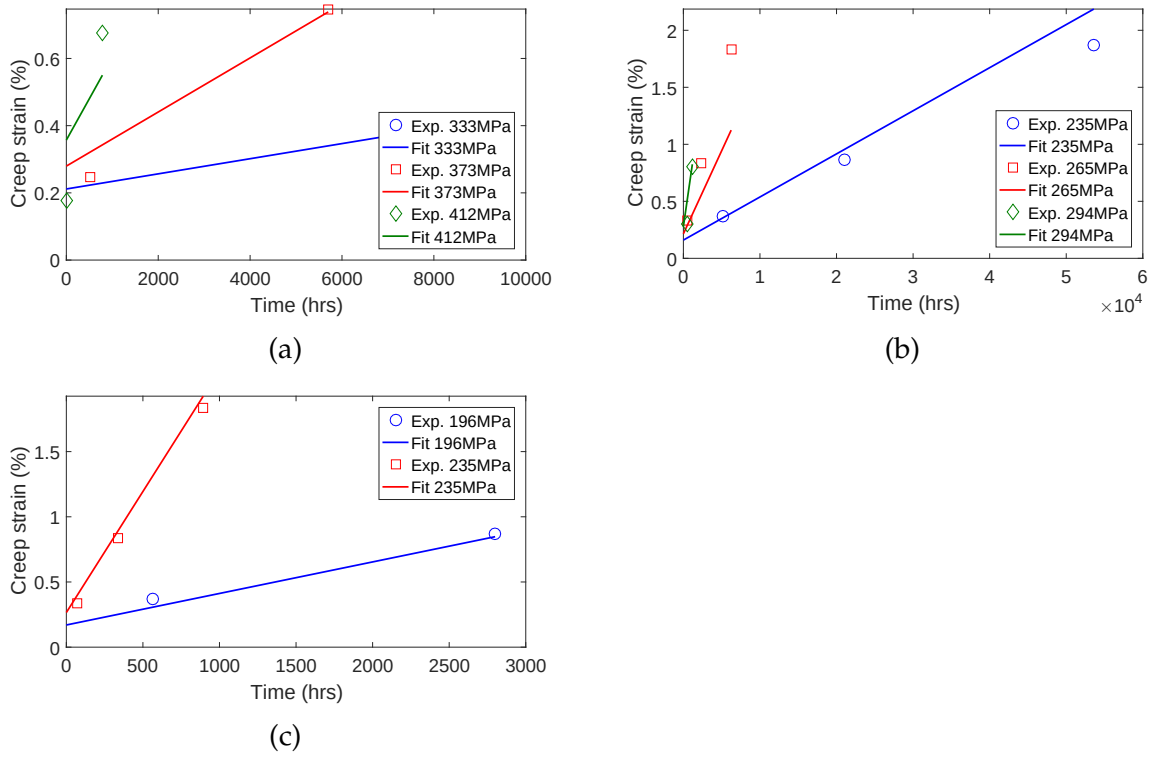

Figure B.6: Summary of simplified CTH model results for casting VbN at (a) 723 K, (b) 773 K, and (c) 823 K

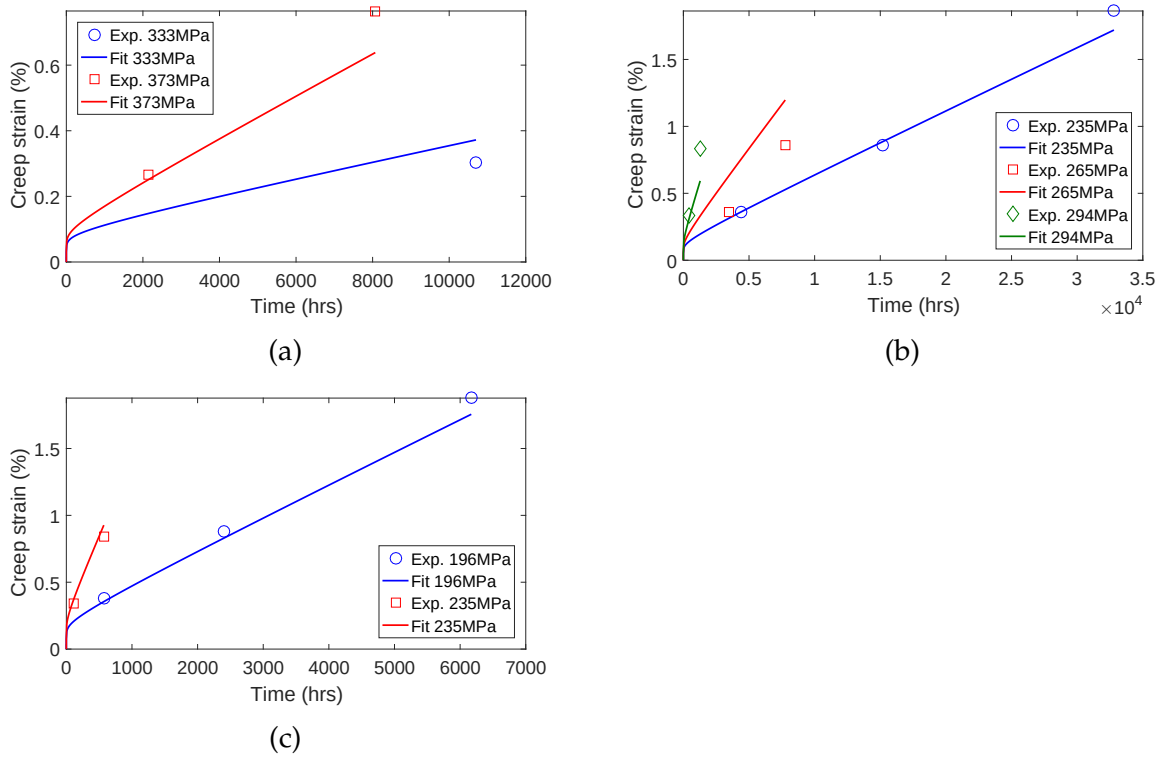

Figure B.7: Summary of full CTH model results for casting VbB at (a) 723 K, (b) 773 K, and (c) 823 K

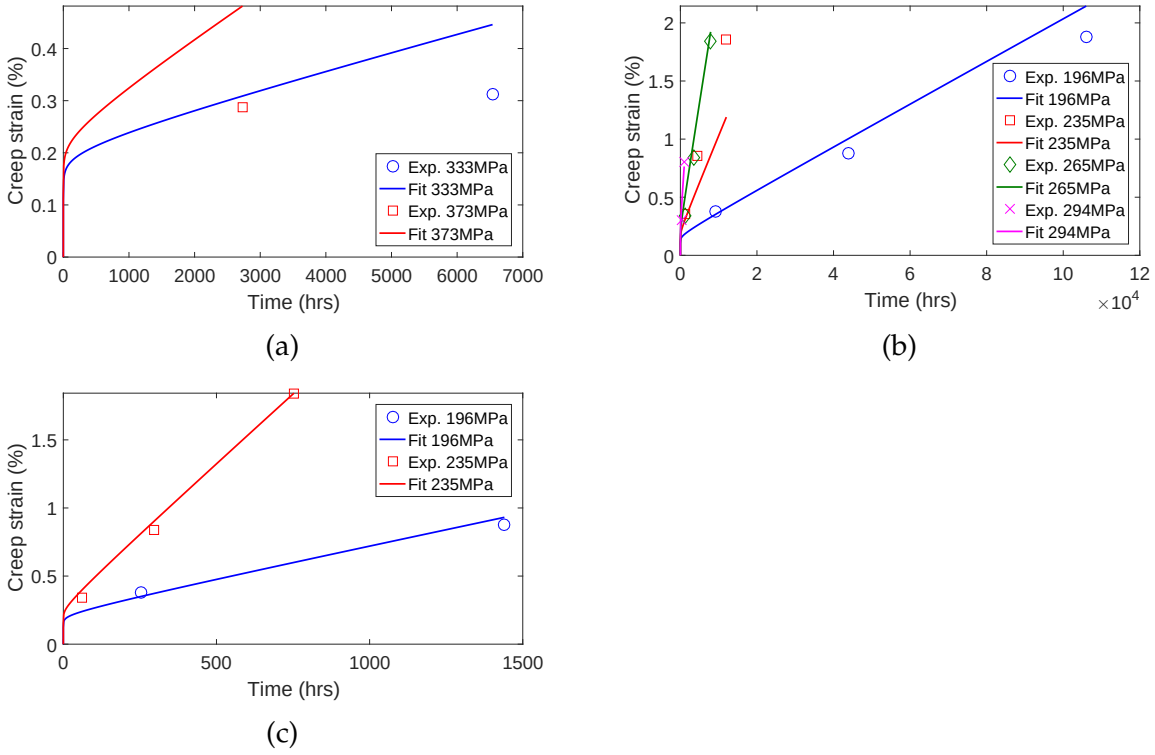

Figure B.8: Summary of full CTH model results for casting VbD at (a) 723 K, (b) 773 K, and (c) 823 K

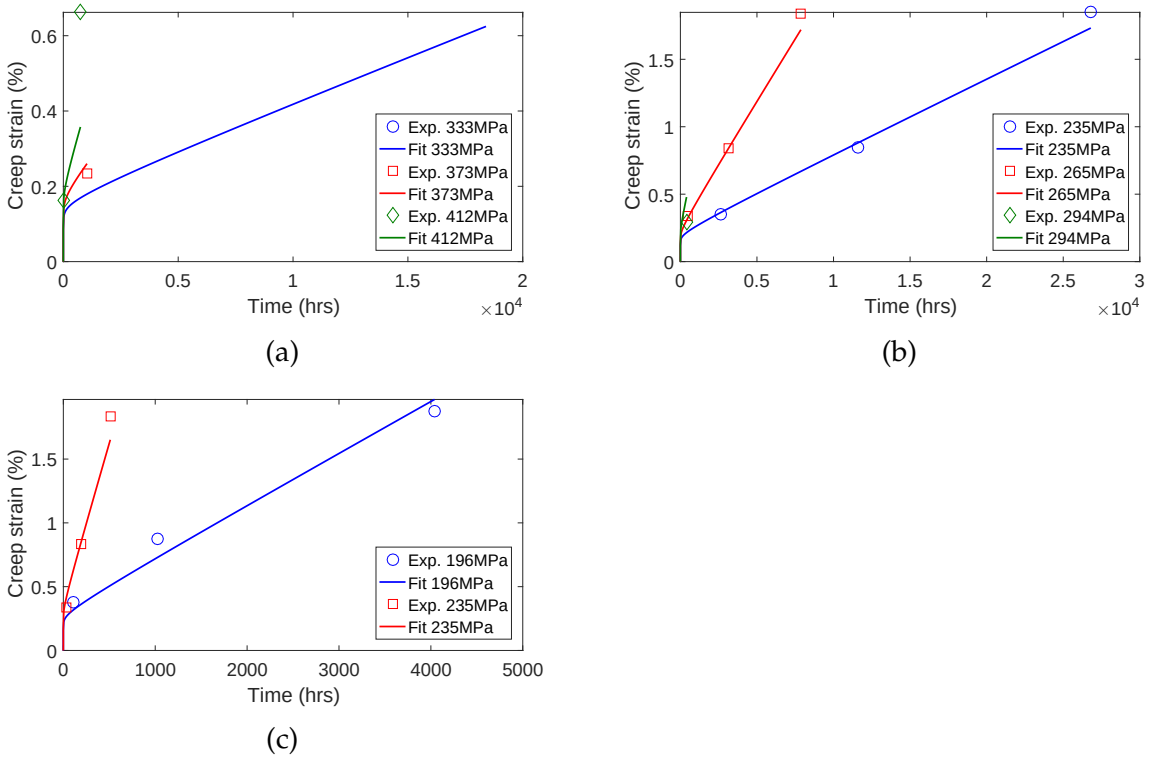

Figure B.9: Summary of full CTH model results for casting VbG at (a) 723 K, (b) 773 K, and (c) 823 K

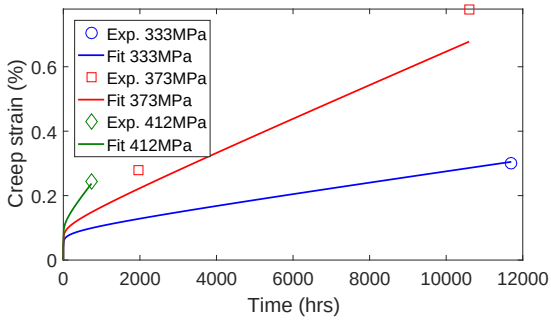

(a)

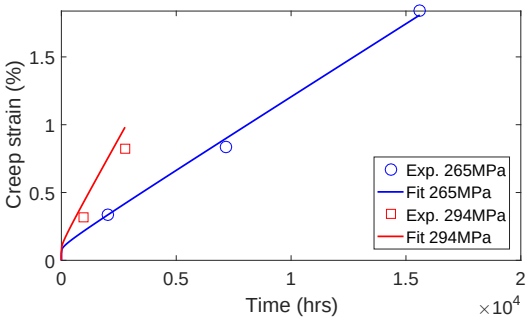

(b)

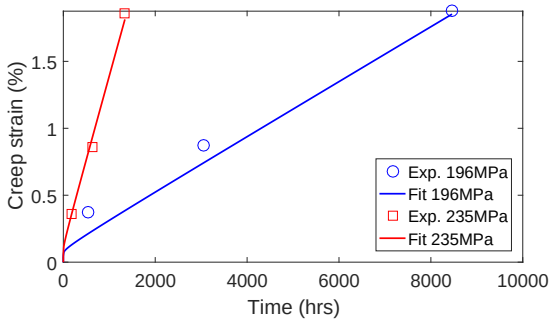

(c)

Figure B.10: Summary of full CTH model results for casting VbJ at (a) 723 K, (b) 773 K, and (c) 823 K

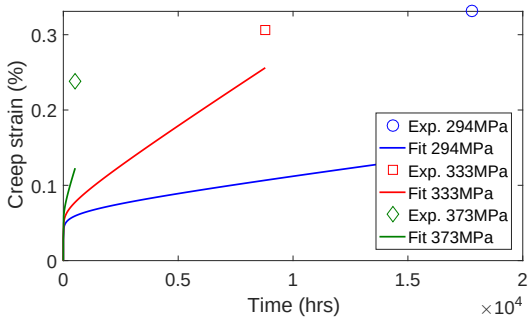

(a)

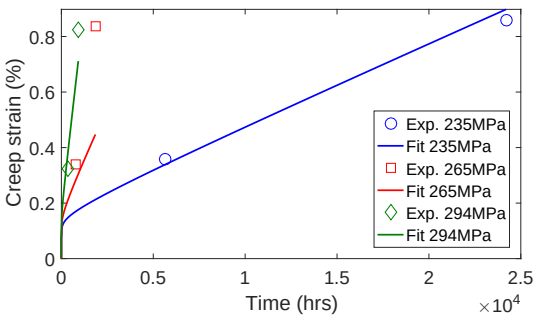

(b)

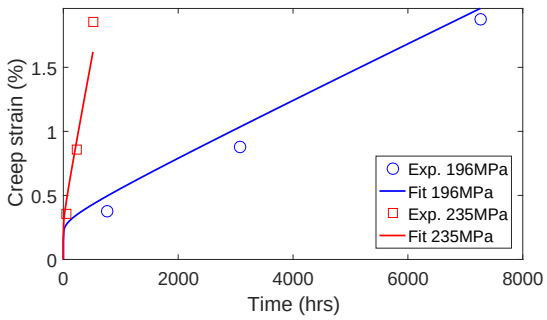

(c)

Figure B.11: Summary of full CTH model results for casting VbM at (a) 723 K, (b) 773 K, and (c) 823 K

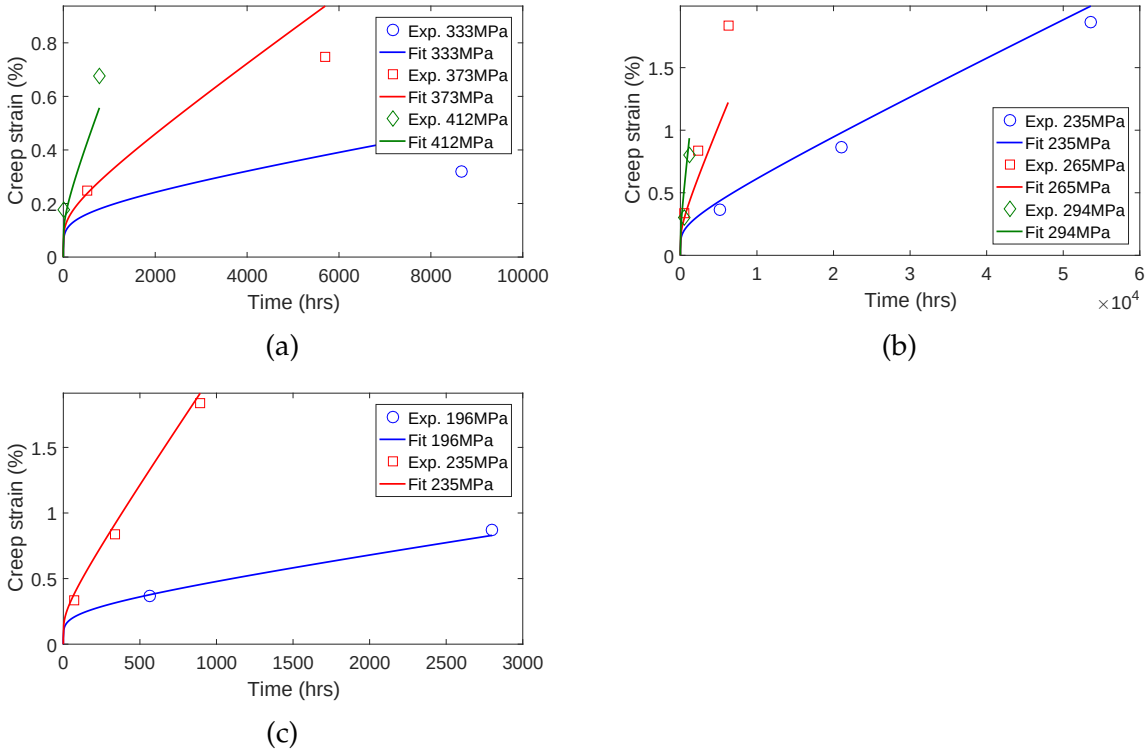

Figure B.12: Summary of full CTH model results for casting VbN at (a) 723 K, (b) 773 K, and (c) 823 K

Appendix C

Validation of boundary conditions

Consider the simplified sketch of the steam inlet in Figure C.1 in which the internal pressure, P_i, and the reaction forces, F_R, are shown. To ensure the correct axial forces are generated it is necessary for the force caused by the internal pressure to be equivalent to the reaction forces at the frictionless boundary conditions.

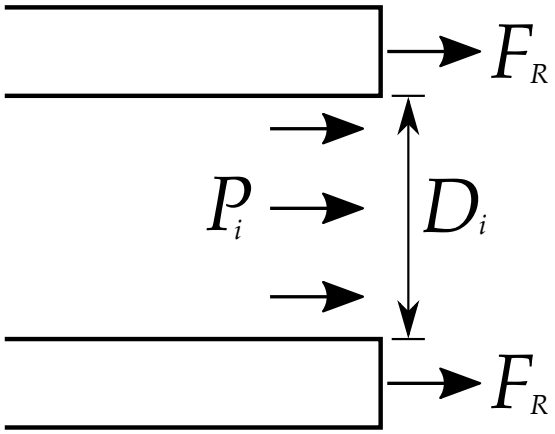

Figure C.1: Simplified sketch of steam inlet

The force caused by the internal pressure, F_{P_i}, is derived from $\sigma = F/A$ as follows,

$$\begin{aligned} F_{P_i} &= P_i A \\ &= P_i \left(\frac{\pi}{4} D_i^2\right), \end{aligned} \tag{C.1}$$

where D_i is the internal diameter which the force would act on to cause an axial load in the pipe. In order to validate the FE boundary conditions it is necessary to ensure that the reaction forces calculated from the FE solution are equivalent to F_{P_i} from Equation C.1. A summary of the results from these calculations is given in Table C.1.

Table C.1: Boundary condition validation results

Support	P_i (MPa)	D_i (mm)	F_{P_i} (kN)	F_R (kN)	% Error
Steam inlet		470	555.2	555.2	0.0
Steam outlet	3.2	480	579.1	579.1	0.00
Control side		740	1376.3	1285.5	6.6

It can be seen from the results tabulated above that the largest discrepancy is 6.6%. This discrepancy can be assumed due a combination of the simplifications in the calculations done, and the complexity of the geometry at the control side. It can therefore be concluded that the frictionless roller supports have been validated, with negligible errors in the force balance results.

Appendix D

Failure analysis

The L-M parameter enables the engineer to estimate creep life for arbitrary temperature and stress combinations. By fitting a best fit polynomial through the available rupture data, it is possible to determine the L-M parameter for an arbitrary stress. Manipulation of the L-M formulation then allows the creep life to be estimated. Consider the polynomial fit through the NIMS rupture data in Figure 6.1. The polynomial for the rupture data formulation was given by,

$$\sigma_{rup} = 13901.74 \; - \; 3192.86 \log(P_{LM}). \tag{D.1}$$

The L-M parameter P_{LM} can be obtained by manipulating Equation D.1 such that P_{LM} is the subject of the formula. This manipulated polynomial is given by,

$$P_{LM} = 10^{\frac{13901.71 - \sigma_{rup}}{3192.86}}. \tag{D.2}$$

Consider the worst case scenario in which the relaxed stress is 50.09 MPa. The L-M parameter is calculated using Equation D.2 as,

$$\begin{aligned} P_{LM} &= 10^{\frac{13901.71 - 50.09}{3192.86}} \\ &= 21792.70. \end{aligned} \tag{D.3}$$

Manipulation of the original L-M formulation will allow for the creep life to be calculated. This is given by,

$$\begin{aligned} P_{LM} &= T(\log t_r + 20) \\ t_r &= 10^{\frac{P_{LM}}{T} - 20}. \end{aligned} \tag{D.4}$$

Lastly, by substituting the operating temperature of $T = 783$ K and the L-M parameter previously calculated into Equation D.4 it is possible to estimate the creep life. This results in,

$$\begin{aligned} t_r &= 10^{\frac{21792.70}{783} - 20} \\ &= 67969.11 \text{ kh}. \end{aligned} \tag{D.5}$$

Note that this is an extremely high lifetime, equivalent to more than 7000 years. This result proves that, at the operating temperature and pressure, the IP valve will not fail due to creep alone.